PERFORMANCE ANALYSIS AND IMPAIRMENT IDENTIFICATION IN OPTICAL COMMUNICATION SYSTEMS

A Dissertation
Presented to
The Academic Faculty

By

Siddharth Varughese

In Partial Fulfillment
of the Requirements for the Degree
Doctor of Philosophy in the
School of Electrical and Computer Engineering

Georgia Institute of Technology

December 2020

Copyright © Siddharth Varughese 2020

PERFORMANCE ANALYSIS AND IMPAIRMENT IDENTIFICATION IN OPTICAL COMMUNICATION SYSTEMS

Approved by:

Dr. Stephen E. Ralph, Advisor
School of Electrical and Computer Engineering
Georgia Institute of Technology

Dr. Matthieu Bloch
School of Electrical and Computer Engineering
Georgia Institute of Technology

Dr. David Anderson
School of Electrical and Computer Engineering
Georgia Institute of Technology

Dr. Sorin Tibuleac
System Architecture
ADVA Optical Networking

Dr. Neil Guerrero Gonzalez
Department of Electrical and Electronic Engineering
Universidad Nacional de Colombia

Date Approved: August 11, 2020

Let me try this one more thing before going home...

Every PhD student

To my parents

ACKNOWLEDGMENTS

"If I have seen further than others, it is by standing upon the shoulders of giants"

Issac Newton

While a successful defense of this dissertation grants me the title of a PhD, I could have never obtained it without the support, guidance, collaboration, and patience of many individuals that I am extremely grateful for.

I would like to thank Prof. Stephen E. Ralph for providing me with the opportunity to work with him. His unique philosophy of industrial collaborations in academic settings transformed the problems I worked on for my PhD and made them both intellectually challenging and emotionally enjoyable. I am thankful for his time, resources, and advice that he invested not only into my education and research but also my personal and professional development.

Next, I would like to thank Dr. Sorin Tibuleac. He was a key figure during my PhD who ensured that all my research efforts continued to be exceptional, practical, and feasible. I would also like to thank my reading committee members - Prof. Matthieu Bloch and Prof. David Anderson. I am grateful for their intriguing questions and guidance without which this dissertation could not be. I am also indebted to Prof. Neil Gonzalez for agreeing to be my external committee member.

Then, I would like to thank all our industrial collaborators, specifically the following people for their continued support throughout my PhD - Dr. Thomas Richter from ADVA Optical Networking, Dr. Richard DeSalvo from L3Harris, Shane Hazzard, Pavel Zinvy,

and Maria Agoston from Tektronix, Scott Fergusson from Keysight Technologies, Gabriel Martin from Rhode Schwarz, and Dr. Hari Shankar from Inphi.

I would like to acknowledge my colleagues Michael Pratt, Edward Tan, Christian Bottenfield, Daniel Garon, Alec Hammond, Michael Hoff and Ewa Simpanen for their support. I am particularly thankful for Dr. Pierre Isautier who helped me get started with my PhD, Dr. Varghese A. Thomas for insightful discussions, and Dr. Jerrod Langston, Dr. Justin Lavrencik, Dr. Jie Pan, Daniel Lippiatt, Alirio Melgar, Dr. Jhon Granada, HyungJoon Cho and Gareeyasee Saha for all our interactions, technical and otherwise.

My gratitude to all my friends that made this American journey wonderful. They are too many to name but here is an attempt - Aditya Sharma, Dr. Doughlas "Bo" Broadwater, Garrett Huang, Pavan Thaker, and Shawn Reginuald for all the memories at graduate and family housing, Anthony Harding and Will Braddock for our Gloomhaven adventures, Dr. Nishant Zachariah and Dr. Christa Zachariah for taking care of me as their own, Youngrak Park, Seth Baer, Patrick Friedrich, Deepak Kamal, Christopher Kunneth and Andrew Fillingim for poker nights, and Jesse Balsiger for our rocket league escapade. Special mention to Deepu Jose for many things that are too many to list here, and Breaunna Wright for her never-ending support, good mood, and energy.

Finally, I would like to thank my family - my parents for their unconditional love and support throughout my life (I am sure they are happy to see me leave school successfully after 27 years), my sister for her encouragements and support, and my extended family for always being there for me.

TABLE OF CONTENTS

LIST OF TABLES

LIST OF FIGURES

NOMENCLATURE

$EENoB_{DC}$	excess $ENoB_{DC}$
$ENoB_{DC}$	frequency independent ENoB
f_B	measurement bandwidth
F_n	EDFA noise figure
$H(f)$	filter response
σ_{tj}	root mean square timing jitter
σ_G	variance of noise added to obtain threshold SER when computing TDECQ

1D-CNN	one-dimensional CNN
ADALINE	adaptive linear element
Adam	adaptive moment
ADC	analog to digital converter
AFC	adaptive filter coefficients
ASE	amplified spontaneous emission
ASIC	application specific integrated circuit
AWG	arbitrary waveform generator
AWGN	additive white gaussian noise
BERT	bit error rate tester
BSS	blind source separation
CD	chromatic dispersion
CMA	constant modulus algorithm

CMOS	complementary metal oxide semiconductor
CNN	convolutional neural network
DAC	digital to analog converter
DCF	dispersion compensating fiber
DCR	digital coherent receiver
DM	dispersion management
DNL	differential nonlinearity
DSF	dispersion shifted fiber
DSP	digital signal processing
EC	electronic converters
ECL	external cavity laser
EDFA	erbium doped fiber amplifiers
ENoB	effective number of bits
FEC	forward error correction
FEL	feature extraction layer
FFE	feedforward equalizer
FWHM	full-width half-maxima
FWM	four wave mixing
GaAs	gallium arsenide
GBaud	Gigabaud per second
GPU	graphic processing unit
ICA	independent component analysis
ICI	interchannel interference
INL	integral nonlinearity
I/Q	in-phase/quadrature
ISI	intersymbol interference
ITU	international telecommunication union

LMS	least mean square
LP	launch power
LSB	least significant bit
LSTM	long short term memory
MAP	maximum a priori
ML	machine learning
MLSE	maximum likelihood sequence estimation
MMA	multi-modulus algorithm
MMF	multimode fiber
MPI	multipath interference
MRE	mean reconstruction error
MSE	mean square error
NN	neural network
NZDF	nonzero dispersion fiber
OMA	optical modulation amplitude
OSA	optical spectrum analyzer
OSNR	optical signal-to-noise ratio
PAM	pulse amplitude modulation
PBS	polarization beam splitter
PCA	principal component analysis
PDF	probability distribution function
PDL	polarization dependent loss
PDM	polarization division multiplexing
PMD	polarization mode dispersion
PRBS	pseudo random binary sequence
PSD	power spectral density
QAM	quadrature amplitude modulation

QPSK	quadrature phase shift keying
RBF	radial basis function
ReLU	rectified linear unit
RMS	root mean square
RMSprop	root mean square propagation
ROADM	reconfigurable add-drop multiplexers
RS	Reed-Solomon
SD-FEC	soft decision FEC
SER	symbol error rate
SINAD	signal-to-noise-and-distortion ratio
SLA	service level agreement
SNR	signal-to-noise ratio
SoP	state of polarization
SPM	self-phase modulation
SSMF	standard single-mode fiber
SSPRQ	short stress pseudo-random quaternary
SVM	support vector machines
TDECQ	transmission dispersion eye-closure quaternary
TDP	transmitter dispersion penalty
tLSTM	truncated LSTM
UI	unit interval
VCSEL	vertical cavity surface emitting laser
WDM	wavelength division multiplexing
WSS	wavelength selective switch
XPM	cross-phase modulation

SUMMARY

Over the past 50 years, optical communications systems have grown tremendously achieving exceptional data rates and reaches. This growth has been enabled through a variety of techniques and technologies such as electronic converters, EDFAs, ROADMs, DSP, WDM, FEC etc. However, as optical networks continue to grow, these techniques and technologies will introduce new limitations to all optical communication systems. The objectives of this research revolves around identifying how these techniques and technologies would affect link performance, manufacturing efficiency, network operation and maintenance, and develop methodologies to mitigate or minimize these limitations.

CHAPTER 1
INTRODUCTION

Internet data rate requirements are expected to exponentially grow in the next five years owing to increases in internet access to the global population, increases in networked devices due to internet of things (IoT), rise of smart appliances, upcoming technologies such as 5G etc [1]. Optical networks have supported these rising data rate demands in the past as the internet's backbone owing to optical fiber's large operational bandwidth and low transportation losses. In fact, in the past 30 years, data rates in individual fiber has increased from 10 Gbps in 1990 to 100 Tbps in 2019 in order to support the rising data rate requirements [2]. This tremendous increase has been largely contributed to multiple innovations in this field which include erbium doped fiber amplifiers (EDFAs), wavelength division multiplexing (WDM), optical networking, digital signal processing (DSP), forward error correction (FEC), application specific integrated circuits (ASIC), advanced modulation formats etc.

However, in order to increase connectivity and meet predicted increases in data rate requirements, optical systems are expected to get faster and complex network configurations are expected to be deployed soon. These implementations would introduce new limitations and impairments to the system that need to be investigated to understand their effects on system performance. The objectives of this research is multidimensional, but revolves around identifying how new techniques and technologies that are going to be deployed in the next generation of optical communication systems would affect link performance, manufacturing efficiency, network operation and maintenance, and develop methodologies to mitigate or minimize these limitations.

This dissertation is arranged in six chapters. Given the interdisciplinary nature of modern optical communication systems and this research, chapter 2 attempts to give readers the required background information to understand the main contributions of this disserta-

tion. It includes a brief historical overview of optical communication systems, a detailed description of the physical phenomena responsible for signal propagation through optical fiber, a detailed description of all optical components required to deploy an optical link, a brief description of DSP algorithms used in optical communication systems with a detailed description of all DSP algorithms used in this research, a brief description of transmitter and dispersion eye closure quaternary (TDECQ), and a brief overview of machine learning (ML) with a detailed description of all ML techniques used here. Chapter 2 does not claim any novelty and is heavily inspired by the work of Agarwal et al. [3, 4], Kumar et al.[5], and Goodfellow et al. [6].

The first novel contribution of this dissertation is described in chapter 3. It identifies electronic converters (ECs) as a major source of impairments in next generation optical communication systems and develops a theory that captures frequency dependent effective number of bits (ENoB) such as those exhibited by modern wideband ECs. The chapter then describes novel and computationally efficient digital to analog converter (DAC) and analog to digital converter (ADC) models that were developed through this research effort to simulate the effects of wideband ECs in optical communication systems. Theoretical and experimental verification of the models are also presented here. Finally, we use these models to identify penalties introduced by ECs on next generation links employing data rates of 400 Gbps, 600 Gbps and 800 Gbps.

In chapter 4, we describe our research efforts to accelerate TDECQ assessments of optical transmitters using ML. TDECQ is a computationally expensive standardization algorithm that is used to accurately qualify optical transmitters. Owing to its accuracy, it has seen relative success in the industry recently. However, such a complex algorithm can reduce manufacturing efficiencies and product yield. The chapter describes two techniques to accelerate TDECQ assessments using ML, one using eye-diagram images and the other using real-time signals. Assessment accuracy and computational speeds of both techniques are also presented.

As the data rates grow, so do the size of the associated networks. While optical communication systems are sufficiently robust, instances of failures in optical links are bound to increase owing to the sheer size of the network. In such a situation, it is important to automate fault management systems in optical networks to ensure smooth network operations. In chapter 5, we develop ML techniques that can be used in next generation optical networks to automate its fault management systems. Techniques described in this chapter utilize features that are easily available at the coherent receiver DSP for fault detection/prediction and identification.

Finally, chapter 6 draws conclusions to this dissertation with a review of key concepts introduced in chapters 3, 4 and 5, a summary of all novel contributions to this field and suggestions for future research topics. Appendices contain some supplementary notes for chapter 3 and research work describing the impact of polybinary coding on data rates in multimode fiber (MMF) links employing vertical cavity surface emitting lasers (VCSELs) that the author explored during his PhD.

CHAPTER 2
BACKGROUND INFORMATION

2.1 A Historical Overview

In its broadest sense, the use of light for communication dates as far back as civilization itself when mankind used mirrors, fire beacons and/or smoke signals to convey messages. While the data rates and reach were severely limited in these methodologies, efforts have been made ever since to improve on these systems [2, 3]. A major advance in this field occurred in 1792, when Claude Chappe demonstrated transmitting mechanically coded messages over long distances with relay stations every 10-15 km [7]. He called his invention optical telegraph and it was first deployed in July 1794 between Paris and Lille. Even though the data rate was less than 1 bps, the optical telegraph network was deployed all over Europe by 1830 owing to its reach.

The optical telegraph was replaced by the electrical telegraph in the 1830s, signaling the beginning of electrical communication [8]. Data rates could be increased to a few bps using new coding schemes such as the Morse code and the first successful transatlantic electrical telegraph was deployed in 1866. Over the next 100 years, electrical methodologies dominated the deployed communication systems reaching 100s of Mbps in data rates and 1000s of km in range. These systems could not be improved in data rates any further due to cable losses and scientists around the world once again started investigating optical methods for telecommunication systems.

There were two barriers to implementing optical telecommunication in the 1950s - the absence of a coherent optical source to support higher data rates and the unavailability of a suitable optical transmission medium to support long transport distances. The first barrier was overcome in 1960, when Theodore Maiman successfully fired the first laser

demonstrating the possibility of a coherent source of light [9]. Optical fiber was available in the early 1960s, however, they were predominantly used for very short length applications owing to its high propagation losses. In 1966, Charles Kao demonstrated that optical fiber losses could be significantly reduced if impurities from silica glass could be removed while manufacturing fiber [10]. This would make optical fiber suitable for optical communication as they could guide light the same way copper wires could guide electrons. A team of three Corning scientist developed the first transport grade optical fiber with $<$20 dB/km propagation losses in 1970 [11]. Two years later, the same team developed optical fiber with only 4 dB/km propagation loss by replacing titanium with germanium as the dopant inside the fiber. Finally, in 1979, a Japanese team developed an optical fiber with 0.2 dB/km propagation losses near 1550 nm wavelengths [12]. This value was close to the fundamental limit set by a phenomenon known as Rayleigh scattering [13]. Around the same time, two groups in Russia [14] and Bell Laboratories [15] demonstrated compact and efficient gallium arsenide (GaAs) lasers that could operate continuously at room temperatures. The simultaneous availability of compact coherent optical sources and low-loss optical transport media marked the dawn of optical telecommunication systems.

2.1.1 The First Era

On April 1, 1977 American Telephone and Telegraph (AT&T) sent its first test signals in Chicago's loop district operating at 45 Mbps near infrared wavelengths of 850 nm. The wavelength was chosen because of the GaAs semiconductor lasers used as the transmitting laser. While the propagation loss (3 dB/km) was relatively higher at this wavelength, it was better than coaxial-cables operating at the same data rates. Within months, three companies deployed fiber based optical communication systems with live telephone traffic - General Telephone and Electronic (GTE) in Long Beach, California at 6 Mbps, AT&T in Chicago at 45 Mbps and United Kingdon Post Office near Martlesham Heath, UK at 8.4 Mbps [16–18]. The suite was followed by other European countries in the following years [19]. With

these deployments began the first era of fiber optical communication systems - the era of direct-detection regenerated systems [20]. This era lasted about 16 years (1977-1993) and saw many major milestones. The first "fiber-to-the-home" was demonstrated in Japan's Hi OVIS project in 1978. The first 1300 nm wavelength system was demonstrated in 1981 and the first system to use single-mode fiber was demonstrated in 1982. Additionally, the first submarine fiber system using these technologies was installed in 1984. The move from 850 nm wavelength systems using multimode fiber to 1300 nm wavelength systems using single mode fiber was crucial to meet the increasing telecommunication capacity demands. The remainder of the era saw data rates move from 45 Mbps to 90 Mbps, 180 Mbps, 417 Mbps and finally 1.7 Gbps. The first two wavelength system, two operating channels simultaneously transported through a single fiber, was demonstrated in 1989 with an aggregate data rate of 3.4 Gbps. The capacity of these systems were limited by the transceiver interface rates since signals had to be regenerated every 10-or-so km to maintain signal quality. Therefore, further progress in this era was limited to increasing data rates to 2.5 Gbps per wavelength.

2.1.2 The Second Era

Many proposed increasing the optical transport data rates by supporting multiple wavelengths through a single fiber. However, this would require multiple repeater units since there was no cost effective way to amplify multiple wavelengths simultaneously. In the late 1980s, the first practical EDFA was developed. The EDFA was able to optically amplify multiple wavelengths around the 1550nm spectra alleviating the need for repeater units. However, the EDFA alone could not solve the growing capacity requirements as the performance was also limited by the existing standard single-mode fiber (SSMF, ITU G.652). SSMF had a large chromatic dispersion (CD) parameter (17 ps/nm/km) that introduced significant intersymbol interference (ISI), limiting the reach of a 10 Gbps systems to only 60 km. In order to eliminate CD, dispersion-shifted fibers (DSF, ITU G.653) were developed

which could support 10 Gbps over many thousands of kilometers. Owing to this feature of DSFs, they were widely deployed in Japan and North America. However, they proved fatal when data rates had to be increased in a single fiber by bringing wavelengths closer and loading more wavelengths.

Four wave mixing (FWM) is a naturally occurring nonlinear phenomenon in silica/glass that generates new wavelengths/frequencies through the interaction of two or three existing wavelengths/frequencies [21]. The newly generated wavelengths scale drastically with existing wavelengths, generating as many as 100 new wavelengths in the presence of 10 existing wavelengths. Not only does FWM rob signal wavelengths of their power, they also coherently mix with signal wavelengths adding distortions to the signal. FWM only occurs under a special condition, known as phase matching, where the phase relation between different wavelengths need to be fixed. This condition is difficult to achieve in optical fiber owing to the evolving phase between wavelengths caused by CD. Since there is no CD in DSFs, FWM thrives in such fiber, severely limiting the performance of an optical link.

In order to mitigate the effects of FWM in DSFs, researchers at AT&T Bell Laboratories developed nonzero dispersion fiber (NZDF, ITU G.655) with low but nonzero CD [22]. This fiber was popularly known as TrueWave fiber. Interestingly, the fiber could be produced in two flavors, with slightly positive and slightly negative CD. This enabled fiber networks to have zero overall CD by concatenating fibers of opposite CD signs, but have sufficient local CD to suppress FWM. The technique was known as dispersion management (DM) and was widely deployed all around the world. While simple combinations (also known as dispersion maps) of fiber was initially sufficient to support long distances of optical transport, they became insufficient for data rates at and beyond 20 Gbps. Many networks saw sophisticated dispersion maps to support higher data rates and more wavelengths [23]. The introduction of dispersion compensating fiber (DCFs) in mid the 1990s, a special fiber with very high negative CD compared to NZDF, allowed for smaller spools of localized negative CD fiber in complicated dispersion maps [24, 25]. This enabled higher

flexibility in deploying complicated dispersion maps and avoided the need to deploy two different types of fiber in an optical network. An optical network equipped with DCFs could support over 80 wavelengths with each wavelength operating at 40 Gbps.

Multiplexing multiple wavelengths on a single fiber to enhance data rates is known as WDM. An important development in the field of optical communication along with DCF and EDFA enabled WDM, was the ability to aggregate, disaggregate and switch data paths in the optical domain. This was referred to as optical add-drop multiplexing (OADM). Early work showed promising results on reconfigurable optical paths to harness the most out of optical networks [26]. MONET, a US government funded project, demonstrated operational reconfigurable optical networks in the late 1990s [27]. However, it was not until the late 2000s that optical networks saw widespread commercial deployment of reconfigurable OADMs (ROADMs). Optical networks were challenged by DM since optimal dispersion maps required DCFs on a per wavelength basis in the presence of optical switching, adding to deployment costs and complexity. Alternative methodologies had to be developed to achieve high network flexibility and transmission performance.

The invention of wideband EDFAs that could optically amplify over 80 wavelengths on a single fiber, along with the development of DCFs or negative CD NZDFs that eliminated CD induced ISI and minimized FWM, and simple optical networks that could switch data paths optically marked the second era of fiber optical communication systems - the era of amplified dispersion managed systems. This era lasted almost 16 years from 1993 to 2009.

2.1.3 The Third Era

Even with the best dispersion maps, commercial EDFAs ran out of operational amplification bandwidths and it was not possible to increase data rates by adding any more wavelengths. The only way to increase data rates was to move from rudimentary two level signals to advanced modulation formats, so as to transport more bits per unit time [28]. Initial deployments included binary and quadrature phase shift keying (BPSK and QPSK) formats

which could be detected using existing receiver technologies employing direct detect photodiodes. However, to employ and detect higher modulation formats, coherent receivers would be required. There were significant efforts in understanding coherent receivers in the 1980s [29] owing to its higher receiver sensitivities. However, with the invention of practical EDFAs in the late 1980s, interest in coherent receivers faded since optical signals could now be amplified and increased receiver sensitivities were no longer required. Interests in coherent systems resurfaced when data rates could no longer be increased in optical networks using existing technologies.

The resurgence of coherent receivers was not just need driven but also opportunity driven. In the early 2000s, complementary metal oxide semiconductors (CMOS) processing and practical CMOS integrated ECs could employ 10 Gigabaud per second (GBaud) signaling rates. These ECs included DACs and ADCs. Together with coherent receivers, CMOS enabled the use of DSP techniques to achieve very high data rates. In 2004, the first CMOS enabled maximum likelihood sequence estimation (MLSE) was demonstrated [30] and commercially implemented [31] at 10 Gbps. MLSE based CD compensation was demonstrated for the first time in long-haul optical links in 2005 [32], but the exponential increase in complexity with distance rendered MLSE impractical for long-haul systems. This inspired research in linear equalization techniques that had significantly less computational complexity. However, linear equalizers would require the phase information of optical signals which directed researchers to also explore how to exploit the full optical field in an optical fiber: in-phase/quadrature modulation (I/Q) and polarization division multiplexing (PDM). Single mode fiber supports two orthogonal signals known as polarizations and it is possible to use them independently to transport data. By using all four orthogonal fields of the optical signal, transport data rates could be instantly quadrupled reaching 40 Gbps based on 10 Gbps system components [33]. Soon, the first commercial 28 GBaud links operating at 100 Gbps was delivered to Verizon by Alcatel-Lucent [34].

Coherent transponders equipped with DSP, known as digital coherent transponders,

were able to compensate for transoceanic amounts of CD with appropriate digital filters and incur little-to-no penalty. They eliminated the need for dispersion managed networks and links now could be deployed with any amounts of accumulated CD. This led to the deployment of modern fiber that has large CD (20 ps/nm/km) but low losses (0.14 dB/km) and large effective area to reduce nonlinear distortions from FWM [35]. Digital coherent transponders with modern fiber also revolutionized the field of network planning. These systems were much simpler to model as compared to DM direct detect systems, and simple analytic and semi-analytic model were developed to estimate link penalties and aid link budget analysis. Two such models are the Gaussian noise (GN) model and the enhanced Gaussian noise (EGN) model [36, 37].

Early optical links used simple FEC codes such as hamming codes to achieve better performance [38]. FEC adds redundancy to the information bits in a controlled fashion to enable correction of errors introduced by noise or other distortions in the channel. Reed-Solomon (RS) codes were also soon introduced in optical communication systems and RS(255,239) with 7% overhead was standardized in ITU-T G.975 [39]. RS(255,239) operates 4.4 dB from the shannon limit [40] at a bit error rate (BER) of 10^{-15}. Hamming codes and RS codes are hard decision codes that operate on bits (0s and 1s) to correct information bits. The advent of CMOS in optical communication system enabled soft decision FECs (SD-FECs) which could reduce the gap to 1-2 dB from the Shannon limit. SD-FECs employ finely quantized demodulator outputs that have an associated reliability measure, allowing for improved decoding performance. Currently deployed SD-FECs include product codes or low-density parity-check (LDPC) codes [41], decoded by iterative message passing in a graphical code model [42]. The gap to Shannon capacity can be further reduced by using modulation formats with non-uniform probability of occurrence [43]. This technique, known as probabilistic shaping, is currently deployed in certain long-haul links to achieve higher data rates [44].

The third era of optical communication systems, which is also the current era, was

boosted by the development of high speed CMOS processes and circuits. Along with various DSP and FEC techniques, they have enabled 100 Gbps using 28 GBaud PDM QPSK [34], 200 Gbps using 32 GBaud PDM 16QAM [45], 400 Gbps using 56 GBaud PDM 16QAM [46], and 1 Tbps using 90 Gbaud PDM 64QAM [47]. A single fiber can now support 65 Tbps over 6600 km [48]

Another aspect of optical communication systems that saw significant development in the third era was flexible mesh networking. The MONET project [27] established the need to provide all optical flexible networking to manage many WDM channels. However, DM systems that were deployed then made it difficult to achieve desired flexibility in the networking layer. Some believe that the expansion of networking in optical communication systems was purely coincidental with the introduction of coherent optical systems, but coherent systems did provide benefits to flexible networking. They eliminated DM systems that required local DCFs at add/drop sites, allowed adaptable transmission formats and data rates based of link distances and channel bandwidths, and provided steep receiver filtering through DSP to isolate the channel of interest effectively [49]. Owing to these changes introduced by coherent systems, today's ROADMs provide multi-degree mesh connectivity [49], flexible wavelength allocation [50, 51], and dynamic gain equalization to improve signal quality and maximize transport distances. Modern ROADMs, made up of wavelength selective switches (WSS), can support variable optical bandwidths unlike the early 1990s that had fixed 50 GHz bandwidth based on the 50 GHz ITU grid. Flexible grids have demonstrated higher data rate network capacities especially in small (metro) networks [52]. Additionally, today's ROADMs can handle optical signals at any wavelength in any direction without wavelength blocking. Therefore, they are popularly called colorless-directionless-contentionless (CDC) and are key components in modern optical networks.

CMOS based coherent receivers employing advanced modulation formats and soft-decision FECs, along with ROADM enabled flexible mesh networks define the third and current era of optical communication systems (2009 - till date). Research and commer-

cial efforts are currently exploring ways to further improve data rates and transport reach through improved CMOS processes, advanced DSP and FECs. There have been significant work in using ML to improve optical link performance [53], but they have seen limited commercial success owing to its computational challenges at high data rates. ML has however seen promising application in optical network management, especially in predicting link failures and quality of transmission (QoT) [54].

2.1.4 Conclusions

Many technological innovations since the late 1970s have enabled the creation of modern fiber optic based communication networks. This section attempted to give a brief historical overview to enable readers in identifying important milestones in this field and understand their motivation. Some efforts to improve optical communication system performances are based on the limitations of many of these milestones and form the motivation of this dissertation. Remaining sections in this chapter provide an in-depth description of the necessary background required to understand the main contributions of this dissertation.

2.2 Propagation of Signals in Optical Fiber

The phenomenon responsible for guiding light through an optical fiber is known as total internal reflection [4]. An optical fiber consists of a cylindrical core of silica surrounded by a cladding whose refractive index is lower than that of the core. Refractive index describes how fast light travels in a material and is defined by $\eta = c/v$, where c is the speed of light in vacuum and v is the speed of light in the material. SSMF uses an abrupt change in refractive index to confine the optical field and such fibers are called step-index fiber, Fig. 2.1. In order to understand the propagation of light through optical fiber, one needs to take a wave-propagation approach using Maxwell's equations as the geometrical approach is invalid when the core size (r_1) is comparable to the wavelength of light propagating through the fiber [55].

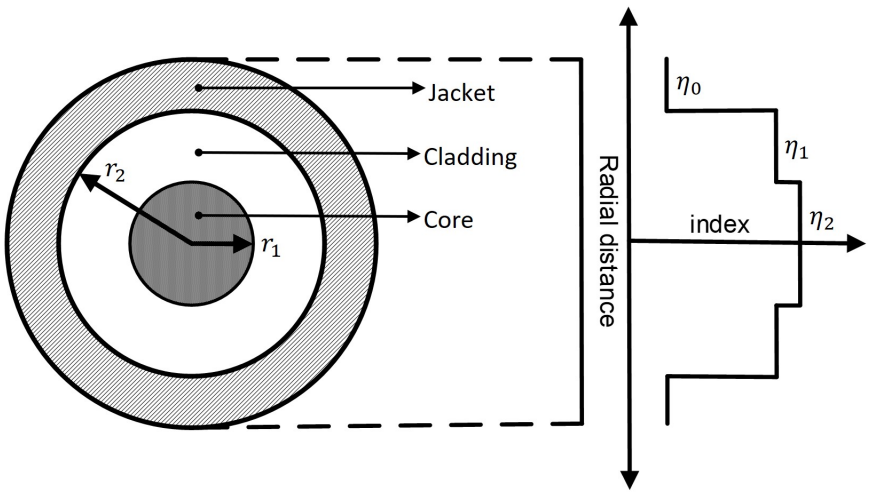

Figure 2.1: Cross section profile of a step-index fiber. The innermost layer is the core and has the highest refractive index (η_2). The second layer is the cladding and has a slightly lower refractive index (η_1). The outermost layer is the jacket and a significantly lower refractive index (η_0)

2.2.1 Wave Propagation through Step-Index Fiber

Since light is an electromagnetic wave, its propagation in an optical fiber is governed by Maxwell's Equations

$$\nabla \times \vec{\mathbf{E}} = -\frac{\partial \vec{\mathbf{B}}}{\partial t} \tag{2.1}$$

$$\nabla \times \vec{\mathbf{H}} = \frac{\partial \vec{\mathbf{D}}}{\partial t} \tag{2.2}$$

$$\nabla \cdot \vec{\mathbf{D}} = 0 \tag{2.3}$$

$$\nabla \cdot \vec{\mathbf{B}} = 0 \tag{2.4}$$

where $\vec{\mathbf{E}}$ and $\vec{\mathbf{H}}$ are the electric and magnetic field vectors respectively, and $\vec{\mathbf{D}}$ and $\vec{\mathbf{B}}$ are the corresponding electric and magnetic flux densities. The field vectors and the flux densities vectors are related by

$$\vec{\mathbf{D}} = \epsilon_0 \vec{\mathbf{E}} + \vec{\mathbf{P}} \tag{2.5}$$

$$\vec{\mathbf{B}} = \mu_0 \vec{\mathbf{H}} + \vec{\mathbf{M}} \tag{2.6}$$

where ϵ_0 and μ_0 are the permittivity and permeability in free space respectively, and $\vec{\mathbf{P}}$ and $\vec{\mathbf{M}}$ are the induced electric and magnetic polarizations respectively. In an optical fiber, $\vec{\mathbf{M}} = 0$ since silica glass is non-magnetic in nature. $\vec{\mathbf{P}}$, however, requires a microscopic quantum mechanical approach to evaluate. If we avoid evaluating $\vec{\mathbf{P}}$ near medium resonance, $\vec{\mathbf{P}}$ and $\vec{\mathbf{E}}$ are related by

$$\vec{\mathbf{P}}(\mathbf{r}, t) = \epsilon_0 \int_{-\infty}^{t} \chi(\mathbf{r}, t - t')\vec{\mathbf{E}}(\mathbf{r}, t')dt' \tag{2.7}$$

where χ is the linear susceptibility which is a second rank tensor [4]. In an isotropic media, such as silica glass, χ can be assumed scalar. Combining Eqn. 2.1 - 2.7, we have

$$\nabla \times \nabla \times \vec{\mathbf{E}} = -\frac{1}{c^2}\frac{\partial^2 \vec{\mathbf{E}}}{\partial t^2} - \mu_0 \frac{\partial^2 \vec{\mathbf{P}}}{\partial t^2} \tag{2.8}$$

where the velocity of light in free space c is defined as $c = (\epsilon_0 \mu_0)^{-\frac{1}{2}}$. By introducing the Fourier transform in Eqn. 2.8, we have

$$\nabla \times \nabla \times \vec{\mathbf{E}}(\mathbf{r}, \omega) = \epsilon(\mathbf{r}, \omega)(\omega^2/c^2)\vec{\mathbf{E}}(\mathbf{r}, \omega) \tag{2.9}$$

where the frequency dependent dielectric constant is defined as

$$\epsilon(\mathbf{r}, \omega) = 1 + \chi(\mathbf{r}, \omega) \tag{2.10}$$

In general, ϵ is a complex number whose real and imaginary part are related to the material's refractive index (η) and absorption coefficient (α) by

$$\epsilon = (\eta + i\alpha c/2\omega)^2 \tag{2.11}$$

The frequency dependence of η is known as chromatic dispersion or material dispersion. If we assume that α is sufficiently low (for SSMF, this is true) and the material is isotropic (ϵ

is independent of $\mathbf{r}$), we can rewrite Eqn. 2.9 as

$$\nabla^2\vec{\mathbf{E}} + \eta^2(\omega)k_0^2\vec{\mathbf{E}} = 0 \tag{2.12}$$

using the identify $\nabla \times \nabla \times \vec{\mathbf{E}} = \nabla(\nabla \cdot \vec{\mathbf{E}}) - \nabla^2\vec{\mathbf{E}}$ and setting $\nabla \cdot \vec{\mathbf{E}} = 0$ using Eqn. 2.3 and Eqn. 2.5. k_0 is the free space wave number defined as $k_0 = \omega/c = 2\pi/\lambda$, and λ is the wavelength in free space.

Taking advantage of the cylindrical symmetry of optical fiber, Fig. 2.1, we can expand the axial component of Eqn. 2.12 in the cylindrical coordinates ρ, ϕ and z as

$$\frac{\partial^2 E_z}{\partial \rho^2} + \frac{1}{\rho}\frac{\partial E_z}{\partial \rho} + \frac{1}{\rho^2}\frac{\partial^2 E_z}{\partial \phi^2} + \frac{\partial^2 E_z}{\partial z^2} + \eta^2 k_0^2 E_z = 0 \tag{2.13}$$

where the step index of the optical fiber of core radius r_1 is of the form

$$\eta = \begin{cases} \eta_1, & \text{if } \rho > r_1 \\ \eta_2, & \text{if } \rho < r_1 \end{cases} \tag{2.14}$$

Equation 2.13 describes the propagation of guided modes [56] in an optical fiber, which is responsible for transporting signals in a fiber optic communication system. A mode is any solution of the wave equation (Eqn. 2.12) that satisfies appropriate boundary conditions. The vector symbol over $\mathbf{E}$ is removed for simplicity of notation. We focus on the axial component of the electric field, E_z, since the other components of the electric and magnetic field can be obtained using Maxwell's equations. The solutions of Eqn. 2.13 can be obtained using method of separation of variables,

$$\mathbf{E_z}(\rho, \phi, z) = F(\rho)\Phi(\phi)Z(z) \tag{2.15}$$

and are given by

$$Z = \exp(i\beta z) \tag{2.16}$$

$$\Phi = \exp(im\phi) \tag{2.17}$$

$$F(\rho) = \begin{cases} AJ_m(\kappa\rho) + A'Y_m(\kappa\rho), & \text{for } \rho \leq r_1 \\ CK_m(\gamma\rho) + C'I_m(\gamma\rho), & \text{for } \rho > r_1 \end{cases} \tag{2.18}$$

where $A, A', C,$ and C' are constants, J_m, Y_m, K_m and I_m are different kinds of Bessel functions [57], β is the propagation constant and m is an integer. The parameters κ and γ are given by

$$\kappa^2 = \eta_2^2 k_0^2 - \beta^2 \tag{2.19}$$

$$\gamma^2 = \beta^2 - \eta_1^2 k_0^2 \tag{2.20}$$

By applying the appropriate boundary conditions, one can obtain all the solutions of Eqn. 2.16 - 2.18 as follows

$$\mathbf{E}_z = \begin{cases} AJ_m(\kappa\rho)\exp(im\phi)\exp(i\beta z), & \text{for } \rho \leq r_1 \\ CK_m(\gamma\rho)\exp(im\phi)\exp(i\beta z), & \text{for } \rho > r_1 \end{cases} \tag{2.21}$$

In order to ensure that all modes are guided in Eqn. 2.21, κ and γ have to be greater than 0. Applying this condition to Eqn. 2.19 - 2.20, we obtain

$$\eta_2 > \bar{\eta} > \eta_1 \tag{2.22}$$

where $\bar{\eta} = \beta/k_0$ is the effective refractive index that the optical mode propagates with. If $\bar{\eta} = \eta_2$, the mode will not propagate. This condition is not of much interest. If $\bar{\eta} = \eta_1$, the mode will no longer be guided. This condition is of special interest as it defines when a

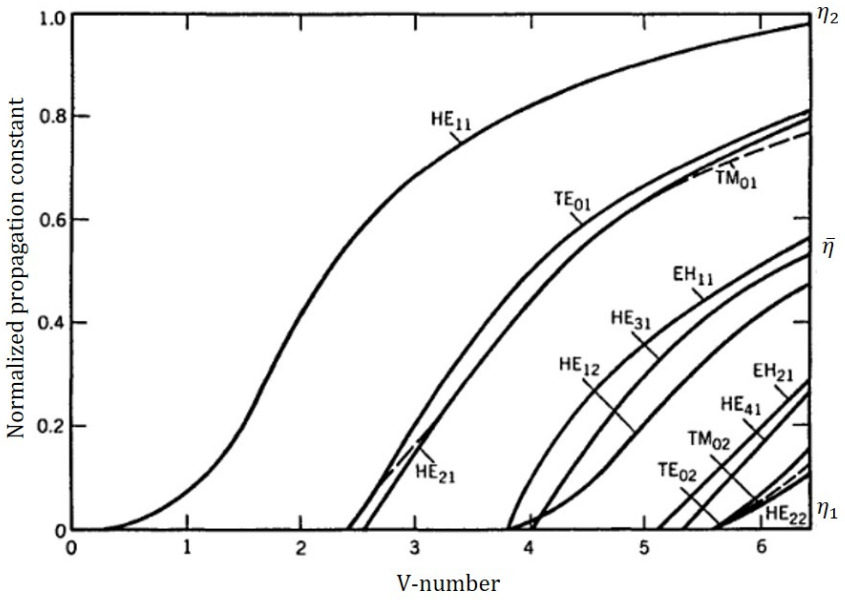

Figure 2.2: Normalized propagation constant as a function of normalized V-number for few low-order fiber modes in step index fiber. Right side scale shows the mode index $\bar{\eta}$ [4]

mode is "cut-off". We can define two parameters that play an important role in determining the cut-off condition, the V-number given by $V = k_0 r_1 (n_2^2 - n_1^2)^{-1/2}$ and the normalized propagation constant $b = (\bar{\eta} - \eta_1)/(\eta_2 - \eta_1)$. The cut-off condition for different optical guided modes in a step-index fiber is shown in Fig. 2.2.

In order to prevent signal degradation from the mixing of different optical modes, SSMF is designed with a V-number$<$2.405 so as to support only one mode, Fig. 2.2. Specification of SSMF are as follows: r_1 = 4 μm, r_2 = 62.5 μm and $\eta_2 - \eta_1$ = 0.003. At λ = 1550 nm, the V-number of SSMF is $\sim$ 2.27.

2.2.2 Chromatic Dispersion

There exists two types of dispersion in any waveguide - inter-modal dispersion and intra-modal dispersion. Inter-modal dispersion can be ignored in SSMF owing to its design, but intra-modal dispersion affects the propagation of optical signals significantly. In an optical fiber, the group velocity associated with the any mode in the fiber is frequency dependent because of CD. As a result, different spectral components of an optical signal travel at

different velocities introducing intra-modal dispersion and ISI in the optical signal.

Let us consider a piece of SSMF of length L. A specific spectral component at frequency ω would arrive at the output of the fiber after time $T = L/v_g$, where v_g is the group velocity defined as

$$v_g = \frac{d\omega}{d\beta} \tag{2.23}$$

and β is the propagation constant from Eqn. 2.21. Let us now consider a pulse with a spectral width of $\Delta\omega$. The extent of time domain pulse broadening is then given by [4]

$$\Delta T = \frac{dT}{d\omega}\Delta\omega = L\frac{d}{d\omega}\left(\frac{1}{v_g}\right)\Delta\omega \tag{2.24}$$

Substituting Eqn. 2.23 in Eqn. 2.24, we get

$$\Delta T = L\frac{d^2\beta}{d\omega^2}\Delta\omega = L\beta_2\Delta\omega \tag{2.25}$$

The parameter $\beta_2 = d^2\beta/d\omega^2$ is known as the group-velocity dispersion (GVD) parameter. In optical communication engineering, it is preferred to determine ΔT in terms of the wavelength content $\Delta\lambda$. By substituting $\omega = 2\pi\lambda/c$, we get

$$\Delta T = -\frac{2\pi c}{\lambda^2}\beta_2 L\Delta\lambda = DL\Delta\lambda \tag{2.26}$$

where $D = -(2\pi c/\lambda^2)\beta_2$ is known as the dispersion parameter and is expressed in terms of ps/nm/km. The dispersion parameter is 0 ps/nm/km for DSF, $\sim$3 ps/nm/km for NZDF and 17 ps/nm/km for SSMF.

Chromatic dispersion has two components - material dispersion, caused by silica glass, and waveguide dispersion, caused by the design of the fiber. By substituting $\beta = \bar{n}k_0$ and

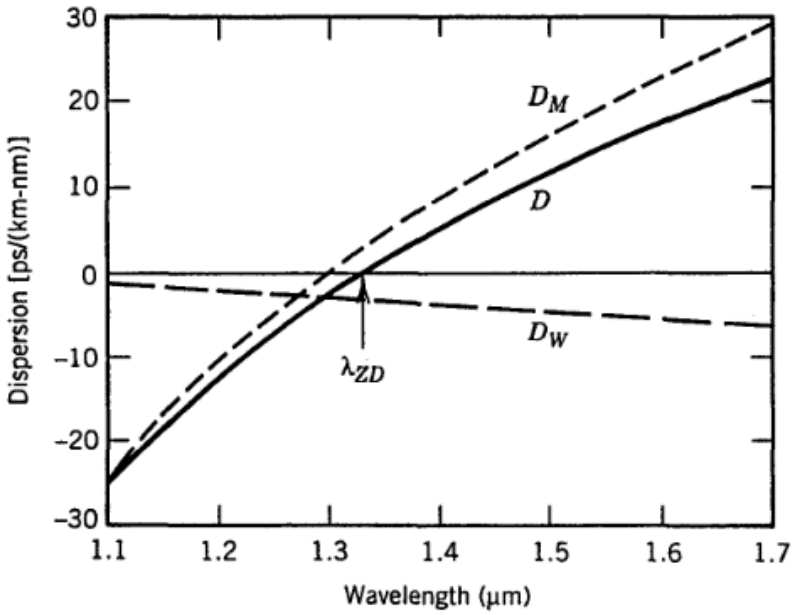

Figure 2.3: Total dispersion D, along with its constituent material dispersion D_M and waveguide dispersion D_W, as a function of wavelength. The zero dispersion wavelength is also indicated as λ_{ZD} and occurs around 1.31 μm [4]

$b = (\bar{\eta} - \eta_1)/(\eta_2 - \eta_1)$ in Eqn. 2.26, we obtain

$$D = \frac{1}{c}\frac{d\eta_{1g}}{d\lambda} + \frac{2\pi\Delta}{\lambda^2}\left[\frac{\eta_{1g}^2}{\eta_1\omega}\frac{Vd^2(Vb)}{dV^2} + \frac{d\eta_{1g}}{d\omega}\frac{d(Vb)}{dV}\right] \tag{2.27}$$

$$= D_M + D_W \tag{2.28}$$

where D_M and D_W are the material and waveguide dispersion respectively, $\Delta = \eta_2 - \eta_1$ and η_{1g} is the group index of the cladding. Figure 2.3 shows the variation of CD as a function of wavelength for SSMF.

2.2.3 Polarization Mode Dispersion

Even though an SSMF is designed to support only one optical mode that satisfies the wave equation (Eqn. 2.21), there actually exists two degenerate solutions to the wave equation since the electric field associated with the electromagnetic wave can be oriented in two orthogonal directions. These degenerate solutions are known as the two polarization com-

ponents of the fiber mode. In a perfectly cylindrical optical fiber, these two components would have the same propagation constant β. However, in reality, there are imperfection in the manufacturing of fiber and each polarization has its own propagation constant, β_x and β_y, causing time delays between the two polarizations. Additionally, there is also random coupling between the two polarizations due to various types of stress and microbending in an optical fiber. The combined effect of these two phenomena is known as polarization mode dispersion (PMD) [58].

In the past, dispersion associated with PMD induced significant penalties in an optical communication system. However, modern fibers are now made by employing a twisting motion in the fiber draw process known as the "GULP method" [59]. The method has reduced the associated dispersion to $\sim$0.1 ps/$\sqrt{\text{km}}$ for SSMF and is negligible for short distances of fiber. However, for long optical links employing high speed PDM signals, PMD is an important impairment that needs to be mitigated using DSP.

2.2.4 Loss

While solving for wave propagation through an optical fiber, we had identified that the frequency dependent dielectric constant ϵ was a complex number whose real part was related to the refractive index (η) of the material and the imaginary part was related to the absorption coefficient (α) of the material (see Eqn. 2.11). However, in general, there are many sources of attenuation in an optical fiber and α can be generalized as the absorption coefficient for all sources of optical attenuation. The power attenuation in an optical fiber is governed by $dP/dz = -\alpha P$, where z is the transport distance. Therefore, if P_{in} is launched through a fiber of length L, $P_{out} = P_{in}e^{-\alpha L}$. The units of α is dB/km.

There are three sources of losses in an optical fiber - material absorption, Rayleigh scattering and waveguide imperfection. Material absorption can be divided into two categories - intrinsic absorption caused by pure silica glass and extrinsic absorption caused by impurities in the fiber. Any material absorbs at certain wavelengths owing to electronic and

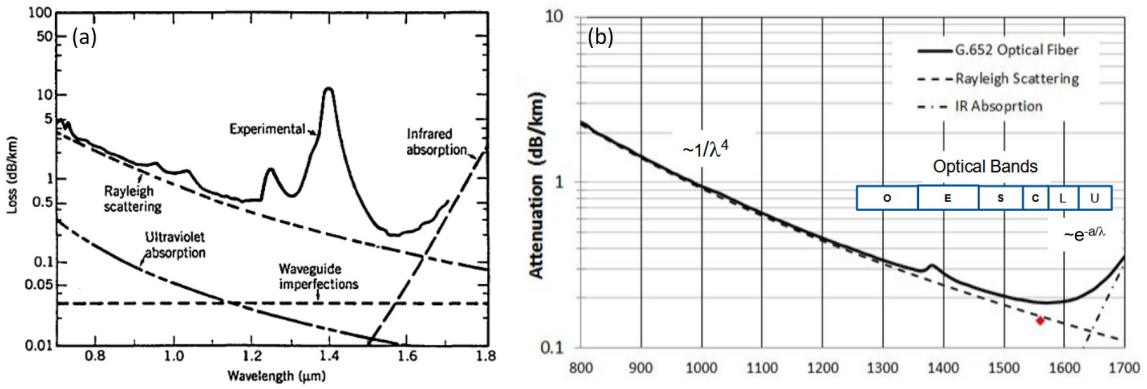

Figure 2.4: (a) Spectral loss profile of a single-mode fiber with wavelength dependence of fiber loss for several fundamental loss mechanism [4]. (b) Spectral loss profile for modern SSMF fiber [60]

vibrational resonances. For silica glass, electronic resonance occurs in the ultraviolet region (λ <0.4 μm) and vibrational resonance occurs in the infrared region (λ >7 μm). The tails of their absorption bands extend into the visible region introducing material absorptions of <0.1 dB/km between 0.8 μm and 1.6 μm, Fig. 2.4, creating the first fundamental limit on the absorption coefficient. The main source of extrinsic material absorption are water vapors. The vibrational resonance of OH ions occurs at 2.73 μm and its harmonic tones have strong absorption at 1.39 μm, 1.24 μm and 0.95 μm, Fig. 2.4(a). In the past, these impurities could introduce losses as high as 10 dB/km. However, modern SSMF are created with sufficient purity and have minimal OH ion absorption, Fig. 2.4(b).

Rayleigh scattering is a fundamental loss mechanism caused by local microscopic fluctuations in the density of the material. These microscopic fluctuations lead to random fluctuations in the refractive index of the material on a scale smaller than the optical wavelength λ, leading to scattering of light in the media [13]. The loss varies as λ^{-4} and is dominant at short wavelengths. In an optical fiber, Rayleigh scattering is the dominant cause of loss introducing 0.12 - 0.16 dB/km power losses at 1.55 μm wavelength, Fig. 2.4.

An ideal single mode fiber would guide an optical mode with no energy leakage into the cladding layer. However, real fiber have imperfections at the core-cladding layer that can lead to additional losses in the fiber. The physical phenomenon behind this loss is known

as Mie scattering [13]. These losses can be minimized by ensuring that the core radius does not vary significantly along the fiber length during manufacturing. Modern fibers present $<$0.03 dB/km losses from Mie scattering. Additionally, losses can also be introduced due to mechanical bends in the optical fiber. Mechanical bends have a bend radius of at least 5 mm and losses at these bend radii are $<$0.01 dB/km.

Total fiber losses from all these sources can be limited to $\sim$0.2 dB/km for commercial SSMF, Fig. 2.4, with research showing record lowest fiber loss of 0.1419 dB/km at 1.56 μm wavelength and 1290 °C operating temperature [61].

2.2.5 Fiber Nonlinearity

Light scattering and absorption form one type of loss mechanism in an optical fiber. There exists another type of loss mechanism where power from a certain wavelength is transferred to another wavelength coherently. These effects give rise to nonlinearities in the fiber. They not only take power from the propagating signal but also introduce distortions in the signal, further degrading the optical system's performance.

Two examples of such effects are Raman scattering [62] and Brillouin scattering [63]. Both these effects absorb power from a certain wavelength and transfer it to a higher wavelength. The main difference between the two is that Raman scattering occurs due to optical phonons and Brillouin scattering occurs due to acoustic phonons. Fortunately, both these effects occur at very high optical powers in an optical fiber and do not contribute to losses in optical communication systems. These effects are however used to create optical amplifiers for various application [64, 65]. Raman amplifiers are commonly used in long-haul optical communication systems owing to its low noise figures [66].

Another source of optical nonlinearity in an optical fiber is the nonlinear refractive index of silica glass. While deriving the equations for wave propagation in a step index fiber in Sec. 2.2.1, we had assumed that the susceptibility χ of silica glass is linear and χ is a second rank tensor. However, as the incident powers in an optical fiber rise, this linear

dependence is no longer valid. In such a case, the relationship between the polarization ($\vec{\mathbf{P}}$) and the electric field ($\vec{\mathbf{E}}$) is given by

$$\vec{\mathbf{P}} = \epsilon_0 \left[\chi^{(1)} \cdot \vec{\mathbf{E}} + \chi^{(2)} : \vec{\mathbf{E}}\vec{\mathbf{E}} + \chi^{(3)} \vdots \vec{\mathbf{E}}\vec{\mathbf{E}}\vec{\mathbf{E}} + \cdots \right] \tag{2.29}$$

where $\chi^{(j)}$ is the j^{th} order susceptibility and is a tensor of rank $j+1$. Previously, we only utilized $\chi^{(1)}$ in Eqn. 2.10 to compute the refractive index of the media, but now we need to utilize Eqn. 2.29 in Eqn. 2.10 to compute the total refractive index of an optical fiber.

Silica is a symmetric molecule. Therefore, $\chi^{(2)} = 0$ and Eqn. 2.29 approximates to

$$\vec{\mathbf{P}} = \epsilon_0 \left[\chi^{(1)} \vec{\mathbf{E}} + \chi^{(3)} \vec{\mathbf{E}}^3 \right] \tag{2.30}$$

Let us assume that the incident optical field in an optical fiber is a monochromatic wave of frequency ω,

$$\mathbf{E} = \mathbf{E}_0 e^{-\jmath\omega t} \tag{2.31}$$

Therefore, the real part of the optical field is given by

$$\Re[\mathbf{E}] = \frac{1}{2} \left[\mathbf{E}_0 e^{(-\jmath\omega t)} + \mathbf{E}_0 e^{(\jmath\omega t)} \right] \tag{2.32}$$

$$\Rightarrow \Re[\mathbf{E}^3] = \frac{1}{8} \left[\mathbf{E}_0^3 e^{(-3\jmath\omega t)} + \mathbf{E}_0^3 e^{(3\jmath\omega t)} + 3|\mathbf{E}|^2 \left(\mathbf{E}_0 e^{(-\jmath\omega t)} + \mathbf{E}_0 e^{(\jmath\omega t)} \right) \right] \tag{2.33}$$

where $\Re[x]$ is the real part of the x. Note that the vector signs have been omitted for ease of notation. The third harmonic electromagnetic wave becomes significant under a special condition known as phase-matching. We will ignore this component for now. Substituting

Eqn. 2.33 in Eqn. 2.30, we get

$$\Re[\mathbf{P}] = \epsilon_0\chi^{(1)}\Re[\mathbf{E}] + \epsilon_0\chi^{(3)}\Re[\mathbf{E}]^3 \tag{2.34}$$

$$= \epsilon_0\left(\chi^{(1)} + \frac{3|\mathbf{E}_0|^2}{4}\chi^{(3)}\right)\mathbf{E}_0 \tag{2.35}$$

$$\Rightarrow \eta'^2 = 1 + \chi^{(1)} + \frac{3|\mathbf{E}_0|^2}{4}\chi^{(3)} \tag{2.36}$$

$$= \eta^2 + \frac{3|\mathbf{E}_0|^2}{4}\chi^{(3)} \tag{2.37}$$

where η' is the total refractive index and η is the refractive index under the assumption of linearity. The second term on the right hand side represents the nonlinear refractive index as the index itself depends on the incident optical power. Typically, this index is smaller than the linear refractive index and we can simplify Eqn. 2.37 to

$$\eta' = \eta\left(1 + \frac{3|\mathbf{E}_0|^2}{4\eta^2}\chi^{(3)}\right)^{-1/2} \tag{2.38}$$

$$\approx \eta + \frac{3|\mathbf{E}_0|^2}{8\eta^2}\chi^{(3)} \tag{2.39}$$

using the following approximation $(1+x)^{-1/2} \approx 1 + x/2$ if $x \ll 1$. Equation 2.39 can be further simplified as

$$\eta' \approx \eta + \eta_2|\mathbf{E}_0|^2 \tag{2.40}$$

where $\eta_2 = 3\chi^{(3)}/8\eta^2$ is known as the Kerr coefficient [67]. For silica, $\eta_2 \approx 3 \times 10^{-20}$ m^2/W. Therefore, to experience 3×10^{-20} change in refractive index, one would need 1 W of incident optical power in a cross-section area of 1 m^2. This change in refractive index may seem insignificant. However, the cause of nonlinear distortions in a fiber is not the high incident power, but the low cross-sectional area of the fiber and the lengths over which these interactions take place. An SSMF has a cross-sectional area of 100 μm^2 or less and transports signals over 1000s of kilometers. The variation in refractive index in such a

situation is comparable to the linear refractive index itself.

Fiber nonlinearities distort the optical signal through three processes, namely self-phase modulation (SPM), cross-phase modulation (XPM) and four-wave mixing (FWM). SPM occurs when the variation in power in a wavelength affects the signal on that wavelength. It introduces the least distortion of all nonlinear processes in an optical fiber. XPM occurs when the power variation in a wavelength affects the signal on another wavelength. One might consider XPM to be the significant source of nonlinear distortions in an optical fiber since modern SSMF carry signals on $\sim$80 wavelengths at a time. However, if the channels are sufficiently spaced and there is sufficient CD present in the link, the effects of XPM is significantly reduced [68]. FWM is a process where a fourth wavelength is created due to the interaction of two or three wavelengths. FWM is the most significant source of nonlinear distortions in an optical fiber. Its impact on an optical communication system can be reduced by increasing the spacing between signal wavelengths, increasing the CD, and using unequal spacings between wavelengths [68]. The first two recommendations reduce the efficiency of the phase matching condition required for FWM, whereas the latter results in FWM wavelength generation outside the signal bands.

2.2.6 Miscellaneous

Apart from these four major impairments - loss, CD, PMD and nonlinearities, there exist a few other impairments such as polarization dependent loss (PDL) [69], multipath interference (MPI) [70], changes in state of polarization (SoP) [71], higher order CD [5] etc. However, these either have little impact on the signal or are very localized. These impairments will not be discussed here.

2.3 Transmitters, Receivers, and other Optical Components

While optical fiber is an important part of an optical communication system, there are many other optical components that enable communication in these optical links. In this section,

we talk about what these components are, why they are used in an optical communication system and what limitations/impairments they introduce in these systems.

2.3.1 Lasers

Laser is the acronym for light amplification by stimulated emission of radiation. They are widely used in the modern day for various applications such as optical disk drives, laser printers, fiber-optic communication systems etc. All lasers consist of a pump source, a gain medium and two or more mirrors that form an optical resonator [4]. By carefully choosing these components, one can design a laser for a wide variety of wavelengths and optical powers. The most commonly used lasers in fiber-optic communication systems include VCSELs, distributed feedback (DFB) lasers and external cavity lasers (ECL). VCSELs are primarily used in short-reach communication systems employing multimode fiber, since they can only produce sufficient optical power using multiple optical modes [72]. These systems are significantly different from communication systems that utilize SSMF, and therefore will not be discussed here. Interested readers are directed towards Appendix B.

Ideally, a laser used in an optical communication system would output a single longitudinal mode, i.e. it is a monochromatic source of light. However, real lasers exhibit fluctuations in its intensity, phase and frequency even when operating at steady conditions [73]. The fundamental source of these distortions is spontaneous emission. Apart from the coherent stimulated photons in the laser, there also exist spontaneously emitted photons that add random phase to the stimulated emissions and perturb the amplitude and phase of the laser output in a random manner. These perturbations impair the communication signal by introducing random phase noise whose variance is given by

$$\sigma^2(\tau) = 2\pi\Delta f\tau \tag{2.41}$$

where Δf is the full-width half-maxima (FWHM) of the laser linewidth (3-dB width of the

output of the laser spectra) and τ is the time between measurements. The added phase noise evolves with time (τ) and is compensated using DSP in coherent communication systems.

2.3.2 Electronic Converters

Electronic converters allow us to convert signals between the analog and digital domains seamlessly. This enables the use of DSP in communication systems to compensate for physical impairments and achieve high data rates. The performance of an EC depends on the following parameters - bit resolution, timing jitter, sample rate, analog bandwidth and noise [74]. Signal-to-noise-and-distortion ratio (SINAD) attempts to quantify the impact of these parameters on a converted signal. It is measured at individual frequencies and is given by [75]

$$\text{SINAD}(f) = \frac{P_{signal} + P_{noise} + P_{distortion}}{P_{noise} + P_{distortion}} \tag{2.42}$$

where P_{signal} is the power of the input sinusoidal wave at frequency f, $P_{distortion}$ and P_{noise} in the numerator is the power of the noise and distortion at frequency f and in the denominator is the power of noise and distortion measured over the entire bandwidth of interest. A more common metric that is used to describe the performance of an EC is the ENoB. It is a measure of how well the signal is being converted between the two domains by an EC (analog and digital) and is related to the SINAD by [75]

$$\text{ENoB} = 0.5 \times \log_2(\text{SINAD}) - 0.5 \times \log_2(1.5) \tag{2.43}$$

A detailed description on the relationship between ENoB and SINAD can be found in appendix A. Limited EC ENoB can affect the performance of optical communication systems and is an important design factor when deploying optical links. There has been some effort in using DSP to overcome the limitations of limited ENoB [76, 77].

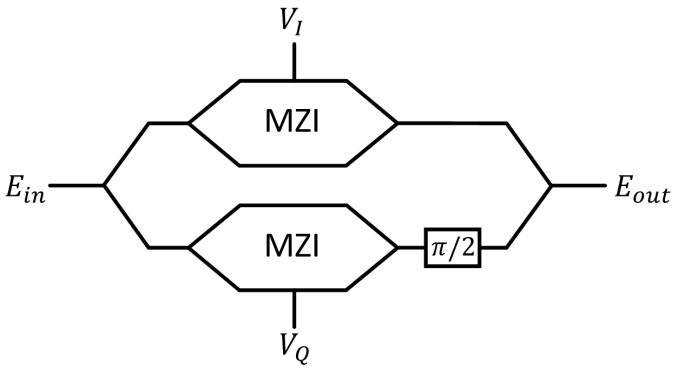

Figure 2.5: IQ modulator constructed using two MZIs and a phase shifter

2.3.3 Modulators and Drivers

Optical communication systems often employ optical modulators to convert the electrical communication signal from an EC to the optical domain. These modulators usually work on the principle of Pockel's effect [78] and are made of substances (e.g. lithium niobate) that strongly demonstrate these properties. Pockel's effect allows one to change the refractive index of a material to introduce phase variation in the optical signal, which can then be used interferometrically to create amplitude variations. Such devices are called Mach-Zehnder Interferometer (MZI) and their transfer function is given by

$$E_{out} = E_{in} \cos\left(\frac{\pi V_{in}}{V_\pi}\right) \tag{2.44}$$

where E_{in} is the input optical field, E_{out} is the output optical field, V_π is the voltage required to obtain a phase shift of π on E_{in}, and V_{in} is the applied voltage that contains the communication signal. Using two such MZIs, it is possible to create an I/Q modulator that can construct complex communication signals, Fig. 2.5.

Optical modulators are inherently nonlinear owing to its sinusoidal transfer function, Eqn. 2.44. They can introduce nonlinear distortions to communication signals and degrade link performance. In order to minimize these distortions, modulators are usually operated in their linear regime. However, this comes at the cost of reduced modulation depth. A

careful trade-off between these two phenomena is required to obtain optimal performance.

Some optical transmitters also use driver amplifiers to amplify the output of an EC before passing it to the optical modulator. Higher voltages improve the quality of the signal by increasing the modulation depth. However, drivers add their own distortions and may need additional DSP to compensate them to obtain best system performance.

Lasers, optical modulators, electronic drivers and digital-to-analog converters together comprise of an optical transmitter. Some optical transmitters also include digital/analog filters to pre-compensate the optical signal for system impairments.

2.3.4 Optical Amplifiers

Erbium doped fiber amplifiers and distributed Raman amplifiers are two of the most common optical amplifiers used in optical communication systems. Optical amplifiers allow for the compensation of fiber propagation losses and enable transmission of optical signals through 1000s of kilometers of optical fiber. However, similar to electronic amplifiers, optical amplifiers degrade the quality of the amplified signal at every amplification stage [79]. This degradation is quantified by the amplifier-noise figure F_n and is defined as

$$F_n = \frac{(\text{OSNR})_{in}}{(\text{OSNR})_{out}} \tag{2.45}$$

where OSNR is the optical signal-to-noise ratio, a metric used to define the quality of the optical signal. It is related to the signal-to-noise ratio (SNR) as follows [80]

$$\text{OSNR} = \frac{pR_s}{2B_{ref}}\text{SNR} \tag{2.46}$$

where p is the number of polarizations, R_s is the symbol rate, and B_{ref} is the resolution bandwidth commonly chosen as 0.1 nm or 12.5 GHz. Experimentally, the OSNR is calculated using the optical spectra obtained from an optical spectrum analyzer (OSA), by measuring the power difference between the signal and the noise floor, Fig. 2.6. The noise

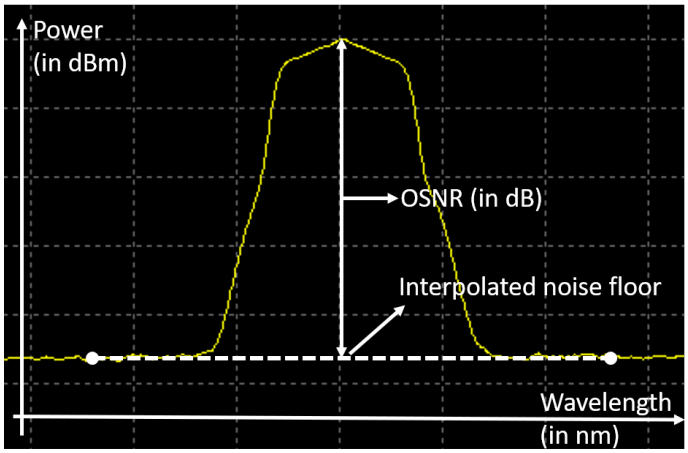

Figure 2.6: Output of an OSA showing the optical spectra and the associated calculations to measure the OSNR of the optical signal

floor at the signal wavelength is obtained by interpolating the out-of-band noise floor. All measurements are done with 0.1 nm resolution bandwidth. If any other bandwidth is used, the following correction factor needs to be added to the OSNR: $10\log_{10}(BW/0.1)$, where BW is the measurement resolution bandwidth in nanometers.

The optical amplifier noise figure is conventionally expressed as [79]

$$F_n = 2n_{sp}\chi \tag{2.47}$$

where n_{sp} is the spontaneous emission factor and χ is the excess noise coefficient. In an ideal amplifier, $n_{sp} = 1$ and $\chi = 1$ demonstrating that the best achievable noise figure is 3 dB. Distributed Raman amplifiers operate near this noise figure since they achieve near complete population inversion ($n_{sp} \sim 1$). EDFA noise figures range from 4 dB to 8 dB since they do not achieve complete population inversion ($n_{sp} > 1$). Even though Raman amplifiers have lower noise figures, EDFAs are more popular since Raman amplifiers are costly and have low power efficiencies. Raman amplifiers are extensively used in long-haul optical communication systems where low noise figures are crucial [66].

For an optical link employing N uniformly spaced EDFAs, the output OSNR (in dB) is

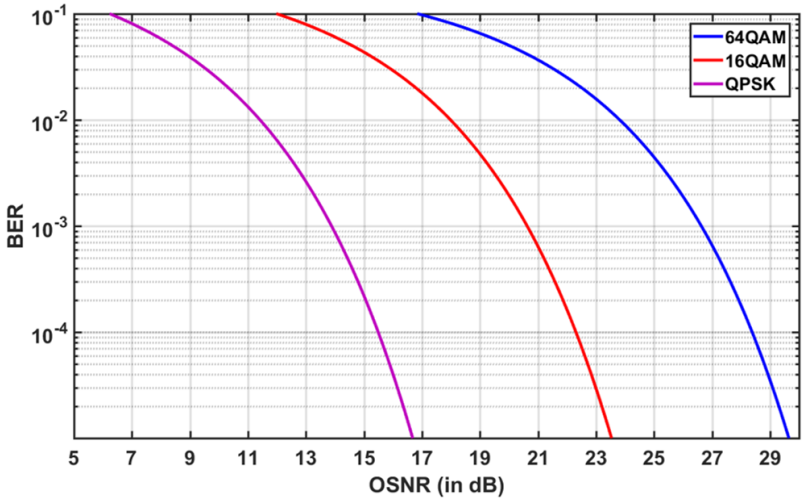

Figure 2.7: BER vs OSNR for 32 GBaud QPSK, 16QAM and 64QAM

given by [81]

$$\text{OSNR} = P_0 + 58 - \Gamma - 10\log_{10}(N) - F_n \tag{2.48}$$

where P_0 is the total optical power launched into the fiber from an EDFA and Γ is the gain of the EDFA. The number of amplifiers and the noise figure of individual amplifiers strongly affect the maximum achievable OSNR, thereby limiting the performance of a long haul communication link. Figure 2.7 shows the BER performance of 32 GBaud QPSK, 16QAM and 64QAM for various OSNR [80].

2.3.5 Reconfigurable Optical Add Drop Multiplexers

A ROADM is an optical device that can selectively add channels to or drop channels from an optical network employing multiple wavelengths. They are widely used in optical communication systems to enable optical networking. The basic building block of a ROADM is a WSS which can be constructed using various technologies including micro-mirror arrays, planar lightwave circuits (PLC), liquid crystal on silicon (LCoS) etc [82]. WSS are designed for a fixed wavelength channel plan - fixed channel spacing centered around certain wavelengths and fixed pass-bands. Similar to other optical components in an optical

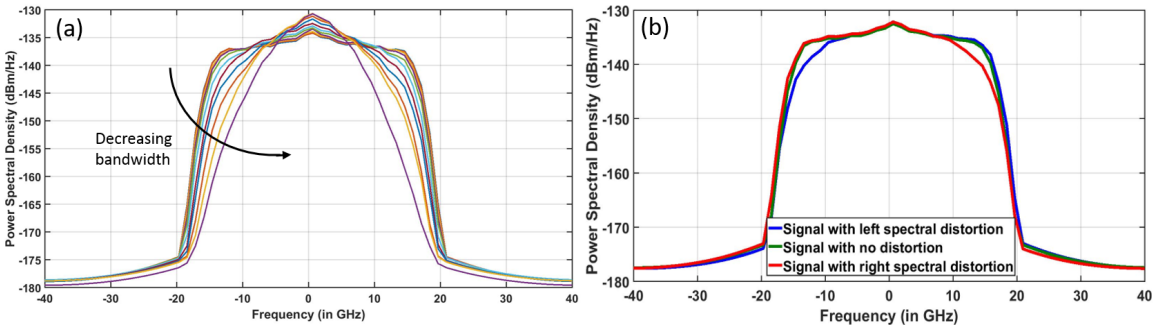

Figure 2.8: Power spectral density of received optical signal affected by (a) narrowing pass-band profile (b) frequency drifts between ROADM pass-band and channel wavelength

communication system, ROADMs also introduce impairments in an optical link and need to be carefully managed to minimize these impairments.

Finite pass-band isolation and imperfect filter shapes of switching elements introduce cross-talk between adjacent wavelengths (also known as interchannel interference or ICI) in an optical network employing ROADMs. These impairments occur at every add-drop stage and accumulate over the lightpath, severely degrading the performance of an optical link [83]. Currently, optical networks rely on high out-of-band suppression to contain the impact of ICI. However, aging equipment can further enhance these cross-talk and timely repairs/replacements are necessary to ensure best performance. ROADMs can also introduce impairments in the pass-band through two mechanisms - narrowing pass-band profile due to cascaded ROADMs, and frequency drifts between the ROADM pass-band and channel wavelengths [84]. Both these mechanisms introduce unnecessary filtering effects on the pass-band channel and degrade system performance, Fig. 2.8. Careful identification of these impairments are crucial to ensure continued network operations.

2.3.6 Photodiodes

All optical communication systems use photodiodes to convert the optical signal to the electrical domain for further processing. A photodiode is characterized by its responsivity

R defined as [5]

$$R = \eta \frac{\lambda_0}{1.24} \tag{2.49}$$

where η is the quantum efficiency and λ_0 is the wavelength of the incident light in μm. A photodiode responsivity determines the output photocurrent governed by $I_{PC} = RP_I$, where P_I is the incident optical power and I_{PC} is the output photocurrent.

There are two sources of noise in a photodiode - shot noise and thermal noise [85]. Shot noise is caused by the random distribution of electrons generated during the photodetection process. The variance of this noise is given by $\sigma^2_{shot} = 2qI_{PC}B$, where q is the charge of an electron and B is the bandwidth of the receiver. Thermal noise is generated due to the random motion of electrons. The variance of thermal noise is given by $\sigma^2_{thermal} = 4k_BTB/R$, where k_B is the Boltzman's constant, T is the absolute temperature and R is the load resistance. In the absence of optical amplifiers, these two noise sources dominate the performance of a link. Therefore, they are limiting factors in the performance of short reach optical communication systems.

In some optical communication systems, the output of a photodiode does not have sufficient power to meet performance requirements. In such cases, a transimpedance amplifier (TIA) is used to amplify the photocurrent. However, these amplifiers add noise and nonlinearities to the signal and degrade the performance. TIAs are common in direct detect systems where messages are modulated on the intensity of light. Since it is not possible to extract phase information in these systems to perform DSP, they are cheaper to implement.

2.3.7 Coherent Receivers

Coherent receivers enable the extraction of phase information from the optical signal thereby allowing complex modulation formats and advanced DSP. Their advent has enabled record data rates and distances in optical communication systems. There are various types of co-

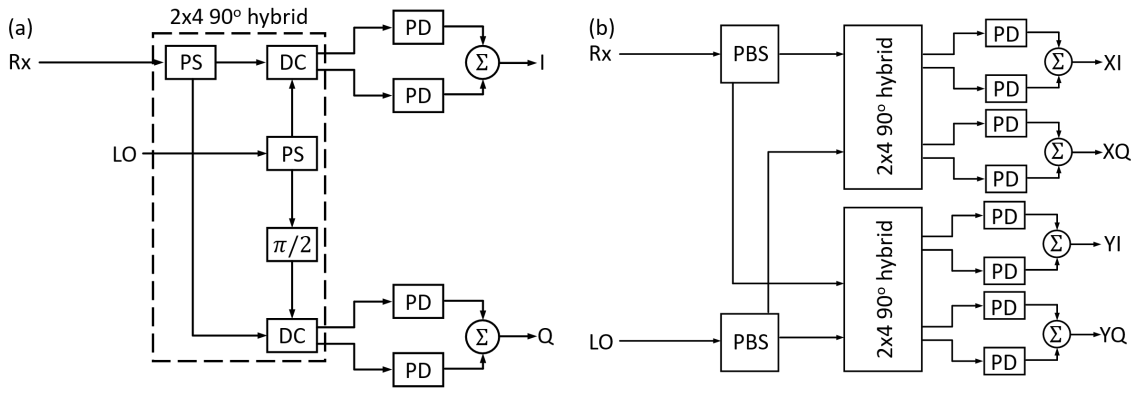

Figure 2.9: (a) One polarization branch of a coherent receiver describing a 2x4 90 degree hybrid. (b) A fully coherent dual polarization balanced receiver. PS: power splitter, $\pi/2$: 90 degree phase shifter, DC: directional coupler, PD: photodiode, PBS: polarization beam splitter and Σ: electrical adder

herent receivers [5]. Here, we will discuss the architecture of a dual polarization balanced coherent receiver that is typically used in long haul links. For simplicity in the following discussion, a coherent receiver refers to a dual polarization balanced coherent receivers.

A coherent receiver consists of a local oscillator, polarization beam splitters (PBS), power splitters, phase shifters, balanced photodiodes and directional couplers, Fig. 2.9. Coherent receivers usually don't employ TIAs since they can achieve higher photocurrents by increasing the local oscillator power. The input to a coherent receiver is the received optical signal and the local oscillator. Both signals first go through a PBS to be split into their individual polarizations. These then go through power splitters and one component of the local oscillator gets delayed by $\pi/2$ phase in order to extract the in-phase (I) and quadrature (Q) component of the signal, Fig. 2.9(a). The outputs are then passed through a directional coupler where they coherently mix with each other and sent to photodiodes to obtain the electrical signals. A balanced photodiode is usually employed to eliminate common mode noise and distortions. The outputs of the coherent receiver are the I and Q component of the X and Y polarization, Fig. 2.9(b). A detailed description of a coherent receiver can be found in [5].

The most common impairment in a coherent receiver is called frequency offset [86].

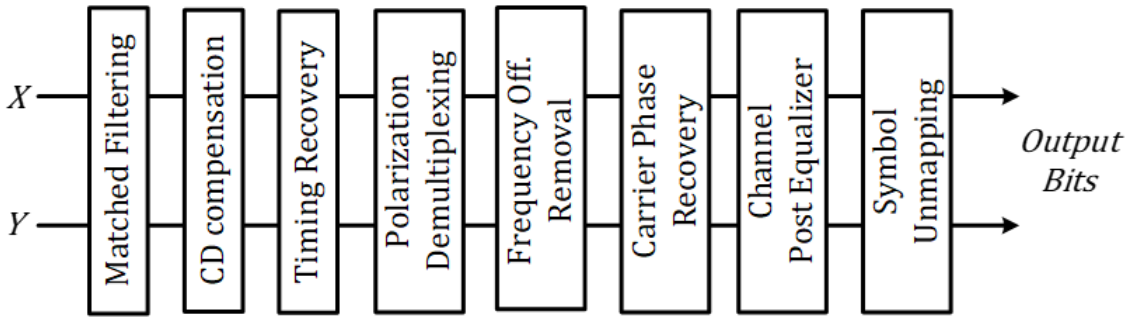

Figure 2.10: Common receiver DSP architecture used in coherent communication links

In general, there is a small difference in operating frequencies between the local oscillator laser and the transmitter laser. When the two lasers beat at the photodiode, this frequency difference is transferred to the received symbols causing growing phase offsets between symbols. Using the same laser at the transmitter and receiver can eliminate this impairment, but this solution is not practical in long optical links where the transceivers can be 1000s of kilometers away. DSP based techniques are currently employed to eliminate frequency offset. Other impairments in a coherent receiver include imbalance in the photodiodes, power splitters, directional couplers etc. However, modern optical components have negligible imbalances and their associated impairments can be usually ignored [87].

2.4 Digital Signal Processing

Since 2009, optical communication systems have seen an increased use of DSP techniques to increase data rates through optical fiber. These techniques allow for the compensation of all link impairments that were discussed in the previous section and the use of advanced modulation formats that can transport more information per unit time. In this section, we discuss common modulation formats that are implemented in optical communication systems and the associated DSP algorithms, Fig. 2.10.

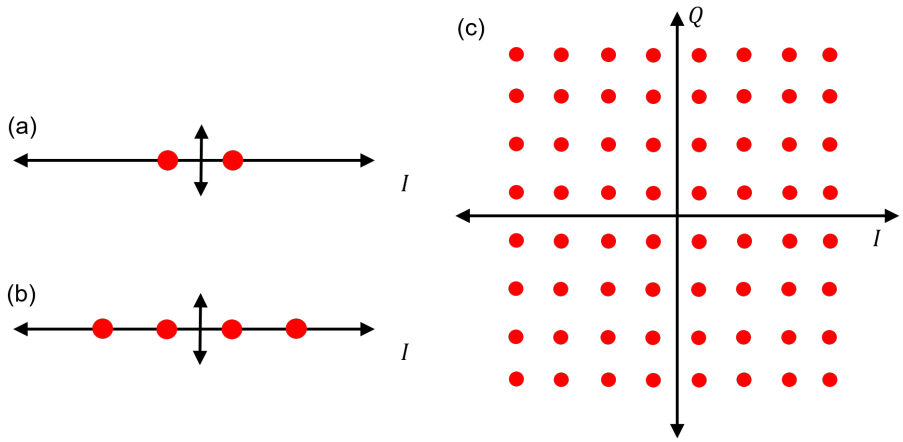

Figure 2.11: (a) PAM-2 (b) PAM-4 (c) 64-QAM

2.4.1 Advanced Modulation Formats

Modulation is the process of mapping a sequence of bits to a signal to make it suitable for transportation over a communication media. The most common types of modulation formats are pulse amplitude modulation (PAM) and quadrature amplitude modulation (QAM) [88]. PAM signals modulate the field or intensity of light into multiple amplitude levels. PAM-2 and PAM-4, employing two and four amplitude levels respectively, are the most common types of PAM signals in optical communication. QAM signals have double the capacity of PAM signals since they modulate PAM signals on the optical fields of two orthogonal carriers - $\sin(\omega_c t)$ and $\cos(\omega_c t)$. 4-, 8-, 16-, 32- and 64-QAM are the most commonly used QAM modulation formats in optical communication systems. Figure 2.11 shows constellation diagrams for some of these modulation formats.

In order to maximize capacity in an optical link [40], one needs to operate at a particular spectral efficiency allowed by the available OSNR in the optical channel. The spectral efficiency of a modulation format is defined as $\log_2(M)$, where M is the number of possible symbols in a modulation format. For example, 64-QAM has a spectral efficiency of 6. PAM and QAM signals can only allow for integer spectral efficiencies, which is not optimum in many cases. Therefore, some optical communication systems use time-domain

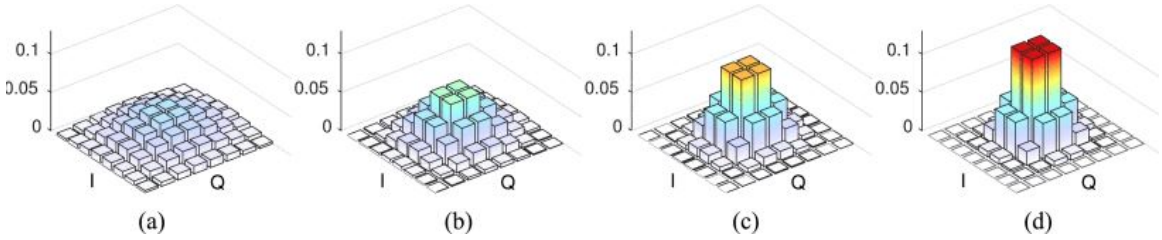

Figure 2.12: Probabilistically shaped 64-QAM constellation with various Boltzmann probability distributions [89]

hybrid modulation formats (TD-HMF) to achieve non-integer spectral efficiency by time interleaving two or more types of modulation format. While individual time periods have integer spectral efficiency, the average efficiency can be non-integer.

The achievable granularity in spectral efficiency of TD-HMFs is restricted by the complexity of the time-interleaving scheme. Beyond a certain interleaving complexity, the associated DSP becomes expensive and impractical, and alternate schemes are necessary to achieve maximum capacity in an optical link. Probabilistically shaped constellations provide an alternate methodology to achieve such granularity [89]. By assigning non-uniform probabilities to constellation points, one can change the associated entropy and thereby its spectral efficiency, Fig. 2.12. Probabilistic shaping has been well received by the optical communication industry due to its relative ease of implementation based on the constant composition distribution-matching (CCDM) scheme [90]. It was successful demonstrated in a trans-Atlantic link in 2018 [91], just three years after its introduction.

Higher modulation formats require higher signal powers (or OSNR) to maintain the same BER in an optical link. Increasing the optical power introduces nonlinear fiber penalties, affecting system performance. In order to minimize these penalties, alternate constellation shapes have been explored in the past that are not based on square lattices like traditional PAM and QAM. The process of shaping constellation in this manner is known as geometric shaping. In [92], 16-QAM constellations tolerant to linear/nonlinear phase noise were demonstrated to improve performance by 1.1 dB over traditional square QAM. Similarly, in [93], 16 point ring constellations were demonstrated to improve performance

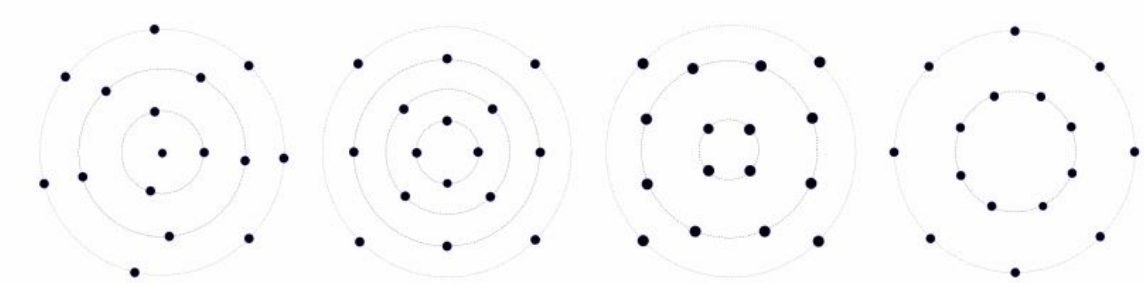

Figure 2.13: Various geometrically shaped 16QAM constellations [93]

by >2 dB by optimally choosing ring radii based on transmission distances, Fig. 2.13. However, all these geometric shaping schemes are specific to the link and require extensive characterization of the link to achieve optimal performance. Recently there has been some investigations in joint geometric and probabilistic shaping for optical communication systems [94]. However, this research is still in its infancy.

2.4.2 Matched Filtering

A matched filter is the complex conjugate of the spectrum of the received signal that results in the filtered signal achieving maximum SNR [88]. It is commonly applied in the frequency domain. Matched filtering can suffer in the presence of frequency offsets. However, in coherent optical links the frequency offset is typically less than 2 GHz and its impact on matched filtering is minimal.

2.4.3 Chromatic Dispersion Compensation

Chromatic dispersion compensation is an important step in the receiver DSP module. It compensates for the accumulated dispersion from the transport fiber. CD can be compensated in the time domain or the frequency domain. In the time domain, the filter coefficients are given by [95]

$$a_k = \sqrt{\frac{jcT^2}{Dz\lambda^2}} \exp\left(- j\frac{\pi cT^2}{Dz\lambda^2}k \right) \tag{2.50}$$

where $j = \sqrt{-1}$, T is the symbol period, D is the dispersion parameter, z is the transport distance and λ is the operating wavelength. The required number of taps ($-N \leq k \leq N$) is determined by the accumulated CD and is given by

$$N = \left\lfloor \frac{|D| z \lambda^2}{2cT^2} \right\rfloor \tag{2.51}$$

where $\lfloor \cdot \rfloor$ is the floor operator.

When compensating for large amounts of CD, it is preferred to compensate for dispersion in the frequency domain using an all pass filter described by [96]

$$G(\omega) = \exp\left(- j \frac{Dz\lambda^2}{4\pi c} \omega^2 \right) \tag{2.52}$$

Overlap-and-save technique is used to implement this filter [96].

2.4.4 Timing Recovery

Timing recovery is a necessary operation in digital communication to obtain best samples from the received signal. Digital filter and square timing recovery is a common timing recovery algorithm used in optical communication systems [97]. In this technique, the signal is first filtered and sampled at integer multiple of the symbol rate. Then the square magnitude of the signal is obtained

$$x_k = \left| \sum_n a_n g\left(\frac{kT}{N} - nT - \epsilon T \right) + \tilde{n}\left(\frac{kT}{N} \right) \right|^2 \tag{2.53}$$

where a_n is the transmitted symbol, $g(t)$ is the convolution of the transmitter pulse shape and the receive filter, T is the symbol period, ϵ is an unknown timing error, N is the integer oversampling factor and $\tilde{n}(t)$ is the received noise. Calculating the phase of the spectral

component of Eqn. 2.53

$$\hat{\epsilon}_m = -\frac{1}{2\pi}\arg\left(\sum_{k=mLN}^{(m+1)LN-1} x_k e^{-j2\pi k/N}\right) \tag{2.54}$$

yields us a timing estimate for a block of L symbols. The oversampling rate needs to be >2 since the phase needs to be extracted at symbol rate. The value of L determines the trade-off between the validity of the estimate for the entire block and the effect of noise on the estimate.

2.4.5 Polarization Demultiplexing

The two polarizations of an optical signal mix as they propagate through the fiber and need to be separated to extract the message symbols from each polarization effectively. This process can be viewed as a multiple-input multiple-output (MIMO) problem [88] and can be separated using source separation algorithms. The most common method used in optical communication systems is the multi-modulus algorithm (MMA) [98]. The output of these algorithms are given by

$$x_{out}(k) = \mathbf{h}_{xx}^T \cdot \mathbf{x}_{in} + \mathbf{h}_{xy}^T \cdot \mathbf{y}_{in} \tag{2.55}$$

$$y_{out}(k) = \mathbf{h}_{yx}^T \cdot \mathbf{x}_{in} + \mathbf{h}_{yy}^T \cdot \mathbf{y}_{in} \tag{2.56}$$

where $\mathbf{x}_{in}$ and $\mathbf{y}_{in}$ are the received polarizations, $\cdot^T$ is the transpose operator and the filter $\mathbf{h}$ updates as

$$\mathbf{h}_{xx} \rightarrow \mathbf{h}_{xx} + \mu(r^2 - |x_{out}|^2)x_{out}\mathbf{x}_{in}^* \tag{2.57}$$

$$\mathbf{h}_{xy} \rightarrow \mathbf{h}_{xy} + \mu(r^2 - |x_{out}|^2)x_{out}\mathbf{y}_{in}^* \tag{2.58}$$

$$\mathbf{h}_{yx} \rightarrow \mathbf{h}_{yx} + \mu(r^2 - |y_{out}|^2)y_{out}\mathbf{x}_{in}^* \tag{2.59}$$

$$\mathbf{h}_{yy} \rightarrow \mathbf{h}_{yy} + \mu(r^2 - |y_{out}|^2)y_{out}\mathbf{y}_{in}^* \tag{2.60}$$

where μ is the step size and bold-face represents vectors. r^2 varies with the modulation format and is given by $r^2 = \mathcal{E}(a^4)/\mathcal{E}(a^2)$, where a are the symbols of the modulation formats being used and $\mathcal{E}$ is the expectation. If the modulation format employed is QPSK/4-QAM, $r^2 = 1$ and the algorithm is called constant modulus algorithm (CMA) [99]

A major limitation of the MMA algorithm is that the output can converge to the same solution for both signals. Many modifications have been proposed to the MMA algorithm to mitigate this drawback which involves constraining the X and Y filters to be orthogonal to each other [100, 101]. However, the two signals may not always be on orthogonal polarizations due to imperfection in optical components.

Blind source separation (BSS) based polarization demultiplexing algorithms have also been demonstrated in optical communication systems [102]. Their primary benefits include avoiding the singularity issue and better performance for higher order modulation formats. Additionally, BSS algorithms don't require signals to be on orthogonal channels. Independent component analysis (ICA), a type of BSS algorithm, has been demonstrated to achieve similar performance to CMA for QPSK [103] in optical communication systems without any convergence to a singularity. The method was easily extended to different modulation formats by changing the matching distribution. Its computational complexity is comparable to CMA requiring two phase extraction and eight more multiplications, and the algorithm converges faster than CMA [104]. The ICA update equations are given by

$$B_{k+1} = N_k B_k \tag{2.61}$$

$$N_{1,1} = 1 + \mu(1 - |x_{out}|^2) \tag{2.62}$$

$$N_{1,2} = \frac{\mu|a|}{2\sigma^2}(e^{j\phi_1} y^*_{out} - e^{-j\phi_2} x_{out}) - \mu x_{out} y^*_{out} \tag{2.63}$$

$$N_{2,1} = \frac{\mu|a|}{2\sigma^2}(e^{j\phi_2} x^*_{out} - e^{-j\phi_1} y^*_{out}) - \mu x^*_{out} y_{out} \tag{2.64}$$

$$N_{2,2} = 1 + \mu(1 - |y_{out}|^2) \tag{2.65}$$

where B_k is a 2x2 inversion matrix, and a and σ are constants describing the matching

normal distribution.

2.4.6 Frequency Offset Correction

After polarization demultiplexing, the frequency offset between the transmitter laser and the local oscillator laser is eliminated by estimating the frequency difference and then digitally removing it using complex phase multiplications. The frequency offset is estimated by finding the peak in the fourier transform of the fourth power of the optical signal [105].

2.4.7 Carrier Phase Recovery

Carrier phase recovery (CPR) algorithms compensate for random phase fluctuation arising from the realities of an optical laser. Both the transmitter laser and the local oscillator contribute to these fluctuations. An adaptive single-tap decision directed phase recovery algorithm is generally employed in optical communication systems to compensate for distortions introduced by carrier phase. The filter updates are given by [106]

$$w_i = w_{i-1} + \mu x_i (d_i - w_{i-1} x_i) \tag{2.66}$$

where d_i is the closest constellation point to $w_{i-1}x_i$. d_i is also known as the decision. Decision errors can result in large phase updates and it is usually recommended to not apply phase corrections to individual symbols if the applied phase offset results in a different decision output.

2.4.8 Channel Equalization

At the last stage of demodulation, an adaptive equalizer is employed in optical communication systems to compensate for any residual impairments that were not compensated by earlier demodulation algorithms. The most common algorithm employed at this stage is the decision directed complex least mean square (LMS) algorithm [107]. The output of the

LMS filter at instance k is given by

$$y_k = \mathbf{w}_k^T \mathbf{x}_k \tag{2.67}$$

where bold-face represents vectors and the filter weights $\mathbf{w}$ update according to

$$\mathbf{w}_{k+1} = \mathbf{w}_k + 2\mu(d_k - y_k)\mathbf{x}_k^* \tag{2.68}$$

2.4.9 Miscellaneous

Optical receivers deployed in long haul optical links also include methods to compensate for nonlinear fiber impairments such digital backpropagation (DBP) [108], volterra equalizers [109], maximum a priori (MAP) detection [110], etc. These techniques have high computational complexities and are usually justified only for long haul links. Additionally, optical receivers also employ FEC codes of various types to achieve maximum capacity in the optical channel. We will not be discussing these technologies here. Interested reader can find more information in [87, 111].

2.5 Transmitter and Dispersion Eye Closure Quaternary

With the exponential growth of fiber optic communication systems in the modern era, there have been significant efforts to standardize methodologies and definitions that describe the working of an optical communication system. Fiber-optic network deployers typically assume that the transmitter, channel and receiver are produced by different vendors. Therefore, in order to ensure interoperability, the main components in a link are individually specified such that even in the worst-case scenario, the system achieves the required BER threshold. One such specification used to qualify PAM-4 optical transmitters is called transmitter and dispersion eye closure quaternary or TDECQ [112].

TDECQ employs an iterative process to qualify optical transmitters, Fig. 2.14. First,

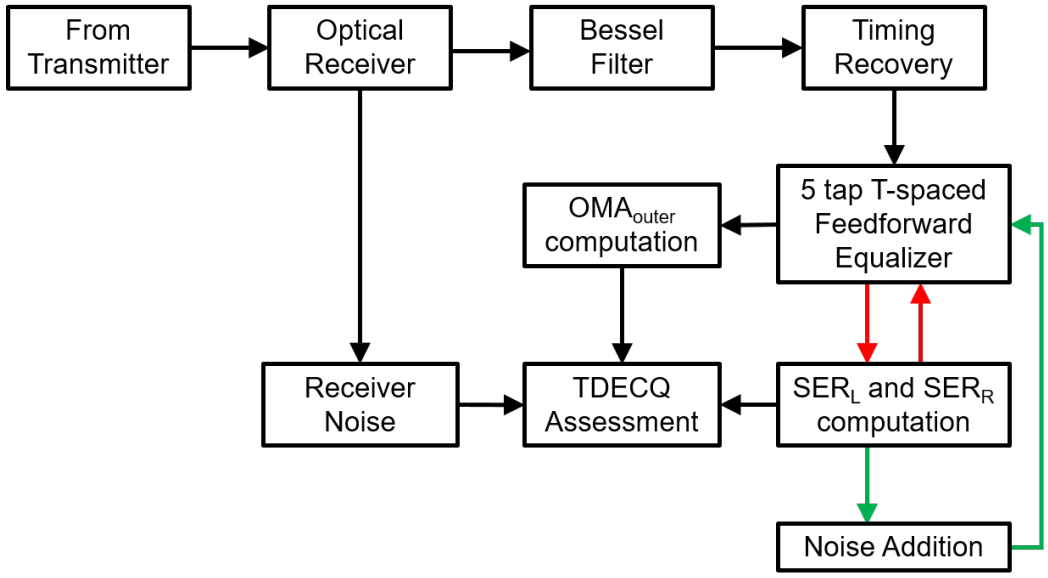

Figure 2.14: Block diagram demonstrating how TDECQ penalty is assessed after receiving a signal from a PAM-4 transmitter. The optimization algorithm consists of two iterative processes. The first process (marked in red) computes the best FFE filters to minimize the SER for a given noise. The second process (marked in green) increases the noise variance to achieve the target SER of 4.8×10^{-4}

the noise of the optical receiver is measured in order to ensure that the characteristics of the receiver are backed out when assessing the performance of the transmitter. This noise is denoted by σ_s. Then, an SSPRQ pattern is loaded onto the transmitter and received by the optical receiver. SSPRQ stands for short stress pseudo-random quaternary [113]. The pattern is derived from a PRBS-31 pattern and is 65,535 symbols long.

After one full pattern is obtained at the receiver, the signal goes through a fourth order Bessel filter whose bandwidth is half the symbol rate. Timing recovery is performed on the filtered signal to resample the signal and obtain best samples. These samples are then passed through a 5-tap T-spaced feed forward equalizer (FFE) to obtain the best symbol error rate (SER) [88]. The sum of all equalizer weights needs to be 1 and the tap with the maximum weight should occur within the first three filter weights. Additionally, the tap with the maximum weight should be at least 0.8 in magnitude. By using a receiver equalizer in the measurement process, TDECQ attempts to create a more realistic performance metric since receiver filters are now commonplace in optical communication systems.

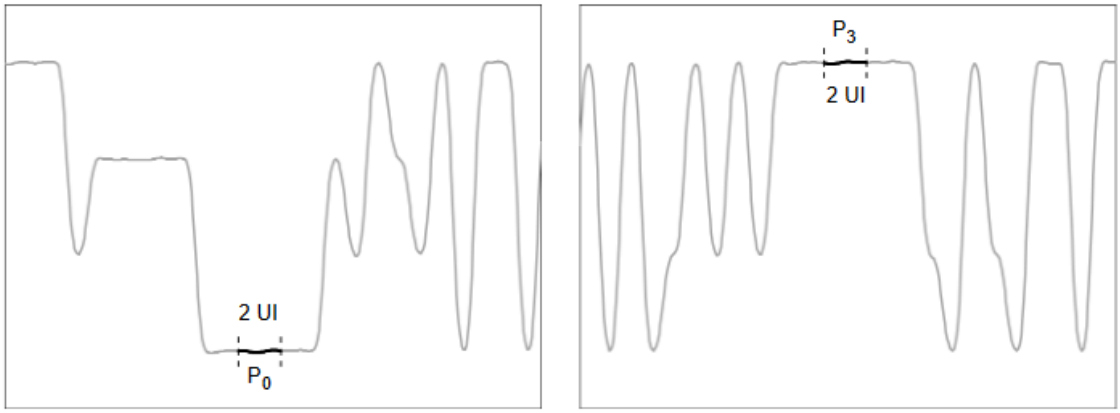

Figure 2.15: Parts of the SSPRQ pattern used to measure the OMA. P_0 and P_3 are the average amplitude levels of amplitude 0 and 3 [114]

The output of the equalizer is also used to calculate the signal's OMA (also known as $\text{OMA}_{\text{outer}}$) which will be used later to compute the TDECQ. In order to compute the OMA, 7 consecutive occurrences of 3s and 6 consecutive occurrences of 0s are identified in the captured pattern. Note that in a PAM-4 signal, the highest and lowest symbol levels are assigned values of 3 and 0, respectively. Unlike, coherent systems where 4 level formats have their amplitude levels denoted by ± 3 and ± 1, direct detect links denote them by 0, 1, 2, and 3, since it is not possible to obtain the phase of the signal through direct detection. OMA is a measure of the amplitude difference in the highest signal amplitude and the lowest signal amplitude. In the presence of noise and distortions, it is not possible to uniquely identify an OMA owing to variations in the amplitude levels from these effects. Therefore, for measuring TDECQ, the OMA is defined as the difference in the average amplitude levels of the two central symbols in these consecutive occurrences, Fig. 2.15.

After equalization, the signal is interpolated and an eye-diagram is created, Fig. 2.16. The eye diagram is centered using the average received optical power and the average eye crossing times, denoted by 0 and 1 in Fig. 2.16, are obtained. Two vertical histograms are then generated from the eye-diagram, which are centered around 0.45 unit interval (UI) and 0.55 UI. One UI denotes one symbol period. Each histogram window is 0.04 UI long. The vertical histograms are used to measure two SERs, SER_{L} and SER_{R}, one for each

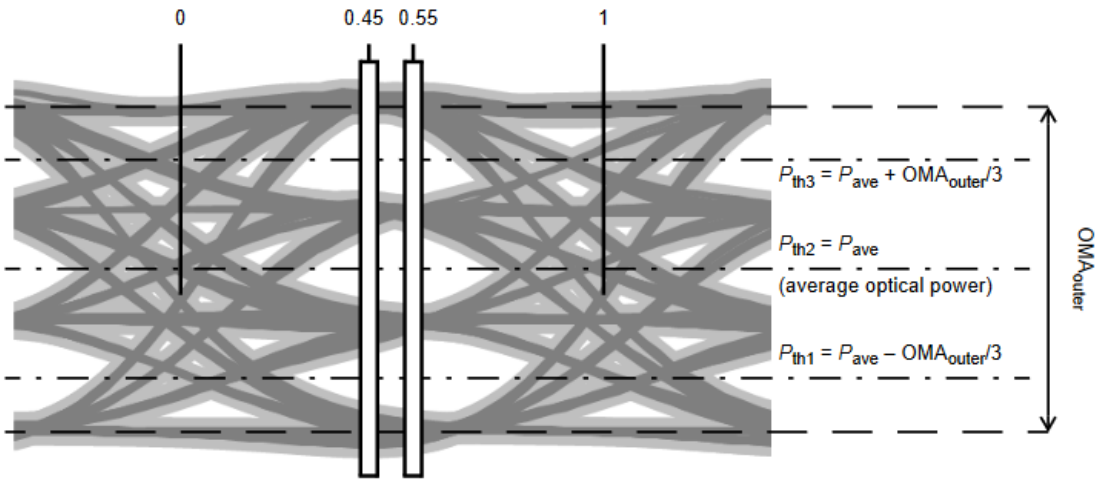

Figure 2.16: PAM-4 eye-diagram showing various components involved when creating eye-diagrams for measuring TDECQ. Thresholds for various symbols, left and right histogram and eye crossing times are shown [114]

histogram. The higher of the two SERs is determined as the SER of the transmitter. Then numerical noise of increasing variance is added to the system and the process of estimating the SER and changing the filter weights is continued till the transmitter SER is 4.8×10^{-4}. The variance of the added numerical noise used to obtain this SER is denoted as σ_G. Finally, the TDECQ is calculated using

$$\text{TDECQ} = 10 \log_{10} \left(\frac{OMA_{outer}}{6 Q_t R} \right) \tag{2.69}$$

where $R = \sqrt{\sigma_G^2 + \sigma_s^2}$ and $Q_t = 3.414$.

TDECQ is the difference in the variance of the amount of noise that needs to be added to an ideal PAM-4 signal and the received PAM-4 signal. For fair comparison, the virtual transmitter that outputs the ideal PAM-4 signal and the 'transmitter under test' need to have the same $\text{OMA}_{\text{outer}}$. Equation 2.69 is derived using this constraint [112]. Note that the ideal PAM-4 signal will always tolerate more noise than the received PAM-4 signal, and therefore, TDECQ will always be a positive number. It is measured in dB. Since TDECQ uses a virtual receiver, the golden receiver used for comparison is standardized and TDECQ

demonstrates higher repeatability.

By exhaustively searching for optimal filter coefficients in an iterative fashion, TDECQ provides us with a rigorous and accurate methodology for qualifying the performance of optical transmitters. However, this iterative approach is time consuming and severely slows down the manufacturing and testing process.

2.6 Machine Learning

The field of ML dates back to the early 1940s when simple linear models motivated from a neuroscientific perspective were designed to take n inputs $x_1, x_2, \cdots, x_n$ and associate them with an output y. These models would use weights $w_1, w_2, \cdots, w_n$ and compute their output $f(x, w) = \sum_{i=1}^{n} w_i x_i$. In fact, in 1943, the McCulloch-Pitts neuron was an early neuron model that could differentiate between two categories of inputs based on whether $f(x, w)$ was positive or negative [115]. However, the weights w had to be set by a human operator. In the 1950s, the perceptron became the first model that could learn the weights on its own based on examples of input-output pairs. Around the same time, adaptive linear element (ADALINE), was also demonstrated to predict real numbers from data [116]. Perceptron and ADALINE were linear models and could not learn popular nonlinear functions such as the XOR. This limitation rendered these techniques unpopular and temporarily diminished the interest in neural networks (NN)/ML [117].

Interest in ML revived in the 1980s due to a movement called connectionism or parallel distributed processing [118]. Connectionism started in the field of cognitive science where researchers were trying to understand the working of the human brain by combining multiple different levels of analysis. Connectionism attempts to achieve intelligent behavior by connecting a large number of simple computational units. In modern ML, it forms the basis of hidden units. Backpropagation, a commonly used technique to train NNs, was also successfully demonstrated around the same time along with many other advances in ML [119]. However, the computational costs associated with these algorithms severely hindered the

growth of ML in the 20th century.

In 2006, Geoffrey Hinton demonstrated an efficient method to train an NN called the deep belief network using a strategy known as the greedy layer-wise pretraining [120]. Soon after, the Canadian Institute for Advanced Research (CIFAR) demonstrated that the technique could be generalized for any type of NN and systematically improved the generalization on test examples [121]. This training method, along with the advent of fast central processing units (CPUs) and general-purpose graphic processing units (GPU), and availability of large data sets (the age of Big Data) revolutionized the field of ML making it a practical tool for various applications. In recent years, ML has impacted many fields including speech recognition, image processing, autonomous vehicles etc.

2.6.1 Machine Learning Basics

Definition

An ML algorithm attempts to create a model to perform a certain task by using examples (also known as the training data) that follows the relations of the task [6]. The formal definition of ML was coined by Tom Mitchell in 1997 [122] and is described as "A computer program is said to learn from experience E with respect to some class of tasks T and performance measure P, if its performance at tasks in T, as measured by P, improves with experience E". A task T can be classification, regression, anomaly detection etc. The performance P can be the classification or regression accuracy. The experience E is the information gained by the algorithm as it traverses through the training data.

Types of machine learning methods

ML methods are often divided into three categories - supervised learning, unsupervised learning and reinforcement learning. In supervised learning, the objective is to find a predictive mapping from an input to an output using a set of labeled input-output pairs. These labels can be categorical or real-valued scalars for classification and regression, respec-

tively. It is the most widely used ML category. In unsupervised learning, the task is to identify a meaningful structure in a given set of data. By definition, the data has only one label or it can be said that there are no labels. Unsupervised learning is mainly used for data visualization, exploratory data analysis, anomaly detection and feature learning. In some cases, unsupervised learning methods can be used in a supervised learning framework to supply transformed versions of the input for improved supervised learning performance. Reinforcement learning is the process of learning, through trial and error, how to interact in a dynamic environment to achieve the most reward [123]. Here, we primarily focus on supervised and unsupervised learning algorithms.

Generalization

The basic requirement of an ML algorithm is to perform well on both observed and unobserved data. The ability of a model to predict unobserved data well is known as generalization. In order to understand generalization, we must first understand complexity and capacity. Complexity is used to denote the sophistication between the input and the output, while capacity is defined as the ability of a model to approximate data relationships well. In general, these concepts are not strictly defined but there have been significant efforts to do so mathematically. One such example is the Vapnik-Chervonenkis (VC) dimensions that attempt to quantify the model complexity for binary classifiers [124]. Qualitatively, the data complexity can be interpreted as the number of dimensions over which useful relationships can be found between the input and the output.

For an ML algorithm to generalize well, the complexity and the capacity need to be similar. If the capacity is greater than the complexity, the model will overfit and learn patterns in the noise or idiosyncrasies of the training data, Fig. 2.17. If the complexity is greater than the capacity, the model will underfit and not learn the underlying relationships between the input and the output. Underfitting results in high training error and can be easily rectified during the training process. Overfitting, however, results in high training

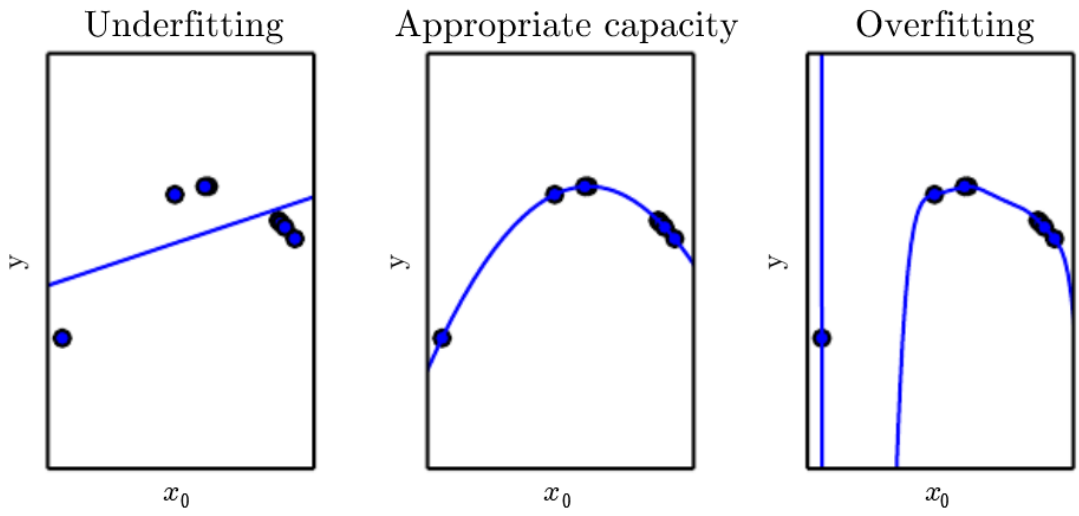

Figure 2.17: Samples generated from a quadratic function fit using ML models of varying capacity. (left) underfitting, (center) appropriate capacity, and (right) overfitting [6]

accuracy and cannot be detected during the training process. Therefore, a second set of data, known as the test data, is usually employed to ensure there is no overfitting. Testing data is never used by the algorithm in its learning process and testing error is usually representative of the model's ability to generalize. A good ML model will have the least training error and the least difference between the training error and the testing error, Fig. 2.18. The difference between the training and testing error is known as the generalization gap. A common practice is to split the data 80%-20% for training and testing, respectively.

Regularization

In general, the complexity of the training data may not be known to us. Therefore, we would like to use the highest capacity possible when developing the model. However, this makes the model prone to overfitting. In order to prevent overfitting, a penalty is usually added to the cost function that scales the capacity of the model if and only if there is positive gain in the accuracy of the model. This process is known as regularization. Formally, regularization is any modification we make to the learning algorithm that is intended to reduce the generalization error but not its training error [6].

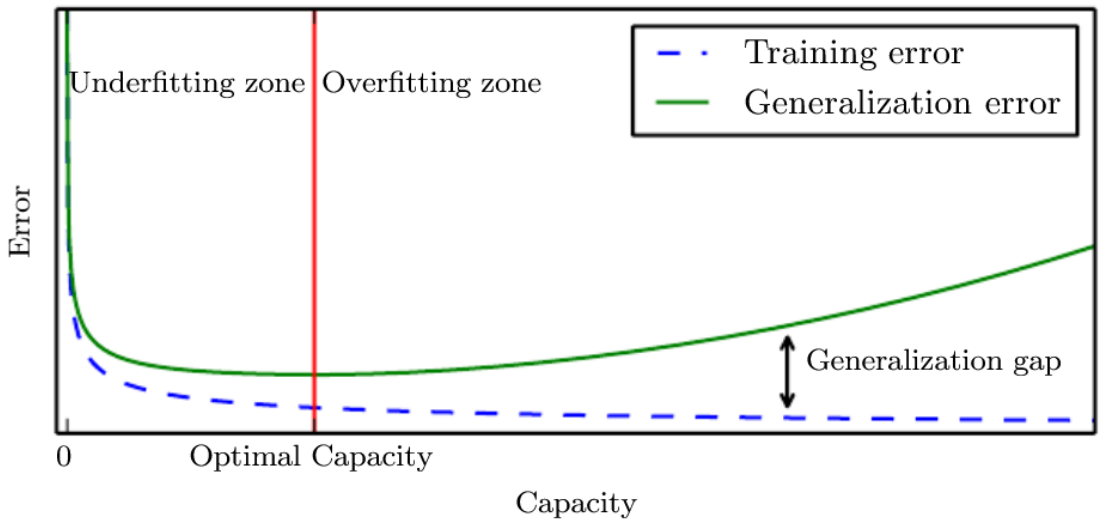

Figure 2.18: Typical relationship between error and capacity. Testing error is representative of generalization error. Underfitting and overfitting regimes are shown to the left and right of optimal capacity [6]

Hyperparameters and Validation Set

Most ML algorithms have hyperparameters associated with them. They are parameters that control the algorithm's behavior and are not learned by the algorithm. In some cases, a parameter becomes a hyperparameter because the underlying optimization required to learn the parameter is complex and computationally expensive. However, in most cases, a parameter is chosen to be a hyperparameter because it controls the model complexity and learning the parameter will always result in overfitting. Regularization parameters are usually hyperparameters.

Training data cannot be used to choose the hyperparameters because training accuracy does not represent the model's ability to generalize. Testing data cannot be used for identifying hyperparameters since we need it to test the complete model which includes the hyperparameters. Therefore, a third set of data, known as validation data, is used for this process. Validation data is obtained by further splitting the training data, usually at 80%-20% with 80% for training and 20% for validating. By ensuring that the validation data is not used for training, it can be used to identify hyperparameters that avoid overfitting.

Cross Validation

Dividing the data set into training and testing sets can results in the testing set being small. A small set implies statistical uncertainties, making it difficult to obtain a good ML model. In order to avoid this, cross-validation is performed when generating an ML model. In a k-cross validation, the data is divided into k non-overlapping sets of approximately the same size. For every trial i, the i^{th} subset is used for testing and the remaining data is used for training. After all training trials, the testing error is calculated as the average of all testing errors across all trials.

Bias-Variance Trade-off

Since the training data used to create an ML model has an associated statistics, the model itself will have an associated statistics. Therefore, foundational concepts of point estimation (bias and variance from the field of statistics) can be used to describe certain characteristics of an ML model. These characteristics include underfitting and overfitting.

Point estimation is the attempt to give the single best prediction of some quantity of interest from available data points [6]. A point estimate is a function of the data itself and is given by

$$\hat{\theta}_n = g(x_1, x_2, \cdots, x_n) \tag{2.70}$$

where $\hat{\theta}_n$ is the point estimate and $x_1, x_2, \cdots, x_n$ are the data points. One can define the bias of an estimator as

$$\text{bias}(\hat{\theta}_n) = \mathcal{E}(\hat{\theta}_n) - \theta \tag{2.71}$$

where θ is a quantity of interest. If the bias is 0, the estimator is said to be unbiased. If $\lim_{n\to\infty} \text{bias}(\hat{\theta}_n) = 0$, the estimator is said to be asymptotically unbiased.

Another property of an estimator is its variance, which is given by

$$\text{Var}(\hat{\theta}) \tag{2.72}$$

where the random variable is the training set itself and 'Var' is the variance. The variance of an estimator is a measure of how we would expect the estimate $\hat{\theta}_n$ to change as the data $x_1, x_2, \cdots, x_n$ changes.

Let us assume a function f that associates the observed output Y to an input X. Then,

$$Y = f(X) + e \tag{2.73}$$

where e is the measurement error that is independent of Y. Let us assume that $\hat{f}$ is the model that an ML algorithm learned for this input-output pair. Then the mean square error (MSE) for an observation can be given by

$$\begin{aligned}
\text{Error} &= \mathcal{E}\left[(Y - \hat{f}(X))^2\right] && (2.74)\\
&= \mathcal{E}\left[(f(X) + e - \hat{f}(X))^2\right] && (2.75)\\
&= \mathcal{E}\left[(f(X) - \hat{f}(X))^2\right] + \mathcal{E}(e^2) && (2.76)\\
&= \left(\mathcal{E}\left[\hat{f}(X)\right] - f(X)\right)^2 + \mathcal{E}\left(\left(\hat{f}(X) - \mathcal{E}\left[\hat{f}(X)\right]\right)^2\right) + \mathcal{E}(e^2) && (2.77)
\end{aligned}$$

where the expectation is taken over all training data X. The first term in Eqn. 2.77 is the bias of the ML model which is the difference in the expected prediction of the model and the correct value which it is trying to predict. The second term is the variability of the model for various training data. The third term is the irreducible error that rises from the measurement itself.

The bias and variance of an ML model is related to its capacity, Fig. 2.19. Increasing the capacity increases the variance error and decreases the bias error. Similarly, decreasing the capacity increases the bias error and decreases the variance error. Optimal capacity of

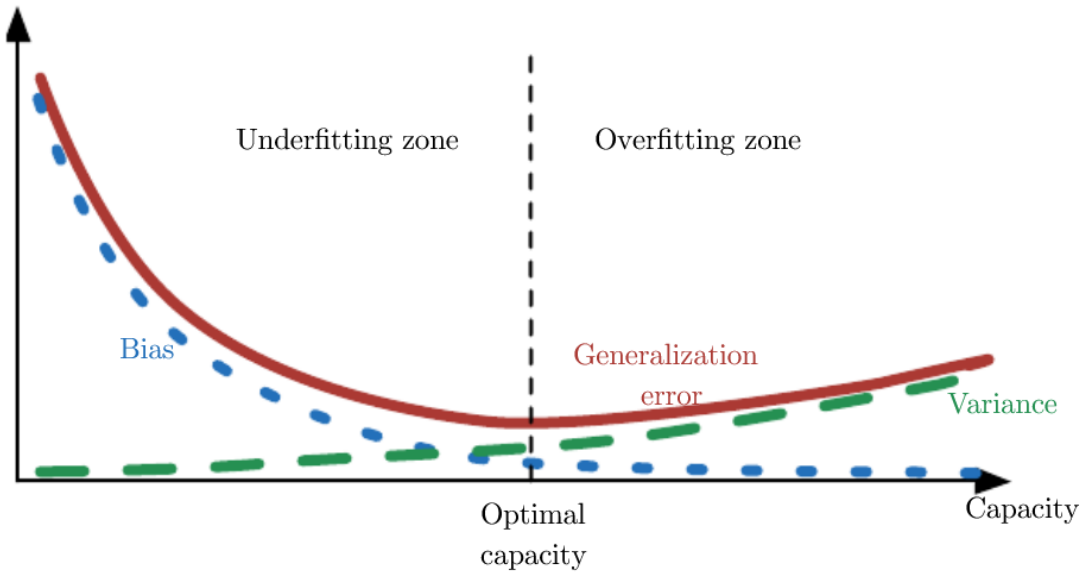

Figure 2.19: Relation between the capacity of an ML model and its bias and variance. Optimum capacity occurs when the total error, the sum of bias error and variance error, is the least [6]

an ML model is where the sum of these error (total error or generalization error) is the least.

2.6.2 Supervised Learning

Supervised learning techniques use labeled input-output data to create an ML model. The model can be used for classification or regression. Some common supervised learning techniques are described below.

Support Vector Machines

Support vector machines (SVM) are one of the most influential approaches in supervised learning that is widely used to separate two types of data [125]. It is driven by the linear function $y(x) = x^T w$, where y is the observed output, x is the input and w is the transformation we are trying to estimate. For simple linear regression, the minimum MSE (MMSE) estimate is given by $\hat{w} = X^T(XX^T)^{-1}y$, where $X = (x_1^T, x_2^T, \cdots, x_n^T)$ are the input observations and $y = (y_1, y_2, \cdots, y_n)^T$ are the corresponding output observations. For simple

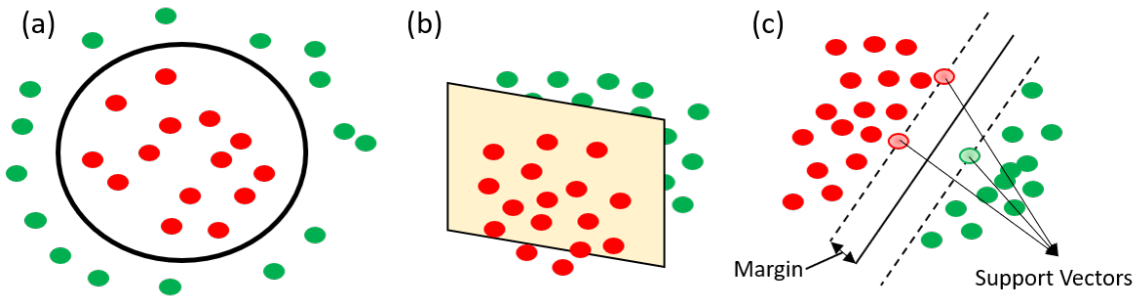

Figure 2.20: (a) Data from two classes that are not linearly separable. (b) Data transformed to a higher dimension using nonlinear transformation that can be separated using a hyperplane. (c) SVM showing classification between two types of data. Support vectors and margins are labeled

classification, one can use the sign of $y(x)$: $y(x) > 0$ for one class and $y(x) < 0$ for another class. Here, $y(x) = 0$ would define the hyperplane separating the two classes [126].

However, linear functions are insufficient to model complex relations as the function is linear in both w and x. Therefore, to enhance the flexibility of the model, linear combinations of nonlinear functions of the input are used. These are given by $y = \sum_j w_j \phi_j(x)$, where $\phi_j(x)$ are the basis functions [126]. Using basis functions, one can transform the data to a higher dimension (possibly infinite) where the data can be linearly regressed or linearly separated based on the application, Fig. 2.20(a)-(b). Note that the relationship is still linear in w and therefore the use basis functions does not change the solution methodology.

Calculating the basis functions, however, significantly increases the computational costs based on the number of dimension the transformation introduces. SVMs circumvent this issue using a clever technique known as the 'kernel trick' [126]. The trick consists of observing that many ML algorithms, including SVMs, can be written exclusively in terms of dot products between inputs. By replacing the dot products with kernel evaluations, one can achieve the required nonlinearities without transforming individual inputs separately. The most commonly used kernel evaluation is the Gaussian kernel given by

$$k(x_1, x_2) = \exp\left(\frac{(x_1 - x_2)^2}{2\sigma^2}\right) \tag{2.78}$$

where x_1 and x_2 are the two input samples and σ is a scaling parameter. The Gaussian kernel is also known as the radial basis function (RBF). RBF corresponds to a dot product in infinite dimensions [6].

A major drawback of kernel machines is that the cost of evaluating the decisions scales with the size of the training set. In order to mitigate this, SVMs use a small subset of training samples that lie close to separating hyperplane to make its decisions. This subset of training samples are known as the support vectors, Fig. 2.20(c). Additionally, the hyperplane is chosen such that there is maximum separation between the support vectors and the hyperplane. The separation is known as the margin, Fig. 2.20(c). SVMs also use slack variables to accommodate for outliers in the training samples. A parameter, box constraint, usually controls the trade-off between slack and performance in the optimization algorithm.

SVMs typically incur large computational costs with large training data set and struggle to generalize well when using generic kernels [127]. NNs have been demonstrated to overcome these limitations and outperform RBF based SVM, especially on the MNIST benchmark [120].

Feed Forward Neural Networks

The purpose of a feed forward NN is to approximate functions. They are also known as deep NN (DNN) or multi-layer perceptron (MLP). They are called feed forward NN because the information flows in one direction, from the input to the output through some intermediate calculations. NNs are called networks because they are composed of a series of functions associated by a directed graph, Fig. 2.21. Each set of functions is called a layer and the number of layers used in an NN is called the depth of the NN. The first layer in an NN is the input layer. This is followed by multiple hidden layers and the final layer is called the output layer. The term 'deep learning' refers to NNs with multiple hidden layers.

Each node in the hidden or output layer is a non-linear transformation of its input. The nonlinear transformations are also called activations. Common activation functions include

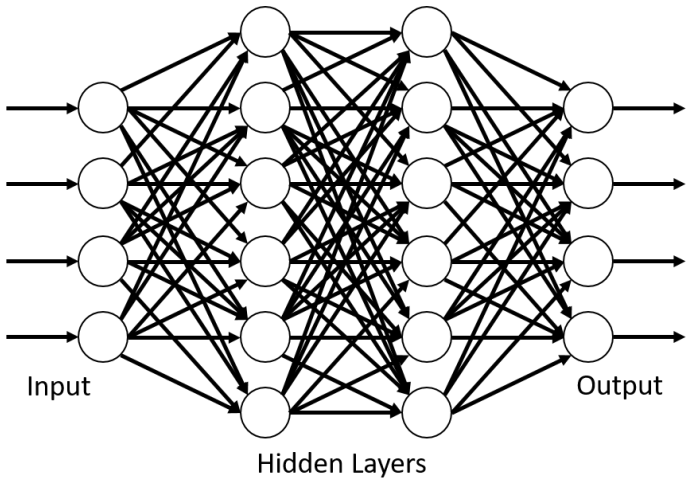

Figure 2.21: A feed forward NN with two hidden layers. Each node in the hidden or output layer performs a nonlinear transformation. They are also called activations. Inputs of every activation is a weighted multiplication of all the outputs of the previous layer

soft-max, sigmoid, rectified linear unit (ReLU) etc. [127]. These activations along with the network architecture makes NNs a well-performing arbitrary function approximator. NNs typically use cross-entropy loss function and back-propagation for optimizing the weights and biases of the network [6]. Popular training algorithms include the stochastic gradient descent and adaptive moment (Adam) estimation.

Many techniques are commonly employed in NNs to improve its generalization error. These include $\mathcal{L}^1$ or $\mathcal{L}^2$ regularization to limit the size of the model parameters, 'data augmentation' where artificially data is created for training purposes, 'early stopping' where training is prematurely stopped when the generalization gap during training diverges, and 'dropouts' where certain nodes in the NN are randomly removed during training.

An aspect of all ML algorithms that separate it from other optimization algorithms is that the objective function usually decomposes as a sum over the training samples. If the training data set is large, this summation can be computationally expensive. In order to avoid this, NNs usually divide the training set into smaller segments and calculate the gradient over all segments individually. Each segment is called a minibatch. The size of the minibatch optimizes the trade-off between computational complexity and statistical

significance. Typical minibatch sizes range from 32 to 256.

NNs are extensively used for binary and multi-class classification and regression.

Convolutional Neural Networks

Convolutional neural networks (CNN) are a special kind of NN that specialize in processing data with grid-like topology [128]. These include one-dimensional data such as time-series signals or two-dimensional data such as images. They are widely used in image classification, medical image analysis and natural language processing.

A CNN consists of an input layer, one or many feature extraction layers (FEL), one or many hidden layers, and an output layer. FELs attempt to enhances features and reduce input size so that the hidden layers are computationally feasible, Fig. 2.22. Each FEL consists of a convolutional layer, a nonlinear transformation and a pooling layer. A convolutional layer convolves the input with multiple kernels (analogous to filters in DSP) to enhance various features in the input. For an image, such features can include edges, shapes, contours etc. The kernel sizes are typically chosen to be smaller than the image size to identify local features. They can also be associated with a certain stride to space the convolutions. The output of the convolutional layer is then passed through a nonlinear transformation to detect these enhanced features. A commonly used transformation is the ReLU. Finally, the pooling layer attempts to summarize the detected features. Common pooling techniques include max-pooling which chooses the maximum value within a small window, and average-pooling which averages all the values in that window. Pooling layers are also associated with strides that reduce the input size.

The output of a FEL can be passed to another FEL to further enhance features or to fully connected hidden layers, Fig. 2.21, to process these features and generate meaningful outputs. The number of convolutional kernels (or filters), the size of the convolutional kernels and the pooling windows, and the strides of the convolutional layers and pooling layers are all hyperparameters that are chosen by the user heuristically.

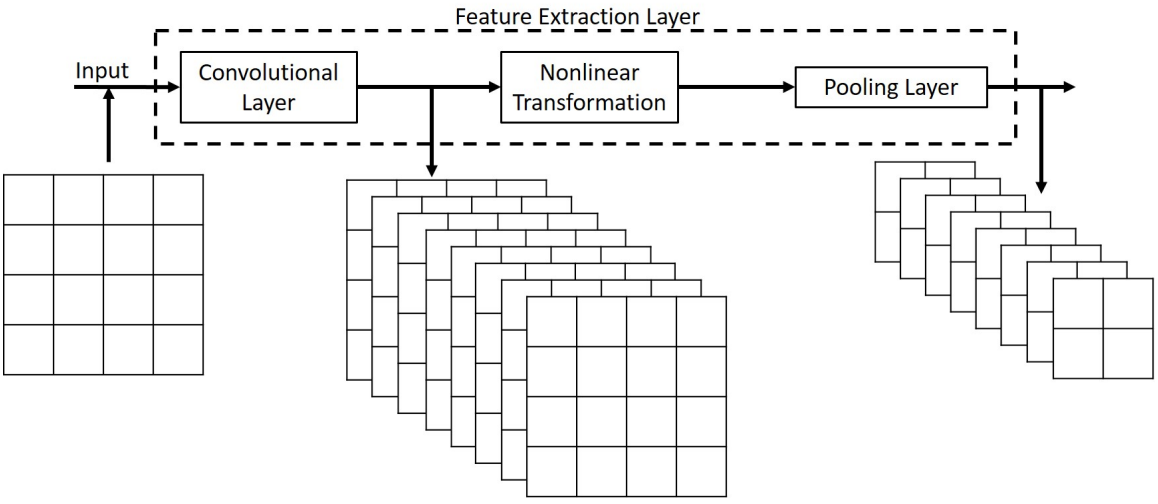

Figure 2.22: Transformation of input data as it passes through various stages of an FEL in a CNN. The input can have any number of dimensions. In this example, it has two dimensions like a grayscale image. The convolutional layer convolves the input with various kernels (or filters) to produce multiple outputs of the same dimensions as its input. The nonlinear transformation does not change the size of its input. The pooling layer reduces the size of its input depending on the employed stride. If the number of kernels in the convolutional layer and the stride of the pooling layer are properly chosen, the total size of the output will be smaller than the input. Additionally, the output will consist of enhanced features from the input

Long Short Term Memory

Traditional feed forward NNs do not have internal memory and therefore produce limited performance when modeling systems with temporal features. Recurrent neural networks (RNNs) are a special type of NN that loop back their previous outputs and use it along with their new inputs to generate their new outputs [129]. While they perform better than traditional NNs due to their architecture, training RNNs can be challenging due to the vanishing or blowing up gradient problem during the backpropagation through time process [130]. Such limitations render RNNs incapable of modeling long term temporal relations.

Long short term memory (LSTM) was created to better model long term temporal relations in NNs [131]. They employ LSTM cells, Fig. 2.23, that consists of three 'gates' and two 'states' in order to control the temporal flow of information. The first gate is the forget gate. It decides what old information is still relevant and updates the cell state appropriately. The second gate is the input gate. It determines what information in the current input is relevant and updates the cell state accordingly. The final gate, the output gate, takes the current cell state, the previous hidden state and the input to generate the current hidden state and the current output. LSTMs are widely used in speech and handwriting recognition.

2.6.3 Unsupervised Learning

Unlike supervised learning, unsupervised learning algorithms do not employ data with distinct labels. They are typically used for anomaly detection, feature learning and dimensionality reduction. Some common unsupervised learning algorithms are described below.

One-Class Support Vector Machines

One-class SVM is a special type of SVM that is commonly used to identify structure within data [132]. Unlike a two-class SVM that creates a hyperplane that separates the two types of data, one-class SVM attempts to create the smallest hypersphere that contains all the training data, Fig. 2.24. Features of two-class SVM such as support vectors and slack

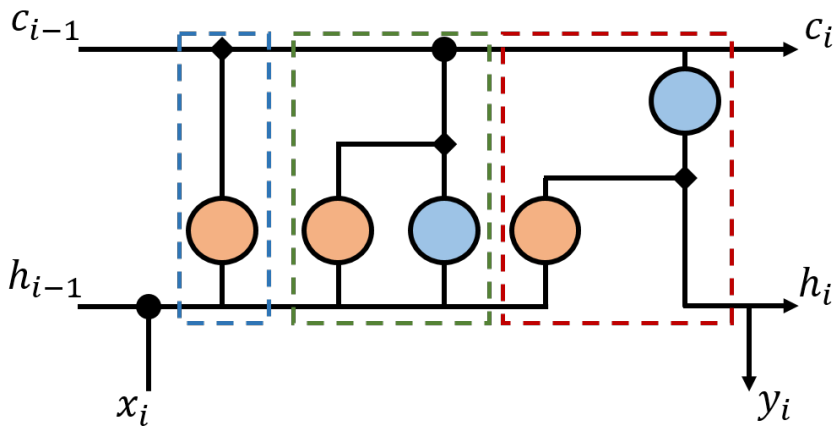

Figure 2.23: An LSTM cell. c_i is the cell state and h_i is the hidden state. Circle intersections represent addition and diamond intersection represent multiplication. Orange circles are sigmoid nonlinearity and blue circles are hyperbolic tangent nonlinearity. The forget gate, input gate and output gate are marked in blue, green and red dashed boxes, respectively. The input to the cell, x_i, is added with the previous hidden state, h_{i-1}, and passed to the forget gate, the input gate and the output gate. The previous cell state, c_{i-1}, is updated by the forget gate and the input gate with relevant old information and new current information, respectively. The updated cell state, c_i, along with the previous hidden state, h_{i-1}, and the current input, x_i, is used to generate the new hidden state, h_i, and the output, y_i

variables are also common to one-class SVM. The slack parameter ν (equivalent to the box constraint in two-class SVM), is used to optimize the trade-off between overfitting and generalization and defines the maximum fraction of the training data that can be potentially considered as outliers during the training process.

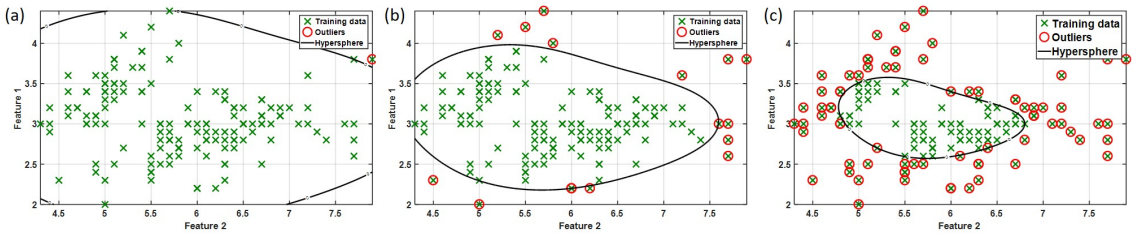

Figure 2.24: One-class SVM trained with ν = (a) 0.01, (b) 0.1 and (c) 0.5. As ν increases, the size of the hypersphere decreases such that it contains at least (1-ν) fraction of training data points. ν controls the trade-off between overfitting and generalization

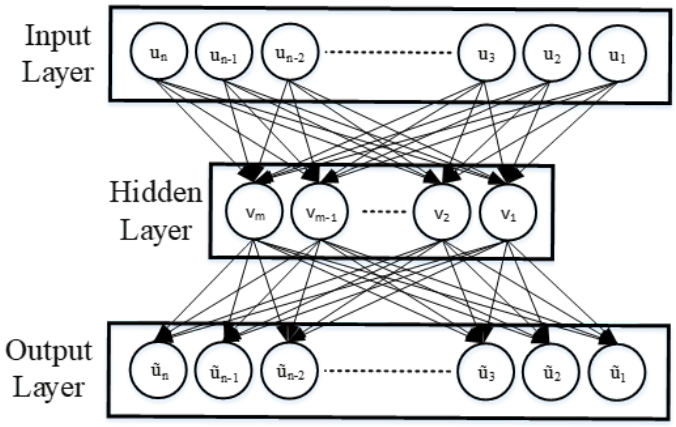

Figure 2.25: A simple autoencoder with one hidden layer. The autoencoder if said to be overcomplete if $m > n$ and undercomplete if $m < n$

Autoencoders

Autoencoders are a special type of NNs in which the desired output of the network is the input itself [133]. They are widely used for dimensionality reduction and feature learning. They can be viewed as nonlinear generalization of principal component analysis (PCA), a technique that converts a set of observations into linearly uncorrelated variables called principal components [134].

An autoencoder typically consists of an input layer, a hidden layer and an output layer, Fig. 2.25. The first half of the autoencoder is called the encoder and the second half is called the decoder. The output of the hidden layer is called the code and the size of the hidden layer is called the code size. Code size is typically chosen by the user. If the code size is greater than the input, the autoencoder is said to be overcomplete and the codes exhibit redundancies which can be used to identify shift invariant features. We will not discuss overcomplete autoencoders here. If the code size is smaller than the input, the encoder compresses the input by extracting useful features from the data that largely represents the data. These codes can be used for anomaly detection.

CHAPTER 3
FREQUENCY DEPENDENT ENOB REQUIREMENTS FOR HIGH SPEED OPTICAL LINKS

Electronic converters have become essential elements of most modern optical communication systems, both coherent and direct detect. Their advent has allowed for the use of sophisticated DSP techniques to achieve high data rates and spectral efficiencies. Electronic converters have also enabled elastic networks, where transmitters and receivers are equipped with adaptive algorithms, adding flexibility to the network and ensuring that the network is optimally utilized [135]. Link capacities continue to approach the Shannon limit using higher order modulation formats with advanced DSP [136, 137]. However, the current tendency to achieve faster data rates through a combination of higher symbol rates and higher modulation formats may not be sustainable with the growth in the performance of electronics, and ECs may introduce significant implementation penalties in such optical links [138].

There has been some preliminary research in understanding the effects of ECs on optical communication systems. Experimental investigation on the effects of ADCs on 1 GBaud optical signals employing 16QAM, 64QAM and 256QAM demonstrated that these formats require an ENoB of 3.8, 4.9 and 6.9 bits respectively to incur $<$2 dB OSNR penalties [139]. However, such data rates were too slow to be deployed in an optical system making the study not comprehensive. The effects of DACs on systems employing pre-emphasis filters were investigated in [140]. However, the study assumed all impairments arising from the DAC to be frequency independent grossly underestimating its effects on optical signals.

The use of a frequency dependent ENoB in link analysis is hindered by the availability of computationally efficient models that can be incorporated in optical simulation environments. In this chapter, we develop novel and computationally efficient DAC and ADC

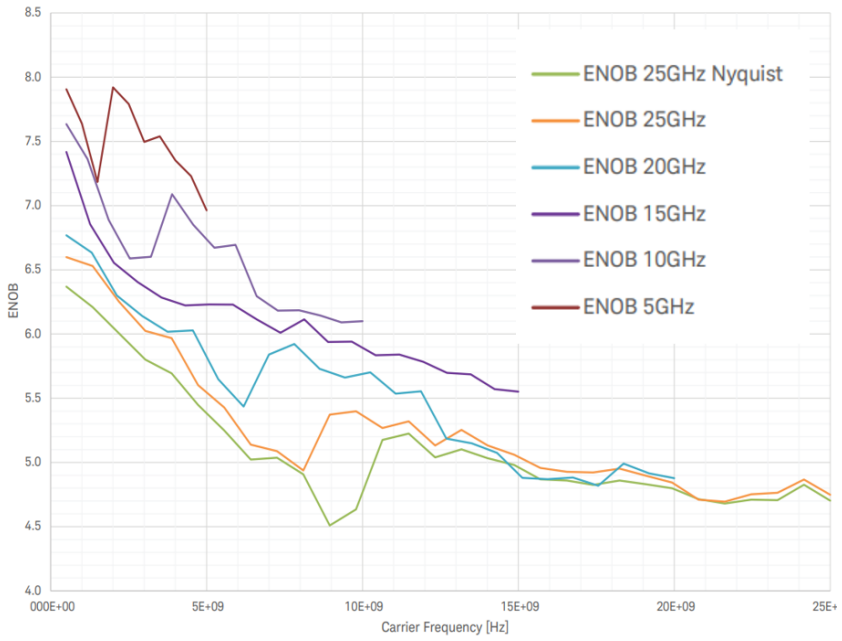

Figure 3.1: "Nominal ENOB measured on a differential signal combined by a 50 GHz Balun Hyperlabs HL9405 with a sample rate of 64 GSa/s, internal clock and 500 mV amplitude at different bandwidths." [141]

models that accurately simulate real ECs that are deployed in optical communication systems. We then use these models to estimate the associated implementation penalties when employing high baud rates and higher modulation formats.

3.1 Theory

Ideally, an EC employing an N bit hardware architecture will have a resolution of 2^N uniform levels. However, all ECs introduce noise and distortion to the signal reducing the amplitude resolution of the conversion (from analog to digital or vice versa). This effective resolution is known as the ENoB. For example, a modern DAC with sampling rates $>$64 GSa/s typical exhibits an average ENoB of 5 bits over all operational frequencies even though its hardware architecture is 8 bits.

The relation between ENoB and SINAD was described in Eqn. 2.43. However, this common result cannot be used in understanding the effects of ECs in optical communication systems as fiber links employ wideband devices and ENoB in such devices tend to ex-

hibit a frequency dependent behavior, Fig. 3.1 [141]. In order to understand this frequency dependence, we identified four major impairments that contribute to ENoB degradation in ECs. They are

1. Noise - Resulting from circuit thermal noise and modeled as additive white gaussian noise (AWGN).

2. Quantization - Resulting from the finite resolution levels of the EC. If the signal being converted is essentially random and the resolution levels are uniformly spaced, the effects of quantization can be assumed to be white and uniformly distributed. It is popularly known as ”quantization noise” for this reason. Real ECs, however, exhibit non-uniform resolution levels that give rise to differential nonlinearity (DNL) and integral nonlinearity (INL) [142]. The difference between two consecutive resolution levels (also known as the step width) for an ideal EC is 1 least significant bit (LSB). A DNL error is the difference between the actual step width and the ideal step width. It is defined for every bit transition. The INL error of a resolution level is the sum of all the DNL error up to that resolution level. Note that it is possible to have zero INL error at a resolution level for non-zero DNL errors. DNL errors are assumed to be white and uniformly distributed [143]. Typically, EC vendors specify the maximum DNL and INL for their products.

3. Timing/sampling jitter - Every EC has a built-in clock that is used to convert the signal from the analog/digital domain to digital/analog domain. The precise sampling instant varies due to imperfections of the clock, its distribution and all circuitry associated with handling the input analog signal, the clock and its various phases, and the process of sampling. These impairments give rise to timing jitter which adds distortions to the signal.

4. Bandwidth limitations - Resulting from the limited operational bandwidth of associated circuitry and packaging.

Noise and quantization are presumed frequency independent, while timing jitter and bandwidth are frequency dependent. By studying each of these impairments in a DAC, we developed Eqn. 3.1 to capture the frequency dependent ENoB exhibited by wideband DACs (See APPENDIX A for a detailed derivation). The expression is developed assuming that a sinusoidal waveform of frequency f is being converted and ENoB is evaluated using Eqn. 2.42 and Eqn. 2.43.

$$\begin{aligned} ENoB(f) =& ENoB_{DC} - \frac{1}{2}\log_2\left(1 + 6\left(2^{ENoB_{DC}}\pi f\sigma_{tj}\right)^2\right) \\ &+ \log_2|H(f)| - \frac{1}{2}\log_2\left[\frac{1}{f_B}\int_0^{f_B}|H(\nu)|^2 d\nu\right] \end{aligned} \tag{3.1}$$

Three metrics define $ENoB(f)$: $ENoB_{DC}$, the root mean square (RMS) timing jitter (σ_{tj}), and the net frequency response, $H(f)$. The measurement bandwidth, f_B [144], defines the frequency range over which the ENoB is measured. Depending on the chosen bandwidth, certain harmonics and noise may not be included when measuring the SINAD and this can increase the ENoB. It is typically set to half the sampling rate of the device. Figure 3.2 depicts $ENoB(f)$ for various $ENoB_{DC}$, Fig. 3.2(a), timing jitter, Fig. 3.2(b), and bandwidth, Fig. 3.2(c). When not varied, the fixed parameters are $ENoB_{DC}$ = 6, σ_{tj} = 600 fs, f_B = 32 GHz and $H(f)$ modeled as a fifth order Gaussian filter with bandwidth = 20 GHz.

$ENoB_{DC}$ represents the hardware bit architecture reduced by the effects of circuit thermal noise, DNL and INL. Since all these distortions add white noise and are frequency independent, their effects can be combined into an effective parameter. The effects of noise is typically $>$1 LSB and the effects of DNL and INL are typically $<$0.5 LSB [74].

The second term on the RHS of Eqn. 3.1 describes the impact of timing jitter on a sinusoid of frequency f. It depends on the operating frequency f, the $ENoB_{DC}$ and the RMS timing jitter (σ_{tj}). This term is always $<$0 and therefore timing jitter always degrades the ENoB. The impact of timing jitter increases as the operating frequency increases, Fig.

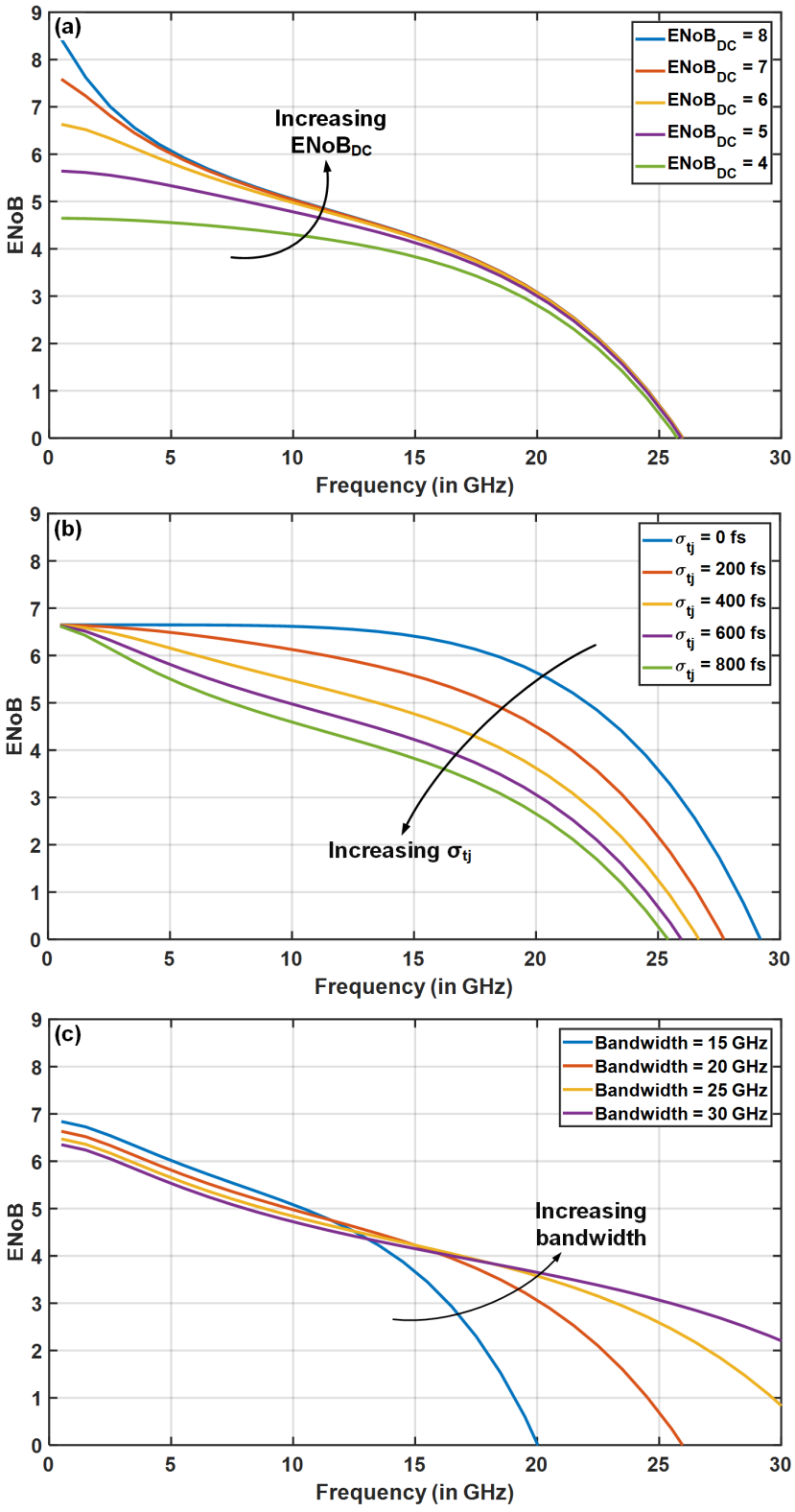

Figure 3.2: Variation of ENoB with frequency for different (a) $ENoB_{DC}$ (b) RMS timing jitter (σ_{tj}) (c) bandwidth. The frequency response is modeled as a fifth order Gaussian filter. When not varied, the parameters are fixed to $ENoB_{DC}$ = 6, σ_{tj} = 600 fs, f_B = 32 GHz and fifth order Gaussian filter bandwidth = 20 GHz

3.2(b). The distortions added due to timing jitter is a random process with no memory.

The third term on the RHS of Eqn. 3.1, $\log_2|H(f)|$ accounts for bandwidth limitations. Limited bandwidth reduces the power of the desired signal, thus reducing the SINAD and $ENoB(f)$, Fig. 3.2(c). $H(f)$ is the normalized frequency response with $|H(f)| \leq 1$, and just like timing jitter, exclusively reduces the ENoB.

The final term in Eqn. 3.1 is known as the processing gain [145]. The limited bandwidth of a DAC suppresses noise and distortions in the generated signal in its high frequency regime. The reduction in noise and distortion power increases the SINAD, which in turn increases the ENoB of the device. In essence, processing gain accounts for the coloration of thermal and quantization noise caused by the DAC's frequency response. For a given frequency response, $H(f)$, and measurement bandwidth, f_B, the processing gain is a constant. The effects of processing gain are evident in Fig. 3.2(a)-(b) where it increases the ENoB at low frequencies by $\sim$0.5 bits more than $ENoB_{DC}$, and in Fig. 3.2(c), where it improves the ENoB at low frequencies for lower bandwidth devices as noise and distortions in higher frequencies are suppressed by bandwidth limitations.

Since ADCs and DACs perform essentially the same operation in opposite orders, the variation of ADC ENoB with frequency is described by a relation similar to Eqn. 3.1, and is given by

$$ENoB(f) = ENoB_{DC} - \frac{1}{2}\log_2\left(1 + 6\left(2^{ENoB_{DC}\pi f\sigma_{tj}}\right)^2\right) + \log_2|H(f)| \qquad (3.2)$$

There is no processing gain in ADCs as the incoming signal is filtered before it is affected by ADC distortions, especially quantization.

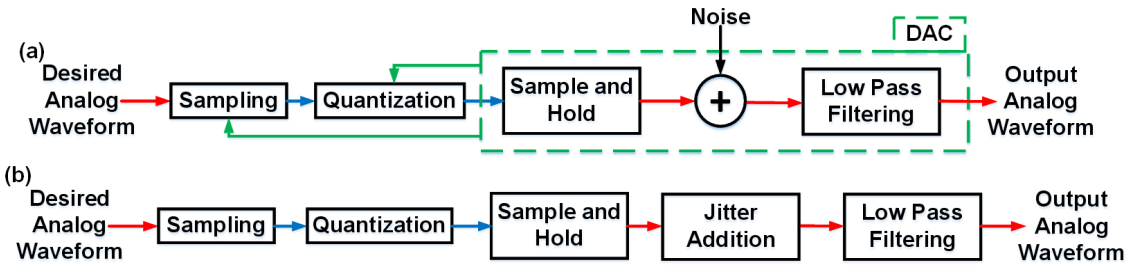

Figure 3.3: (a) Block diagram representing the primary operations of a DAC. Blue arrows represent digital signals and red arrows represent analog signals. Green dashed box represents the DAC hardware. Sampling and quantization requires the DACs operation parameters to pre-process the signal before loading into the DAC memory. Timing jitter is added in the sample-and-hold operation in a real DAC. (b) Block diagram of the model presented in this paper. Quantization includes hardware bit architecture limited quantization and noise. Timing jitter is added separately to make the model efficient. Similarity between the two block diagrams is representative of the accuracy of the model

3.2 DAC Model

3.2.1 Model Description

Figure 3.3(a) shows a simplified block diagram of a DAC. We presume a digital preprocessing unit, such as an ASIC, has created a digitized version of the desired analog waveform. Prior to latching into the DAC, the sampling rate of this digital signal must match that of the DAC. Furthermore, the number of bits of the digital signal is presumed to be equal to the DAC hardware architecture. The parameters of these operations (sampling rate and hardware bit architecture) are therefore dictated by the DAC and we include sampling and quantization in the model even though these are not performed by a real DAC.

Although Eqn. 3.1 accurately depicts the jitter impairments to ENoB, the optimum serial simulation order is not obvious. We examined the performance of many permutations of the processes within a DAC and determined an optimum processing order, Fig. 3.3(b). Some other permutations that were explored include performing quantization before sampling, adding jitter after filtering etc. Throughout our discussion of MATLAB based simulations, we will use “analog signals” to refer to highly oversampled digital signals as it is

not possible to implement analog signals in a simulation environment. The oversampling factor employed here is 64.

The input to the model is the ideal desired analog waveform. This signal is first sampled at the DAC sampling rate. The sampled digital signal is then quantized based on the resolution of the DAC using $ENoB_{DC}$. For now, we will analyze uniform resolution levels. In a real digital system with a DAC, quantization is inherent in the digital hardware and the ENoB is reduced by DAC noise. In our model, we include the effects of thermal noise by quantizing to amplitude levels dictated by $ENoB_{DC}$. This is done to minimize the complexity of the model and reduce the number of independent variables. Note that the effectiveness of this method relies on the input signal being essentially random (such as communication signals). If trivial signals (such as constant signals) were passed through this model, $ENoB_{DC}$ would not be able to account for thermal noise and the model would require an additional block that would add AWGN noise to the signal on a per sample basis. However, for the purposes of simulating optical communication systems, this is not required and we will not discuss such an implementation.

Within the model, the quantized digital signal is converted to an analog signal using a sample-and-hold operation and timing jitter is added to this signal. Finally, the analog signal with timing jitter is passed through a low pass filter, characterized by $H(f)$, to yield the output analog waveform.

In a real DAC, the quantized sample passes through the sample-and-hold operation, which adds timing jitter to the signal in the time domain. However, simulating this is not practical. For state-of-the-art DACs employed in optical communication systems, RMS timing jitter is typically on the order of 100s of femtoseconds (refer to Walden plot [146]), whereas simulations are performed with a temporal resolution of a few picoseconds. Simulations with jitter added directly in the time domain require commensurately finer temporal resolution making them computationally expensive and time consuming. We circumvent this problem by determining an effective amplitude jitter resulting from the specified tim-

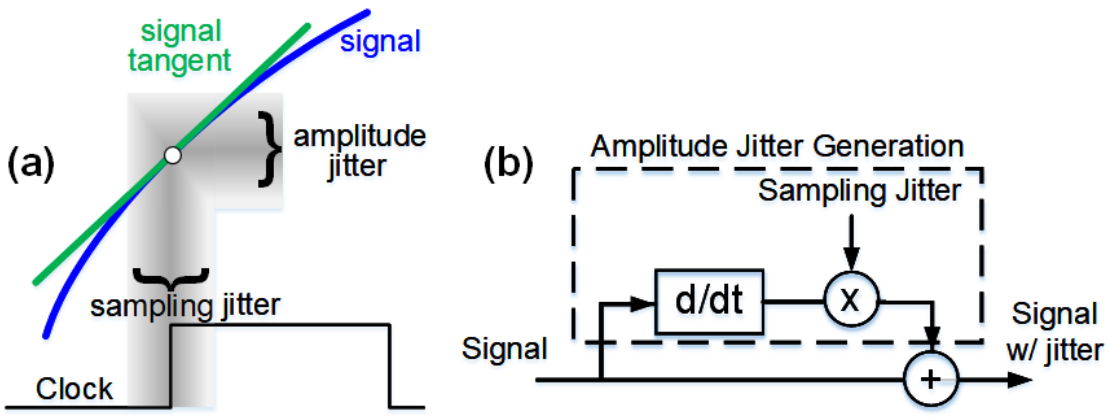

Figure 3.4: (a) For small timing jitters, an equivalent amplitude jitter can be derived using the derivative of the analog signal. (b) The timing jitter block adds the effects of timing jitter to the signal by taking the derivative of the input signal, multiplying it with the required timing jitter and adding it back to the signal

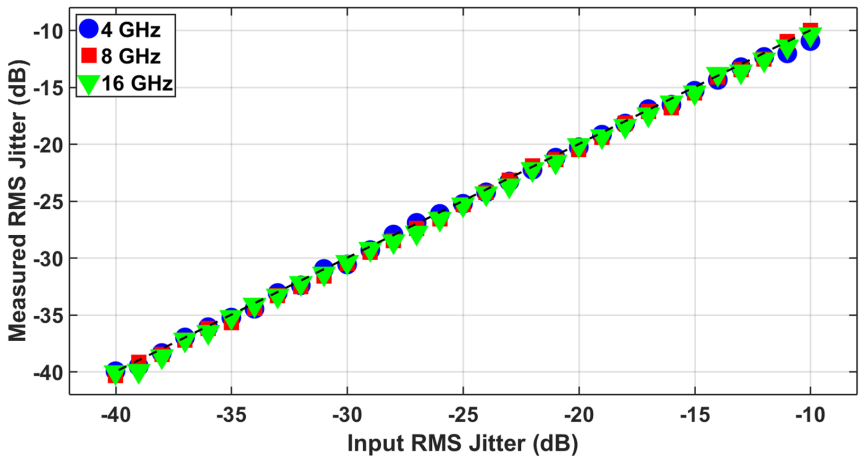

Figure 3.5: Input RMS timing jitter versus measured RMS timing jitter for 4, 8 and 16 GHz sinusoids. RMS jitter (dB) = $10\log_{10}(f.\sigma_{tj})$ where f is the sinusoidal frequency and σ_{tj} is the timing jitter. For small sampling jitters, the measured jitter and input jitter were approximately equal.

ing jitter. The signal after the sample-and-hold is associated with an ideal clock and the equivalent amplitude jitter is simply added to this analog signal. If the timing jitter ΔT is much smaller than its sampling period, an equivalent amplitude jitter ΔX can be calculated from the derivative of the analog signal dx/dt, Fig. 3.4(a)

$$\Delta X = \frac{dx}{dt}\Delta T \tag{3.3}$$

ΔX is then added to the analog signal to simulate timing jitter, Fig. 3.4(b). We validated this procedure by adding specific RMS timing jitter as an equivalent amplitude jitter to sinusoids at different frequencies and observing the resulting timing jitter. Over three orders of magnitude, the input RMS timing jitter and the measured RMS jitter were essentially identical, Fig. 3.5. Choices of frequency were arbitrary and the results would be consistent for any choice of sinusoidal frequency.

Figure 3.6(a)-(f) depicts how a signal transforms as it progresses through different blocks of the model. For this illustration, the input is a 15 GHz sine wave, Fig. 3.6(a). The digital preprocessing first samples the signal at a DAC sampling rate of 64 GSa/s, Fig. 3.6(b). The sampled signal is then quantized with an $ENoB_{DC}$ of 6.5 bits, Fig. 3.6(c). An ideal sample-and-hold operation is then performed on the quantized samples, Fig. 3.6(d). Subsequently, a 600 fs timing jitter, in the form of an equivalent amplitude jitter, is added to the signal. Note that due to the ideal sample-and- hold operation, the derivative of the analog signal is zero except at the transitions. Therefore, the equivalent amplitude jitter is only added at these samples, Fig. 3.6(e). Such an implementation is computationally efficient since jitter needs to be computed only at transitions. Finally, the signal is low pass filtered, (5^{th} order Gaussian, 20 GHz bandwidth), Fig. 3.6(f). Note that jitter addition and low pass filtering are linear operations and switching their order yields the same output. The output amplitude is lower than the input due to the frequency response of the low pass filter. Lastly, to better visualize the effectiveness of our model, we constructed eye

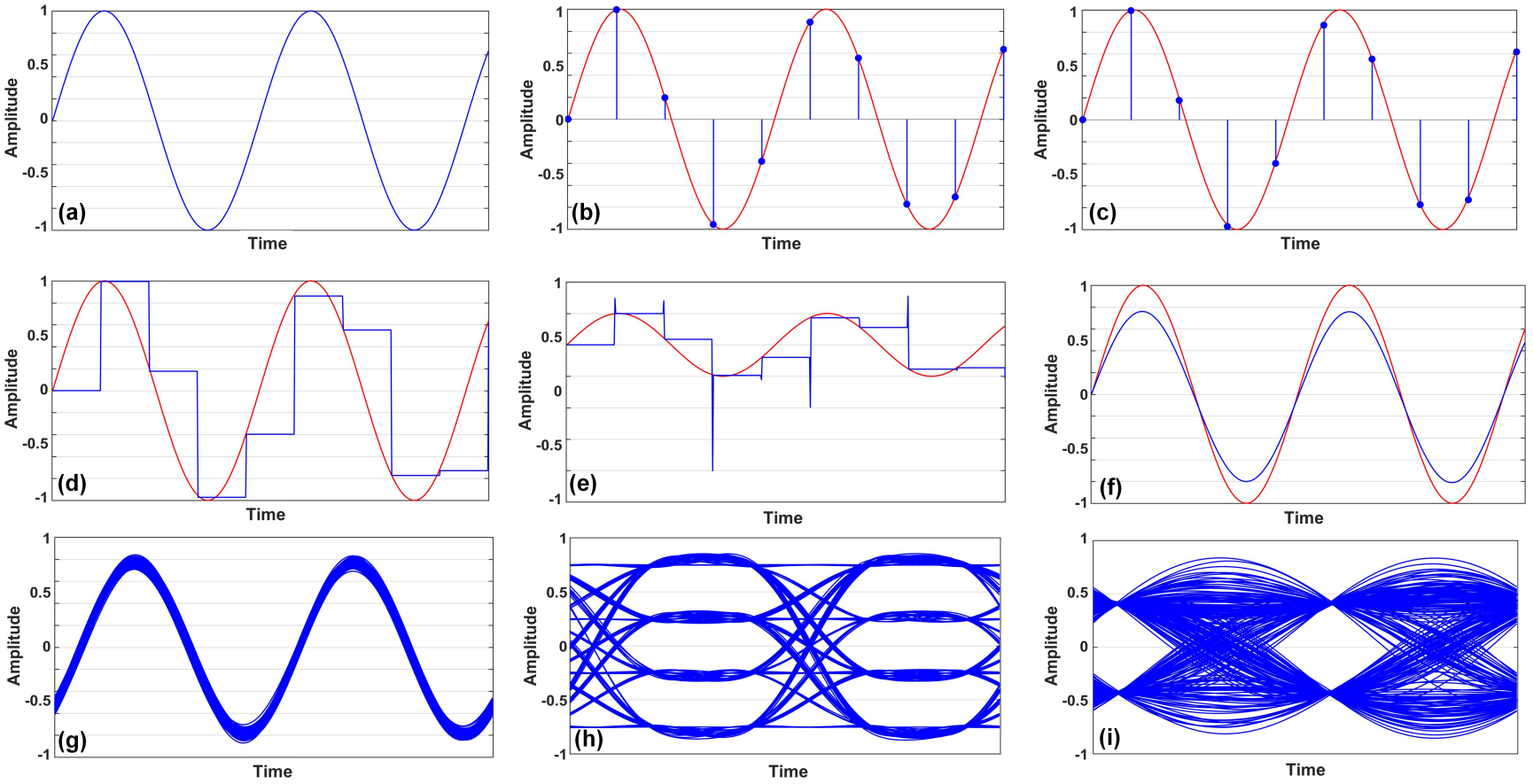

Figure 3.6: (a)-(f) Signal progression through each block in the DAC model. Parameters of the simulated DAC are : $ENoB_{DC}$ = 6.5 bits, sampling rate = 64 GSa/s, RMS timing jitter = 600 fs and a 5th order Gaussian low pass filter with 20 GHz bandwidth (a) Input sine wave (15 GHz) Signal after (b) sampling at sampling rate, (c) quantizing at $ENoB_{DC}$ (d) ideal sample-and-hold (e) jitter addition (f) low pass filtering. Red curve in (b)-(f) is the input waveform to the model that can be used for comparison. (g) Eye diagram of the output sine wave. Output of the DAC model for (h) a PAM-4 signal with rectangular pulse shaping (i) a PAM-2 signal with RC shaping (roll-off = 0.1)

diagrams of three signals: 15 GHz sinusoids, PAM-4 with rectangular pulse shaping and PAM-2 with raised cosine pulse shaping at a roll-off of 0.1, Fig. 3.6(g)-(i). The effects of the DAC, especially those of timing jitter and bandwidth limitations are clearly visible.

3.2.2 Model Validation

Exhaustive validations were performed between the simulation model and theory, Eq.3.1, and consistent results were obtained in all cases. DAC ENoBs were calculated using the SINAD, estimated from the device's sinusoidal outputs and Eq. 2.43. More details about the procedure can be found in [75]. Figure 3.7 shows three examples where $ENoB_{DC}$ = 6.5 bits and the low pass filter was modeled as a 10$^{\text{th}}$ order Gaussian with a bandwidth of 20 GHz. For all investigated cases of timing jitter, there is a close agreement between theory and our model. Small deviations were observed in cases where the DAC was mostly quantization limited (low RMS timing jitter). This results from the use of sinusoids which yield deterministic distortions when quantized, whereas the theory assumed that quantization creates additive white noise. However, the effects of such deviations can be ignored because the deviations are small and practical DACs have much higher timing jitter.

We next demonstrate the ability of our model to simulate frequency dependent ENoB such as those exhibited by real DACs by comparing it with experimental ENoB obtained from two commercially available DACs. The DAC ENoBs were measured using a 14-bit wide-bandwidth oscilloscope following the procedures described in [75]. By appropriately choosing the model parameters, we are able to closely match the behaviors for both the DACs, Fig. 3.8. The frequency response, $H(f)$, of the DACs was measured using a range of test tones and thereby creating the DAC transfer function. The response of each DAC was approximated as an n$^{\text{th}}$ order Gaussian response and implemented as a low pass filter for each model. It is to be noted that the model can readily accommodate for any filter response and is not restricted to just Gaussian profiles. The sampling rate used for the model was that of the device under test. Finally, the RMS timing jitter (σ_{tj}) and $ENoB_{DC}$ were obtained

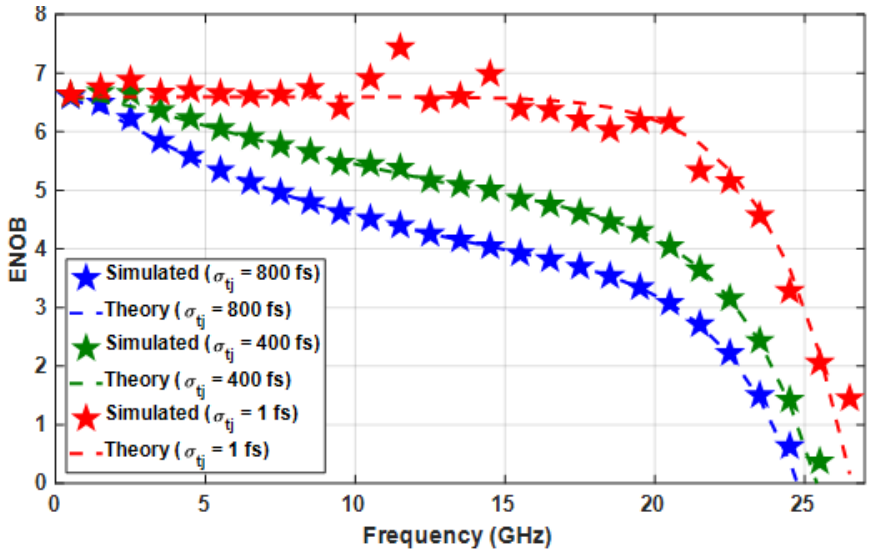

Figure 3.7: DAC parameters $ENoB_{DC}$ = 6.5 bits, sampling rate = 92 GSa/s and a low pass filter of 22 GHz bandwidth modeled as a 10th-order Gaussian. RMS timing jitters of 1 fs, 400 fs and 800 fs were simulated. Close match between theory and simulation was obtained for 400 fs and 800 fs of timing jitter. For quantization-limited cases (low RMS timing jitter), small deviations were observed since the assumption that quantization noise is white does not hold for periodic signals

using curve fitting and Eq. 3.1. These three parameters yield excellent agreement between the simulation model and experimental results. We find that these commercial DACs have an RMS jitter of 500 to 700 fs. This correspond to an ENoB of 4 to 4.8 bits at 10 GHz input frequency, which is in close agreement with Heisenberg limit [146].

3.3 ADC Model

3.3.1 Model Description

Similar to the DAC model, we developed an ADC model to capture the frequency dependent ENoB exhibited by wideband ADCs, Fig. 3.9. The input to the model is the input analog waveform that we wish to digitize. Firstly, the input signal is low-pass filtered based on the ADC filter profile - $H(f)$. Then timing jitter is added to the signal based on the ADC RMS timing jitter - σ_{tj}. This jittered signal is then downsampled based on the sampling rate of the simulated ADC. Finally, the samples are quantized to appropriate

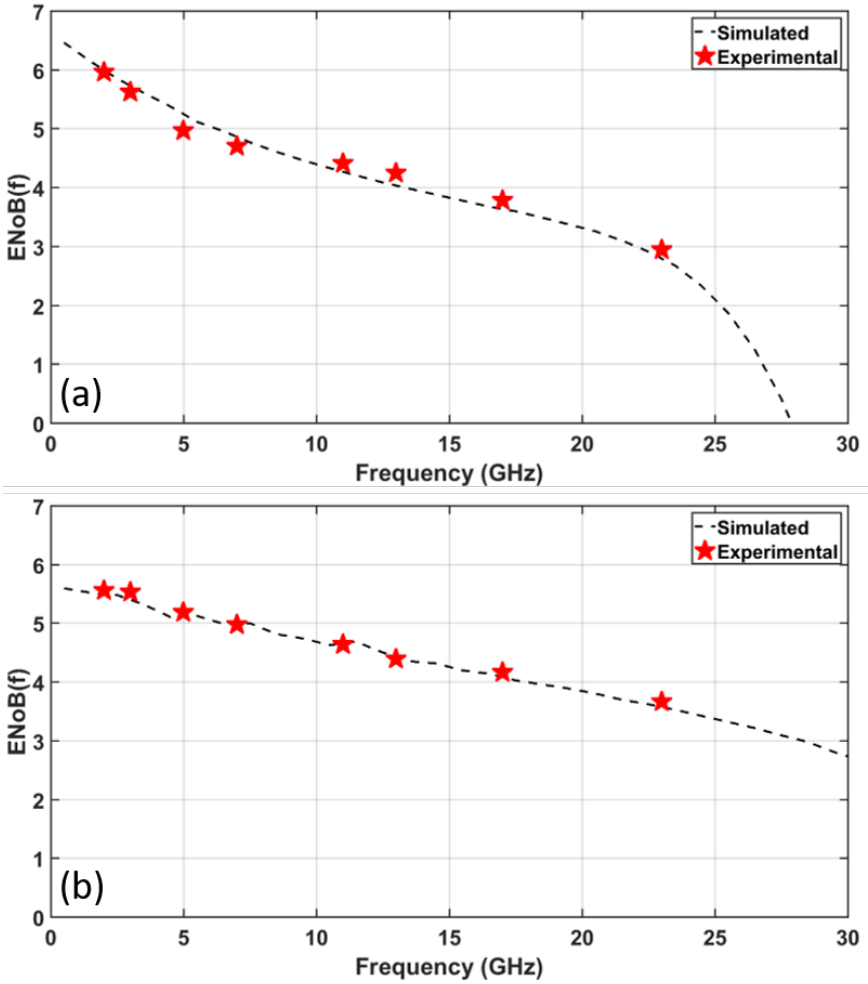

Figure 3.8: Experimental versus simulated ENoB for two commercially available DACs. Parameters used for the simulated model (a) $ENoB_{DC}$ = 6 bits, σ_{tj} = 700 fs and bandwidth = 25 GHz (b) $ENoB_{DC}$ = 5 bits, σ_{tj} = 500 fs and bandwidth = 30 GHz

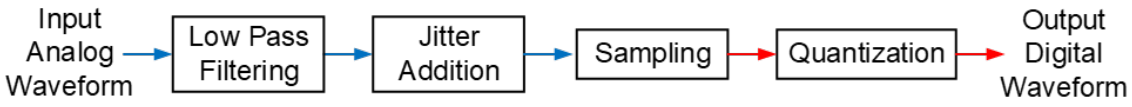

Figure 3.9: Block diagram of the ADC model. Red arrows represent digital waveforms and blue arrows represent analog waveforms. Sampling refers to the process of digitizing the analog waveform based on the sample rate of the ADC. Timing jitter is added based on the RMS timing jitter of the ADC and low-pass filtering is performed based on the filter profile of the ADC

resolution levels.

Figure 3.10 shows the progression of an 11.5 GHz sinusoid through our ADC model - input sinusoid, Fig. 3.10(a); signal after low-pass filtering (33 GHz bandwidth, near brick wall filter) and jitter addition (σ_{tj} = 400 fs), Fig. 3.10(b); and signal after downsampling (sampling rate = 80 GSa/s) and quantization ($ENoB_{DC}$ = 5 bits), Fig. 3.10(c). Input signal is represented in red in Fig. 3.10(b)-(c) for the purposes of comparison.

3.3.2 Effects of DNL and INL

In order to understand the effects of DNL and INL on frequency dependent ENoB, we simulated multiple DACs and ADCs with varying amounts of DNL and INL, Fig. 3.11. DNL is generated using a uniformly distributed random variable [143],

$$DNL[k] = U\left(-\frac{LSB}{2}, \frac{LSB}{2}\right) \tag{3.4}$$

where the arguments of $U(.)$ are the bounds of the uniform random variable and k refers to the k^{th} resolution level. INL of the k^{th} level is given by,

$$INL[k] = \sum_{m=1}^{k} DNL[m] \tag{3.5}$$

Both DNL and INL are restricted to be within ± 0.5 LSB to ensure that the EC code transitions are monotonic. This assumption is also realistic as modern ECs have $<$0.5 LSB of DNL and INL [74].

Black curves in Fig. 3.11 simulate the average effects of DNL and INL on ENoB as well as the ENoB fluctuations that occurred over 100 simulated DNLs and INLs for the same EC. The parameters of the DAC are - $ENoB_{DC}$ = 6 bits, σ_{tj} = 700 fs and a bandwidth of 25 GHz modeled as a 10$^{\text{th}}$ order Gaussian. Similarly, the parameters of the ADC are - $ENoB_{DC}$ = 5 bits, σ_{tj} = 400 fs and a bandwidth of 33 GHz modeled as a near brick wall filter. The red stars and curve show the simulated and theoretical ENoB respectively for the

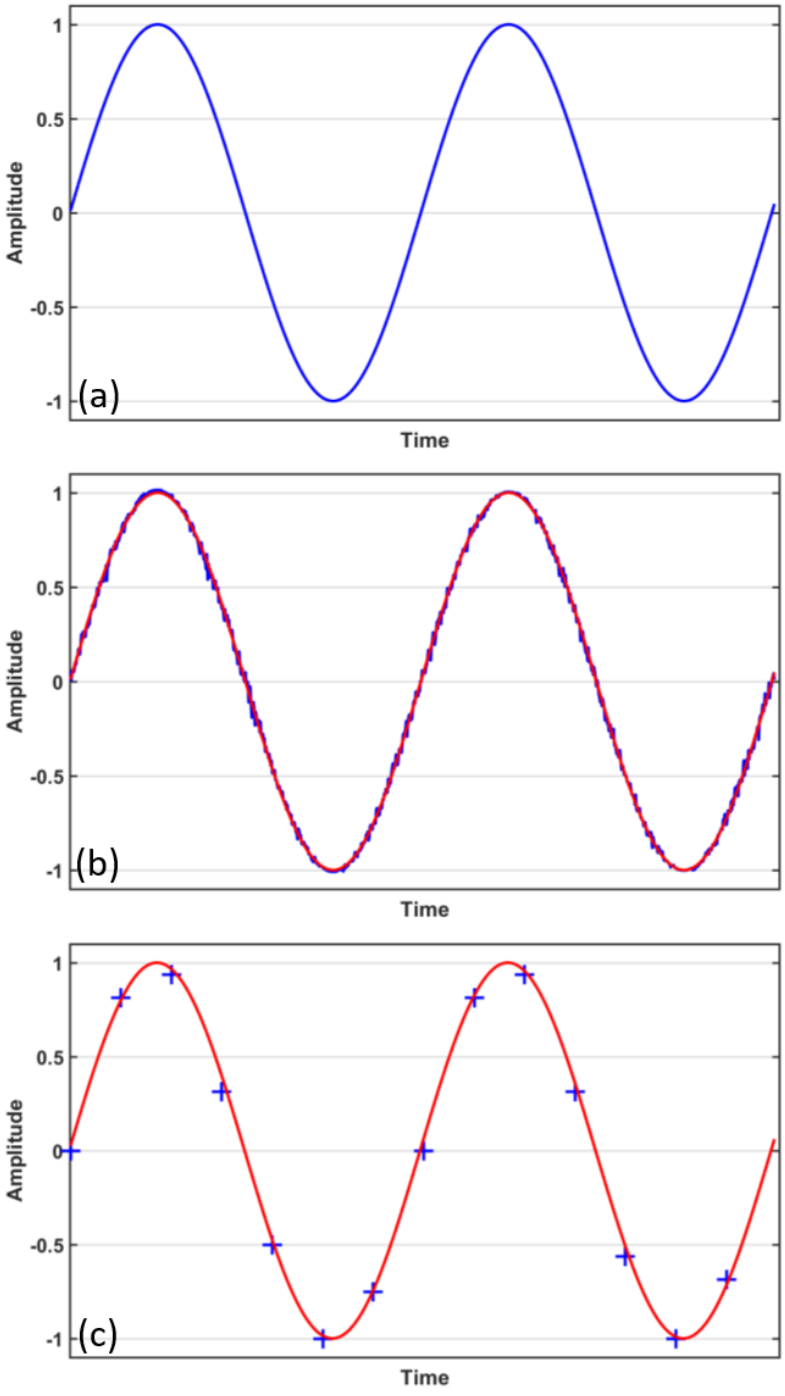

Figure 3.10: Signal progression through the ADC model. (a) input sinusoid of 11.5 GHz. (b) Signal after lowpass filtering and addition of timing jitter. The lowpass filter is a brick wall filter with 33 GHz of bandwidth. RMS of timing jitter is 400 fs. (c) Signal after downsampling at 80 GSa/s and quantization at $ENoB_{DC}$ = 5 bits

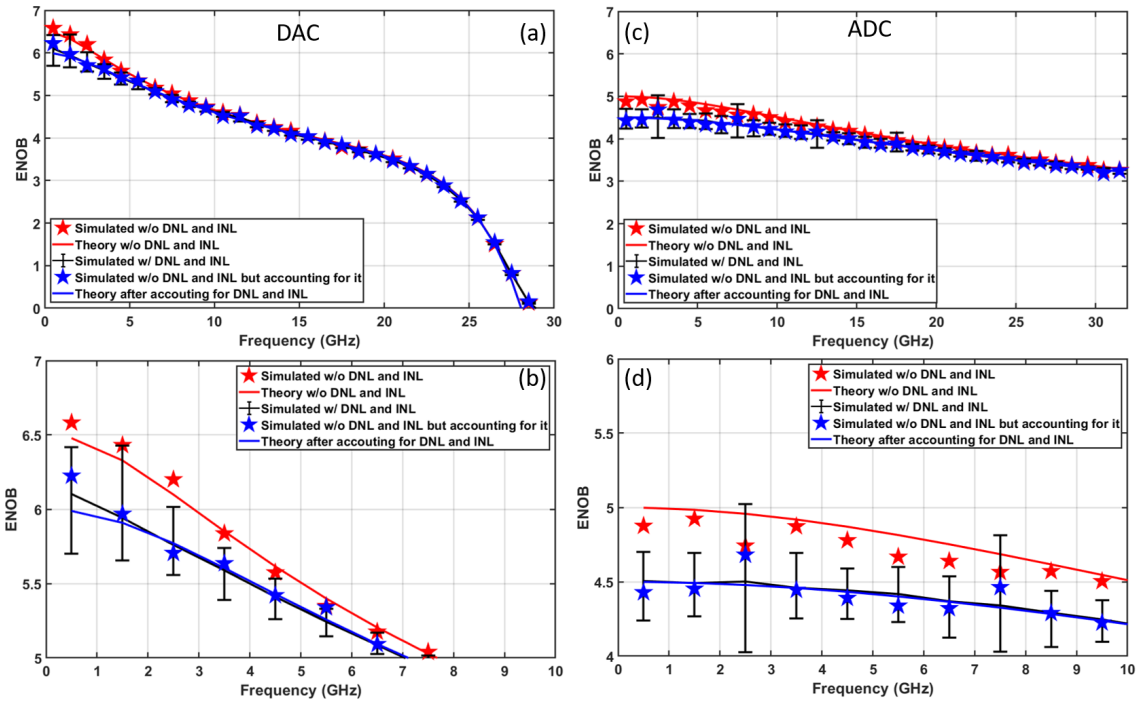

Figure 3.11: Comparison between ECs with uniform quantization levels and ECs with DNL and INL. DAC parameters are - $ENoB_{DC}$ = 6 bits, σ_{tj} = 700 fs and bandwidth = 25 GHz modeled as a 10th order Gaussian. ADC parameters are - $ENoB_{DC}$ = 5 bits, σ_{tj} = 400 fs and bandwidth = 33 GHz modeled as a near brick wall filter. Black curve show the average frequency dependent ENoB for 100 (a) DACs and (c) ADCs with a maximum DNL and INL of $\pm$0.5 bits. Magnitude variations in these ENoB are also shown as bars. The red curve is the theoretical frequency dependent ENoB for the same ECs without DNL and INL. Red stars are the corresponding model output. The blue curve attempts to theoretically model these ECs without DNL and INL. Blue stars are the corresponding simulated outputs. For sufficiently small DNL and INL, appropriate modifications in $ENoB_{DC}$ is sufficient to model its effects on ECs. (b) and (d) shows the variation of ENoB between 0 and 10 GHz from (a) and (c) respectively. The effects of DNL and INL are predominant at low frequencies

same EC without any DNL or INL. The effects of DNL and INL are predominant in the low frequency regime (or the quantization dominant regime), Fig. 3.11(b) and (d), and the characteristics of an EC with DNL and INL eventually converge to the characteristics of an EC without DNL and INL as the frequency increases.

The blue curve attempts to model the previously discussed EC that is affected by DNL and INL, by finding the theoretical EC parameters (Eqn. 3.1 and Eqn. 3.2) having equivalent performance. The blue stars show the corresponding simulated EC performance without DNL and INL. The blue curve and stars are well-fit to the average ENoB of the DNL/INL-affected cases which allows for the associated penalties to be assessed by the model as well. The performance difference when accounting for DNL and INL is $\sim$0.5 bits which, due to the frequency independence of this penalty, can be accounted for within $ENoB_{DC}$. Doing so results in tremendous reductions in computational complexity for the model, as full simulations would require time-dependent sample-wise quantization computations for all resolution levels.

Deviations in ENoB at certain frequencies in Fig. 3.11 are an artifact of the white quantization noise assumption. Since sinusoids are used to assess the ENoB of the model, the effects of quantization are signal dependent and they do not follow the theory smoothly. These variations can be as high as 1 bit in certain cases.

3.3.3 Model Validation

We exhaustively validated our model with Eqn. 3.2 for various ADC parameters and found consistent agreement between the two, Fig. 3.12. Furthermore, we experimentally compared our model with two commercially available ADCs, Fig. 3.13, using the methodologies described in [147]. ADC ENoBs were experimentally obtained by capturing sinusoids from a high-speed signal generator and measuring the SINAD of the captured signals. Sampling rate of the simulated models in Fig. 3.13 are the sampling rates of the ADCs they are being compared to. Filter profiles, $H(f)$, of the ADCs were measured by capturing a

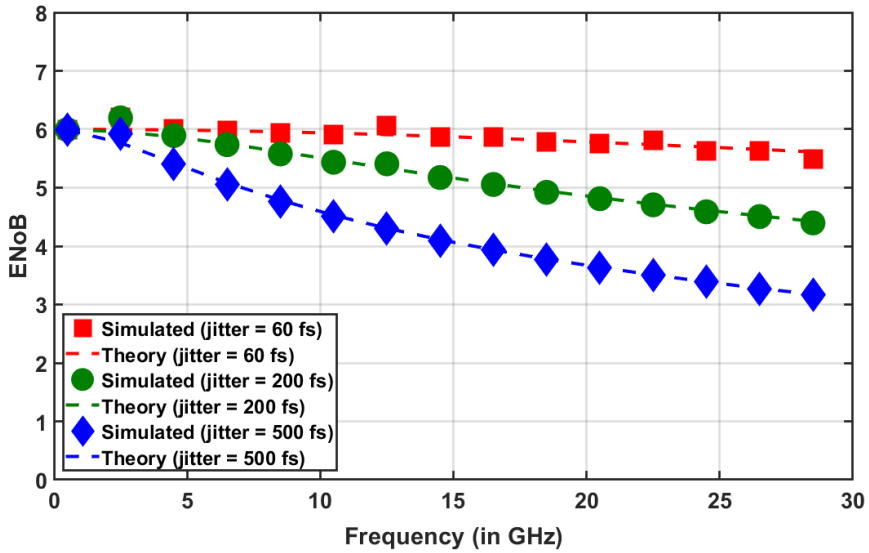

Figure 3.12: ADC parameters $ENoB_{DC}$ = 6 bits, sampling rate = 80 GSa/s and a low pass filter of 33 GHz bandwidth modeled as a near brick wall filter. RMS timing jitters of 60 fs, 200 fs and 500 fs were simulated. Close match between theory and simulation was obtained for all investigated cases

range of test tones and creating the ADC transfer functions. $ENoB_{DC}$ and σ_{tj} were obtained through best-fit between Eqn. 3.2 and the captured ENoBs. Figure 3.13 shows close agreement between the simulated model ENoBs and experimentally obtained ENoBs, and demonstrates the accuracy of our ADC model to simulate real ADCs that are employed in optical communication systems.

3.4 Effects of Frequency Dependent ENoB on Optical Communication Systems

3.4.1 Simulation Setup

In order to assess the impact of frequency dependent ENoB on optical communication systems, we implemented our DAC and ADC model in RSOFTs OptSim simulation environment for various EC parameters and measured their corresponding OSNR penalties. Since we previously identified that the effects of DNL and INL can be included in the model by appropriately changing $ENoB_{DC}$, we will not investigate non-uniform resolution levels separately. We investigate three data rates namely 64 GBaud DP-16QAM (400G), 64

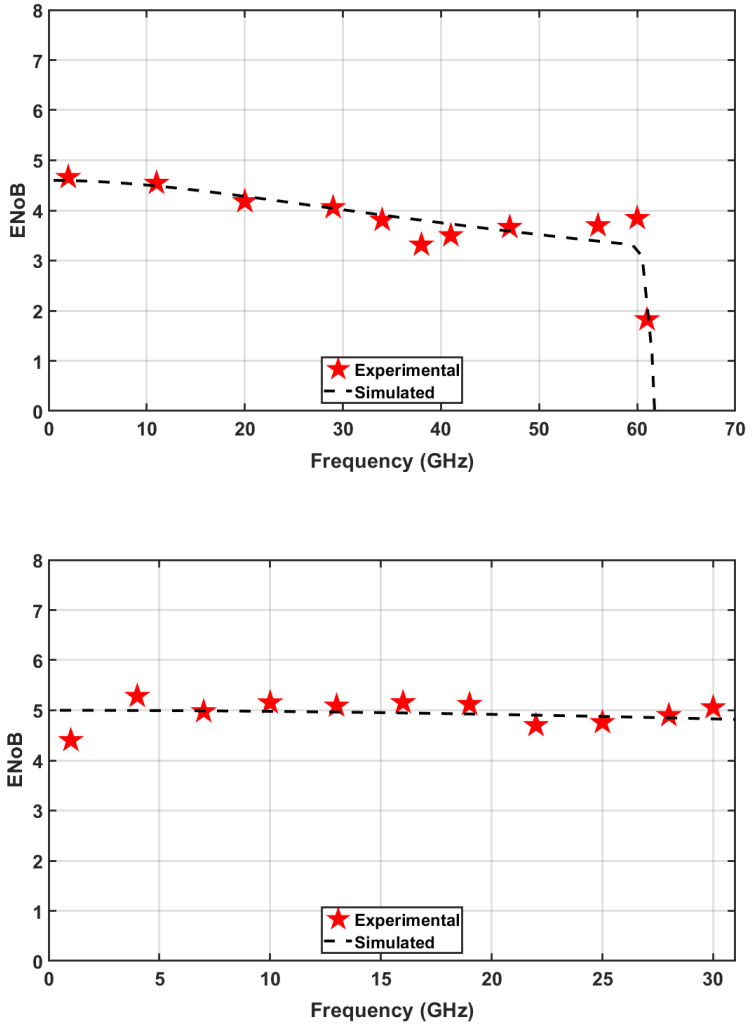

Figure 3.13: Experimental versus simulated ENoB for two commercially available ADCs. Parameters for the simulated ADC are (a) $ENoB_{DC}$ = 4.6 bits, bandwidth = 60 GHz and RMS timing jitter = 200 fs. (c) $ENoB_{DC}$ = 5 bits, bandwidth = 32 GHz and timing jitter = 70 fs

GBaud DP-64QAM (600G), and 96 GBaud DP-32QAM (800G). The signals were generated using a PRBS-15 bit sequence shaped using a root raised cosine pulse shape with a roll-off factor of 0.1. DAC $ENoB_{DC}$ and σ_{tj} are systematically varied to analyze their effects on system performance. The DAC filter is a 5$^{\text{th}}$ order Gaussian filter with a bandwidth of half the symbol rate. The DAC sampling rate was fixed to 240 GSa/s. ECs with oversampling factors $>$1.2 do not provide any additional benefits to the performance [148] and therefore the sampling rate is not varied here. The DAC outputs are used to drive an I/Q Mach-Zehnder Modulator (MZM) with a bandwidth of 60 GHz and extinction ratio of 40 dB. High quality components were purposely chosen for the simulation to ensure they have minimal effects on the signal and all penalties arise from the ECs.

Amplified spontaneous emission (ASE) power is added at the receiver to vary the OSNR of the signal. The signal is not transported through any fiber to ensure no fiber penalties are incurred by the signal. After noise loading, the signal goes through a 150 GHz optical band pass filter (OBPF). Finally, the signal is received by a coherent receiver and digitized using the ADC model. Here, the ADC $ENoB_{DC}$, σ_{tj} and bandwidth are systematically varied to analyze its effects on the signal. The ADC filter shape is near brickwall. The sampling rate of the ADC is fixed to 240 GSa/s. After digitization, the signal passes through our digital coherent receiver (DCR) that is implemented in MATLAB. Conventional DSP methods described in Sec. 2.4 are used here. Finally, symbol decisions are made and OSNR penalties are calculated for BER = 10^{-3}. We note that the different data rates explored here will have different BER thresholds based on the employed FEC. However, we chose the same BER threshold for all data rates to provide a fair comparison between different signal types subject to the same impairment. Large filter lengths were purposely chosen to ensure all observed OSNR penalties arise from EC impairments that cannot be mitigated using linear filters. Significant efforts were made to ensure that our simulation methods closely match our experimental testbed.

3.4.2 Results

For brevity, we refer to systems employing 64 GBaud DP-16QAM, 64 GBaud DP-64QAM and 96 GBaud DP-32QAM as '400G systems', '600G systems' and '800G systems' respectively. Additionally, for ease of discussion, we define the following variables

1. Excess $ENoB_{DC}$ ($EENoB_{DC}$): Defined as $ENoB_{DC} - 0.5 \times \log_2(M)$, where M is the number of constellation points in the modulation format. For 64QAM, $EENoB_{DC}$ = $ENoB_{DC}3$.

2. Relative RMS timing jitter: Defined at the ratio of the RMS timing jitter to that of the symbol period in percentage.

3. Excess bandwidth: Defined as the difference between the EC bandwidth and half the symbol rate.

Unless mentioned otherwise, the following parameters are to be assumed in the following discussions - DAC $EENoB_{DC}$ = 2.5 bits, DAC RMS timing jitter = 450 fs, DAC excess bandwidth = 0 GHz, ADC $EENoB_{DC}$ = 3 bits, ADC RMS timing jitter = 150 fs and ADC excess bandwidth = 4 GHz. Additionally, fixed EC parameters are labeled as the title of individual figures for convenience.

Frequency dependent ENoB introduced significant penalties to all investigated modulation formats. We divide our discussion into three parts to understand how individual parameters of frequency dependent ENoB affect these systems.

Bandwidth

Excess DAC bandwidth = 0 GHz did not introduce any OSNR penalties in all investigated systems. Any bandwidth limitation was compensated by the receiver adaptive DSP filters.

The effects of ADC bandwidths were relatively minor in the presence of $>$4 GHz of excess bandwidth for all investigated systems, Fig. 3.14. Excess bandwidths $<$2 GHz could not be supported due to Nyquist requirements and the near brick-wall filter employed here.

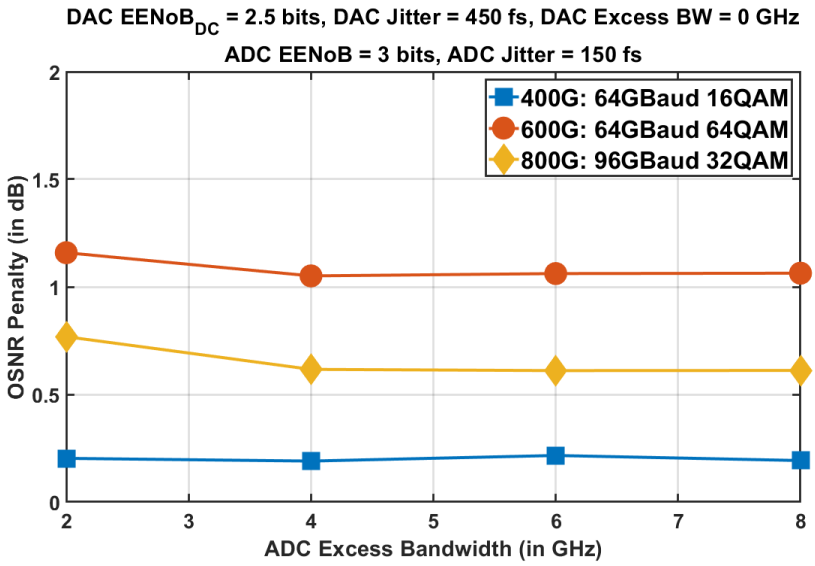

Figure 3.14: OSNR penalties for various ADC excess bandwidths. Excess bandwidths >4 GHz did not introduce any penalties in all investigated systems. Excess bandwidths <2 GHz could not be supported due to Nyquist requirements and the near brickwall filter employed here. Variations in OSNR penalties between different systems are caused by other EC parameters

Timing Jitter

Unlike bandwidths, DAC timing jitter introduced significant penalties in all investigated systems, Fig. 3.15. The effects of DAC timing jitter also strongly depended on the operating DAC $ENoB_{DC}$. As an example, for 400G systems, increasing the DAC RMS timing jitter from 0 fs to 900 fs incurred a penalty of 0.4 dB for DAC $EENoB_{DC}$ = 3 bits, and 0.8 dB for DAC $EENoB_{DC}$ = 1.5 bits, Fig. 3.15(a). The compounded effects are due to the order in which the processes take place in a DAC.

As expected, DAC timing jitter has worse impact on systems employing larger modulation formats and higher symbol rate, Fig. 3.16. Interestingly, for the same RMS timing jitter, 600G system and 800G system investigated here demonstrated similar OSNR penalties. Decreasing the constellation size from 64QAM to 32QAM counterbalanced the increase in symbol rate from 64 GBaud to 96 GBaud, neutralizing some additional effects of DAC timing jitter on the system. For a given timing jitter, a careful investigation of symbol

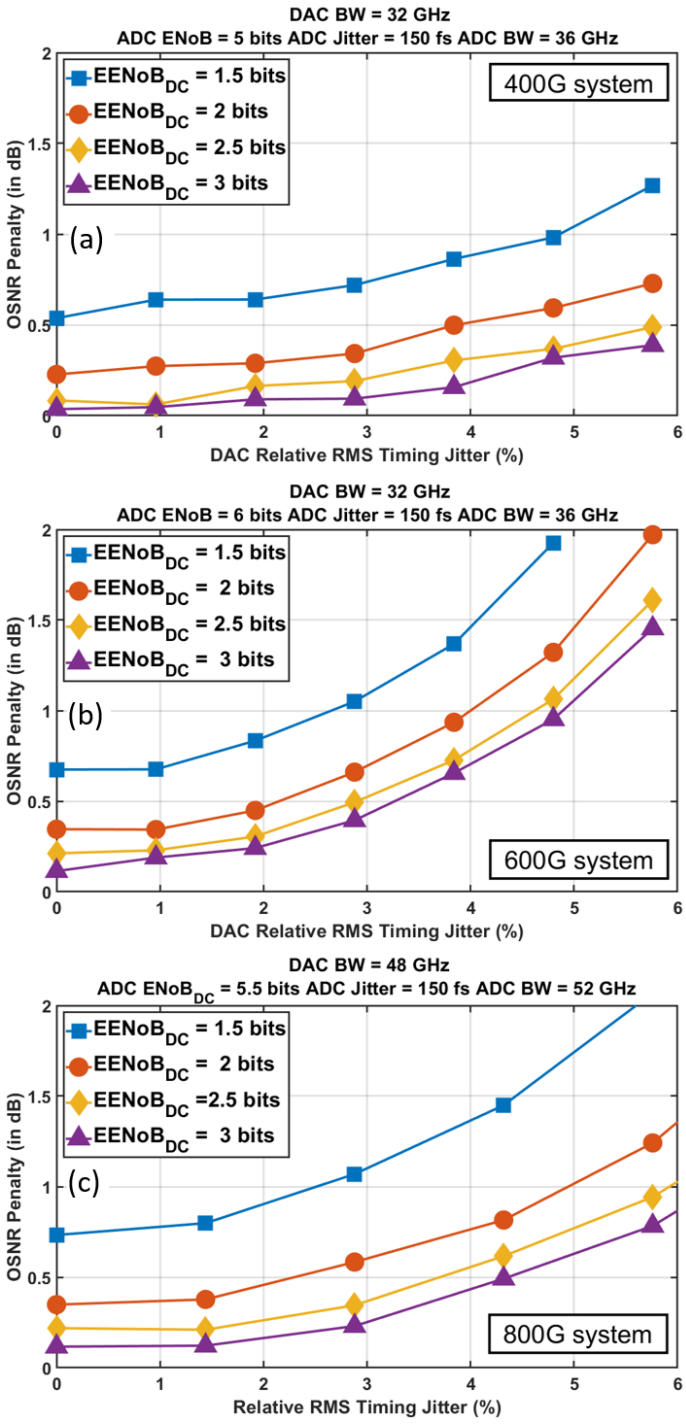

Figure 3.15: OSNR penalties for various DAC relative timing jitter and DAC $EENoB_{DC}$ for (a) 400G system, (b) 600G systems, and (c) 800G systems. Effects of DAC timing jitter strongly dependent on the operating DAC $(E)ENoB_{DC}$, the modulation format and the symbol rate

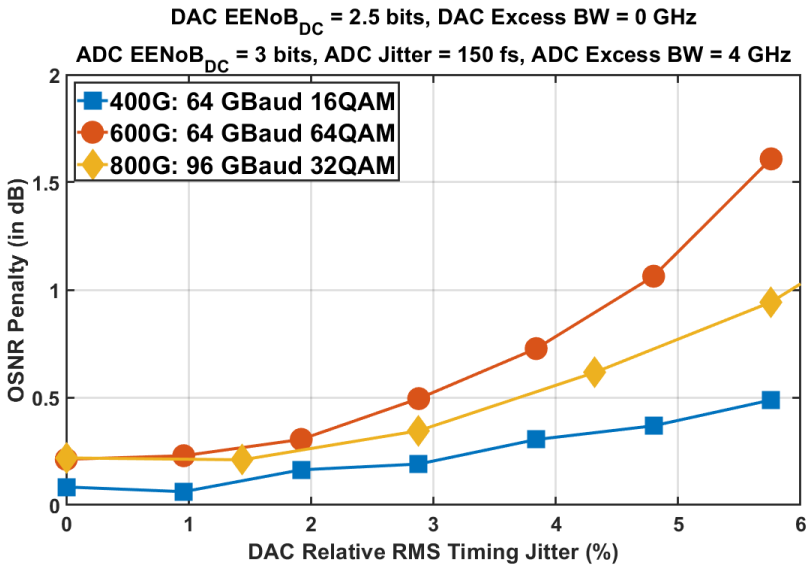

Figure 3.16: OSNR penalties for various DAC relative timing jitter for various systems. Higher modulation formats are affected more by DAC timing jitter. Careful trade-offs between modulation formats and symbol rates is required to maximize the system bit rate in the presence of timing jitter

rate and modulation format is required to maximize system margin or bitrate.

All investigated systems suffered approximately twice the penalty from ADC timing jitter when compared to DAC timing jitter, Fig. 3.17. For example, in 800G systems, 3% relative ADC timing jitter introduced the same penalties as 5% relative DAC timing jitter. Increased timing jitter accuracy is required at the ADC to enable the DSP to correct other system impairments effectively. Unlike DACs, effects of ADC timing jitter were found to be independent of other EC parameters investigated here, due to the order of different processes in an ADC.

The following are the (DAC, ADC) relative timing jitter requirement pairs to ensure $<$0.5 dB OSNR penalty - (6%, 4%) for 400G, (3.5%, 2%) for 600G and (5%, 3%) for 800G. DAC timing jitter requirements were computed in the presence of DAC $EENoB_{DC}$ of 2.5 bits. For lower DAC $EENoB_{DC}$, these DAC timing jitter tolerances would be lower.

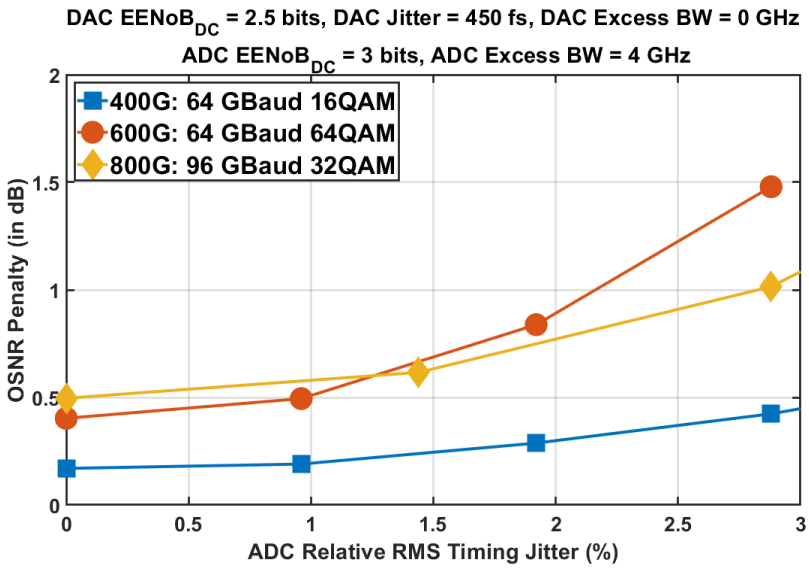

Figure 3.17: OSNR penalties for various ADC relative timing jitter for various systems. Systems are less tolerant to ADC timing jitter when compared to DAC timing jitter

$ENoB_{DC}$

OSNR penalties introduced by DAC $ENoB_{DC}$ exponentially increased as $ENoB_{DC}$ decreased, Fig. 3.18. Additionally, it was observed that DAC quantization introduced no penalties when $EENoB_{DC} \geq 3$ bits. As expected, penalties introduced by DAC $ENoB_{DC}$ did not depend on the symbol rate and only depended on the employed modulation format.

All investigated systems were observed to be more sensitive to ADC $ENoB_{DC}$ as compared to DAC $ENoB_{DC}$, Fig. 3.19. While DAC $EENoB_{DC}$ >1.5 bits was sufficient to incur <1 dB OSNR penalties, ADC $EENoB_{DC}$ had to be $\geq$ 2.5 bits for the same. However, ADC $EENoB_{DC} \geq 3$ bits did not provide any additional benefits to the system, similar to DAC $ENoB_{DC}$. Such patterns demonstrate the need for higher ADC conversion accuracies at the receiver to enable DSP algorithms to compensate for other system impairments well.

To incur <1 dB OSNR penalties, DAC $EENoB_{DC}$ needs to be >1.5 bits and ADC $EENoB_{DC}$ needs to be >2.5 bits. Assessments in [149] overestimated DAC $EENoB_{DC}$ requirements (>2 bits) for 64QAM due to the lack of DAC/ADC models that can simu-

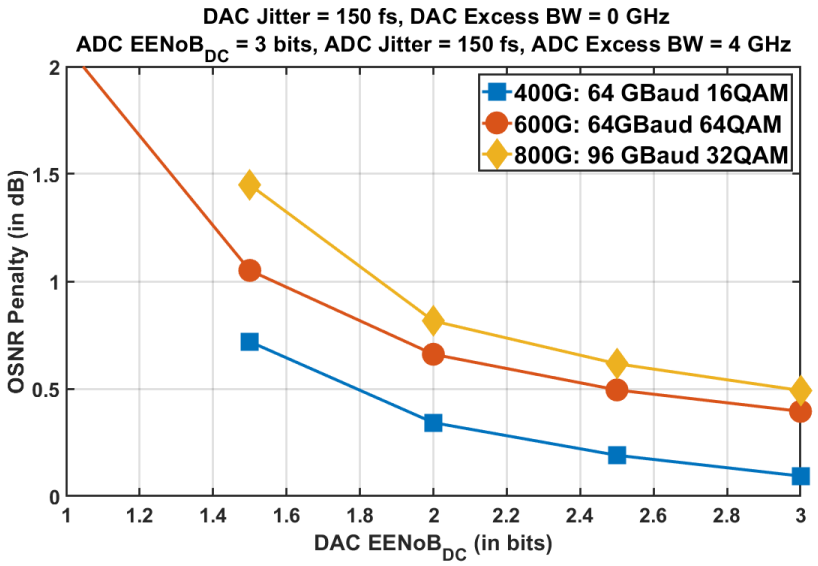

Figure 3.18: OSNR penalties for various DAC $EENoB_{DC}$ for various systems. DAC $EENoB_{DC}$ severely affected the performance of all investigated systems. Penalties solely depended on the operating modulation format

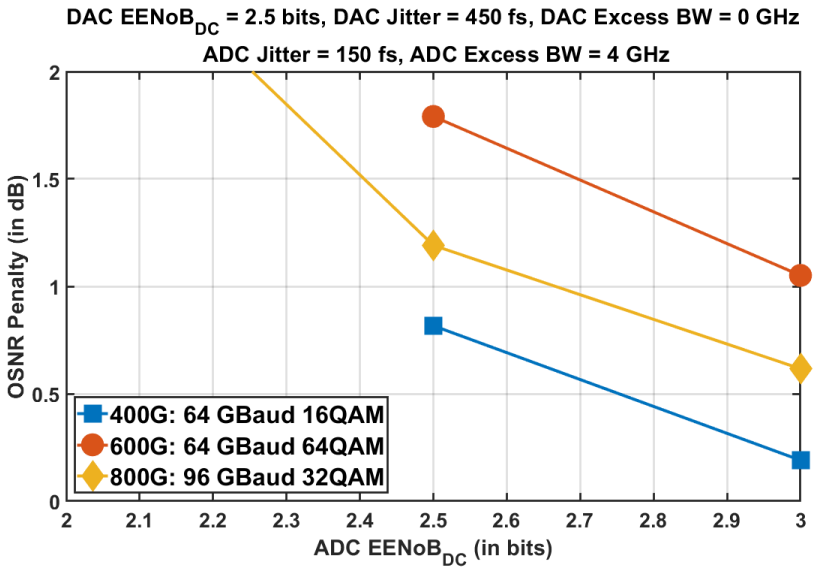

Figure 3.19: OSNR penalties for various ADC $EENoB_{DC}$ for various systems. ADC $EENoB_{DC}$ also severely affected the performance of all investigated systems. They were more sensitive to ADC $ENoB_{DC}$ when compared to DAC $ENoB_{DC}$

Table 3.1: EC parameters used to train the neural network

Parameter	Values
Modulation format	2 (16QAM), 2.5 (32QAM), 3 (64QAM)
DAC $EENoB_{DC}$	1, 1.5, 2, 2.5, 3 bits
DAC σ_{tj}	0, 150, 300, 450, 600, 750, 900 fs
ADC $EENoB_{DC}$	1, 1.5, 2, 2.5, 3 bits
ADC σ_{tj}	0, 150, 300, 450, 600, 750, 900 fs
ADC Excess bandwidth	2, 4, 6, 8 GHz

late frequency dependent ENoB. Once again, $EENoB_{DC} > 3$ bits do not provide any additional benefits for DACs and ADCs. All OSNR penalties observed in Fig. 3.18-3.19 at $EENoB_{DC}$ = 3 bits are due to ADC and DAC timing jitter, and this can be verified through Fig. 3.15-3.17.

3.4.3 Machine Learning based Regression

Finding an analytical solution to estimate the performance impact for various EC parameters is challenging due to the nonlinear relationship between these parameters and associated OSNR penalties. However, this information is invaluable during network planning as it allows for enhanced margin assessment for optical links. In order to obtain such a tool, we employed simple NNs to derive a regression that takes the EC parameters, modulation format and symbol rate as its input and gives the OSNR penalties as its output.

The neural network consists of a single hidden layer with 10 neurons. The size of the neural network was chosen to ensure minimum regression error and minimum computational complexity. The input to the neural network is a vector containing the following parameters - modulation format, DAC and ADC $EENoB_{DC}$, DAC and ADC relative RMS timing jitter, and the ADC bandwidth. The network was trained using data obtained for 400G, 600G and 800G systems through our simulation setup for various EC parameters. The parameters are listed in Table 3.1.

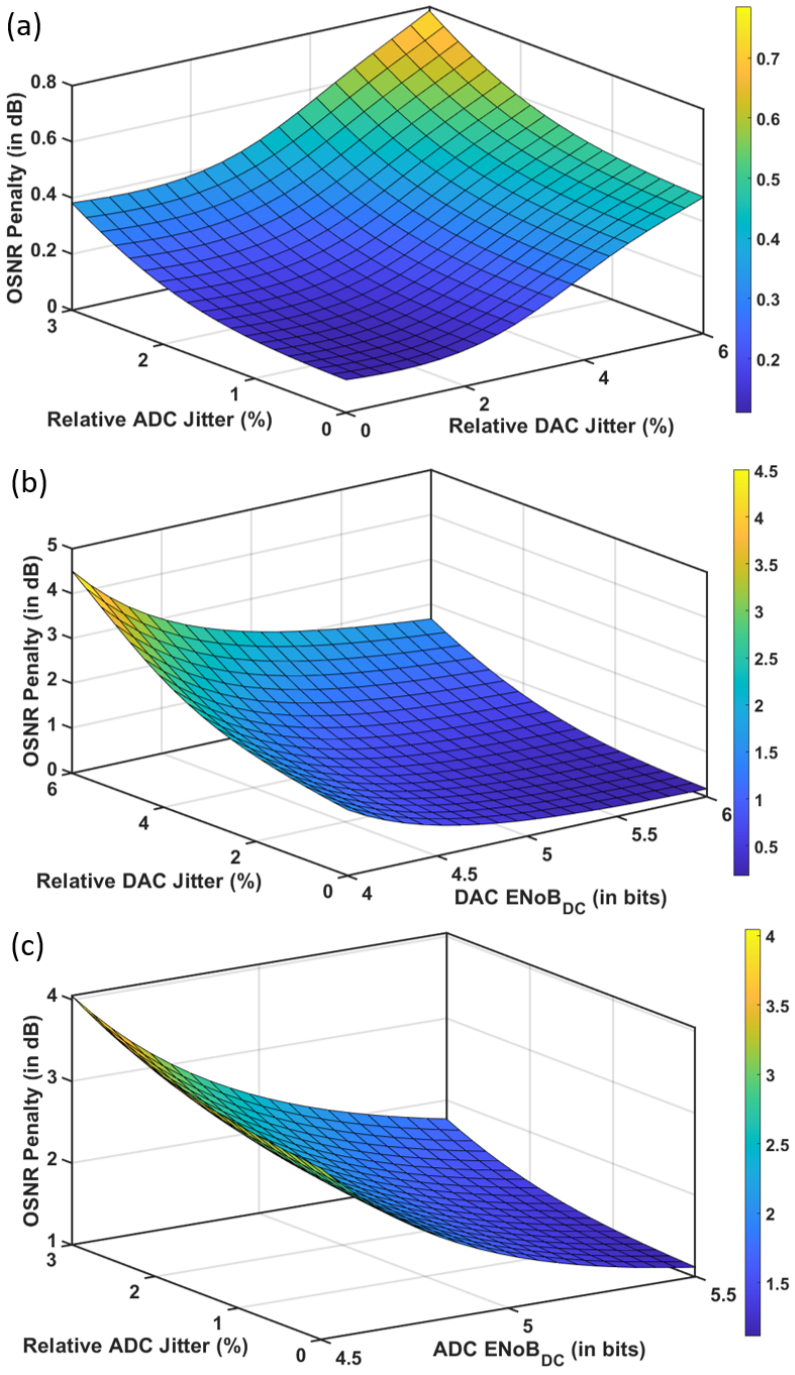

Figure 3.20: OSNR penalties for various (a) DAC and ADC relative timing jitter for 400G system, (b) DAC $EENoB_{DC}$ and DAC relative timing jitter for 600G systems, and (c) ADC $ENoB_{DC}$ and ADC relative timing jitter for 800G systems

The data was split into 70%-15%-15% randomly for training, testing and validation purposes, respectively. The mean testing error was <0.1 dB and the maximum testing error was <0.2 dB. Such a neural network model enables one to generate OSNR penalties for arbitrary EC parameters, Fig. 3.20.

Hyperbolic tangent sigmoid was used as the nonlinear transfer function and the trained NN weights are

$$G = \begin{bmatrix} 2 \\ 1 \\ 0.2314 \\ 2 \\ 0.3472 \\ 9.6 \end{bmatrix} \quad O = \begin{bmatrix} 2 \\ 1 \\ 0 \\ 2 \\ 0 \\ 1.0416 \end{bmatrix} \quad x_m = \begin{bmatrix} -1 \\ -1 \\ -1 \\ -1 \\ -1 \\ -1 \end{bmatrix} \tag{3.6}$$

$$W^{(1)} = \begin{bmatrix} 13.9143 & 0.036 & -0.037 & 0.4065 & -0.2862 & 4.4138 \\ -0.0095 & 0.9643 & -0.2412 & 0.0395 & -0.0120 & 0.0119 \\ 8.5176 & 2.0387 & 0.0446 & 0.0692 & -0.0787 & -0.0156 \\ 0.9257 & -0.0655 & 0.1361 & -0.0975 & 1.6149 & -0.0403 \\ 0.7922 & -0.2128 & 1.8638 & -0.1729 & 0.1971 & -0.0372 \\ 5.2940 & -0.0102 & 0.0116 & 0.4895 & 0.0144 & 0.0013 \\ -0.1234 & -0.0087 & 0.0202 & 0.0047 & -1.9173 & 0.0217 \\ -0.9885 & 0.0001 & -0.0075 & -0.4784 & -0.0014 & 0.0005 \\ 0.0378 & -0.2572 & 2.2386 & 0.1092 & 0.1179 & 0.0240 \\ -6.7927 & 0.0004 & -0.0034 & -2.4718 & -0.0034 & 0.0011 \end{bmatrix} \quad b^{(1)} = \begin{bmatrix} 4.3170 \\ 2.0071 \\ 3.3791 \\ -1.4323 \\ -1.2596 \\ 0.9191 \\ 0.0425 \\ -1.0981 \\ -0.1293 \\ -6.8714 \end{bmatrix}^T \tag{3.7}$$

$$W^{(2)} = \begin{bmatrix} -0.1806 \\ -5.7756 \\ -6.0456 \\ 1.2766 \\ 0.7854 \\ 10.0438 \\ -0.1754 \\ 16.6441 \\ -0.1477 \\ -73.2583 \end{bmatrix}^T \quad b^{(2)} = \begin{bmatrix} 12.512 \end{bmatrix} \tag{3.8}$$

where G is the input gain, O is the input offset and x_m is the bias which relates the input to the output of the input layer as

$$x_{out} = G \times (x_{in} - O) + x_m \tag{3.9}$$

and W and b are the weights and biases on each layer.

CHAPTER 4
ACCELERATION OF TDECQ ASSESSMENTS FOR OPTICAL TRANSMITTER QUALIFICATION

Higher order modulation formats such as PAM-4 and electronic equalization at the receiver have been implemented in direct detect optical communication systems to meet the ever increasing data rate requirements of data center networks and similar applications [150, 151]. The introduction of these technologies created the need for a new performance validation metric to demonstrate inter-vendor compatibility for optical transmitters as previous methodologies such as transmitter dispersion penalty (TDP) were too expensive [152], and transmitter and dispersion eye closure (TDEC) [153] were not compatible with PAM-4 format. TDECQ was created to overcome these limitation [112]. TDECQ has seen success in the testing of optical components, as it numerically implements a reference feed forward equalizer (FFE) which abstracts the metrics from impairments incurred through a specific receiver or benefits gained from a specific receiver equalization scheme. Owing to its success, it is now included in IEEE P802.3 Ethernet standard [154, 155] as a measurement method to qualify optical transmitters.

Even though TDECQ is a useful figure of merit for optical transmitters employing PAM-4 modulation formats, it is computationally intensive and therefore much slower to calculate than other important transmitter compliance metrics such as optical modulation amplitude (OMA) and extinction ratio (ER). Therefore, methods to accelerate the process of calculating TDECQ are needed to improve manufacturing efficiencies. ML excels at modelling overly complex physical systems and processes or streamlining calculations. Assessing TDECQ is a good application for ML as conventional method of calculating TDECQ is a complex nonlinear statistical process that is numerically demanding.

In this chapter, we demonstrate how ML techniques can be used for accelerating TDECQ

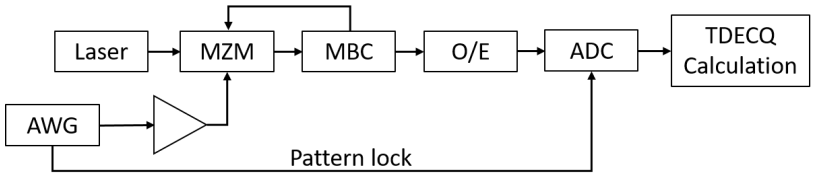

Figure 4.1: Experimental setup used to emulate various PAM-4 transmitters with various TDECQ. AWG: arbitrary waveform generator, MBC: modulator bias controller, O/E: optical to electrical converter

assessments of optical transmitter. Specifically, we present methods that can be implemented in real-time scopes, and use eye-diagram images or real-time signals.

4.1 Experimental Setup

The experimental setup was configured to emulate various PAM-4 transceivers with a plurality of TDECQ penalties for training and testing our ML algorithms, Fig. 4.1. It consists of a 1310 nm laser that is externally modulated using an EO-Space MZM whose bandwidth is 20 GHz. The modulator is biased using a Thorlabs MBX bias controller and driven by a Tektronix 70001A arbitrary waveform generator (AWG) which has an analog bandwidth of 13 GHz. The output of the AWG is amplified using an SHF 807 linear amplifier to obtain high modulation depth. The optical output of the modulator is captured by a 33 GHz Tektronix DPO7OE1 optical to electrical converter and digitized using a DPO73304D real-time oscilloscope.

The channel is digitally pre-compensated to 22 GHz to support 25 GBaud PAM-4 signaling. Additionally, a variable bandwidth gaussian filter is employed at the AWG to emulate bandwidth limitations. Dispersive effects of test fiber present in short reach direct detect systems are effectively captured using the gaussian filter [156].

The PAM-4 pattern employed here is the SSPRQ pattern which consists of the most stressful parts of a PRBS-31 pattern [154, 155]. A pattern lock is employed in our setup to ensure that the captured signal consists of the same pattern between acquisitions. Previous demonstrations in optical communication systems have shown that using known patterns

(PRBS-7, PRBS-15 etc.) to train NNs run the risk of learning the pattern instead of predicting or compensating the underlying phenomena [157]. However, when estimating TDECQ, the NN is not trying to predict the pattern but instead trying to map the nature of the distortions in the signal to a real valued scalar. Therefore, there is no risk of pattern prediction (or overfitting) in our ML implementations.

Conventional TDECQ is calculated using the methodologies described in [154, 155]. A plurality of TDECQ is obtained by varying the gaussian filter bandwidth and the MZM drive voltage to emulate linear and nonlinear limitations of PAM-4 transmitters. The captured TDECQ varied between 1.9 dB, which was the minimum achievable on the setup, and 5 dB. The explored TDECQ purposely exceeded the maximum TDECQ set by standards for satisfactory PAM-4 transmitters in order to create better ML regression models. Assessing transmitter TDECQ $>$5 dB is impractical owing to the asymptotic relation between BER and TDECQ [158], and unnecessary since transmitters with TDECQ $>$3 dB are considered unsatisfactory.

ML algorithms were implemented on a Nvidia RTX 2060 GPU with a memory of 6 GB. Accuracy of the implemented ML algorithms are reported by calculating the minimum, mean and maximum discrepancy between TDECQ assessed using conventional methods and those obtained from ML methods. We refer to the difference as discrepancy since algorithmic approaches, being statistical in nature, can itself have variations of up to 0.25 dB. Referring to the difference as error is a misnomer. Computational speeds are compared to multithreaded/multicore industry calculation speeds of 15 seconds per waveform/transmitter [159].

4.2 Eye-diagram based TDECQ Assessment

PAM-4 eye-diagrams contain significant information about the transmitters TDECQ and since CNNs specialize in processing images, they can be used on eye-diagrams to accurately assess the TDECQ in an accelerated manner. The input to our CNN is a gray-scale

PAM-4 eye diagram image. Eye-diagrams created using false colors does not provide the CNN with additional information and only increase the complexity of the CNN.

The eye-diagrams are created using one SSPRQ pattern captured from the ADC, Fig. 4.2. The signal is first upsampled to 40 samples per symbol to produce smooth eye-diagrams, Fig. 4.2(a). Then, rudimentary timing recovery is performed on the signal using simple cross-correlations to remove subsampling uncertainties from the real-time scope, Fig. 4.2(b). A two-dimensional histogram is generated using the signal with a time width of two symbol periods (=80 ps). The histogram has 160 vertical bins and 80 horizontal bins. Each bin has a grayscale depth of 256. The histogram consists of $\sim$2.6 million points. Vertical irregularities present in Fig. 4.2 are due to the resolution of the real-time scope. Output of a real-time scope has 8-bit resolution while the interpolated symbols generated in MATLAB have 32-bit resolution. We attempted to remove these image irregularities by adding sub-resolution noise to the samples in order to create smoother eye-diagram images. However, these modifications did not improve the performance of the ML method as the CNN was configured to extract macro features from the eye-diagram instead of sample-wise micro features.

The CNN employed here has 2 FELs. The first convolutional layer consists of 16 10×10 filters and the first maxpooling layer has a window size of 10×10 with a stride of 3. The second convolutional layer consists of 8 5×5 filters and the second maxpooling layer has a window size of 5×5 with a stride of 3. The nonlinear activation function used in these FELs is ReLU. All convolutional layers were initialized using the Glorot method that samples the filter weights from a uniform distribution with zero mean and a variance that is related to the number of filters and the size of the filters [160]. The output of the last FEL goes to a regression layers that maps its input to an associated TDECQ.

We captured 1000 waveforms from our experimental setup and split it to 60%, 20% and 20% for training, validating and testing purposes. Various optimization algorithms were explored, and it was found that the CNN optimized using the RMSprop technique

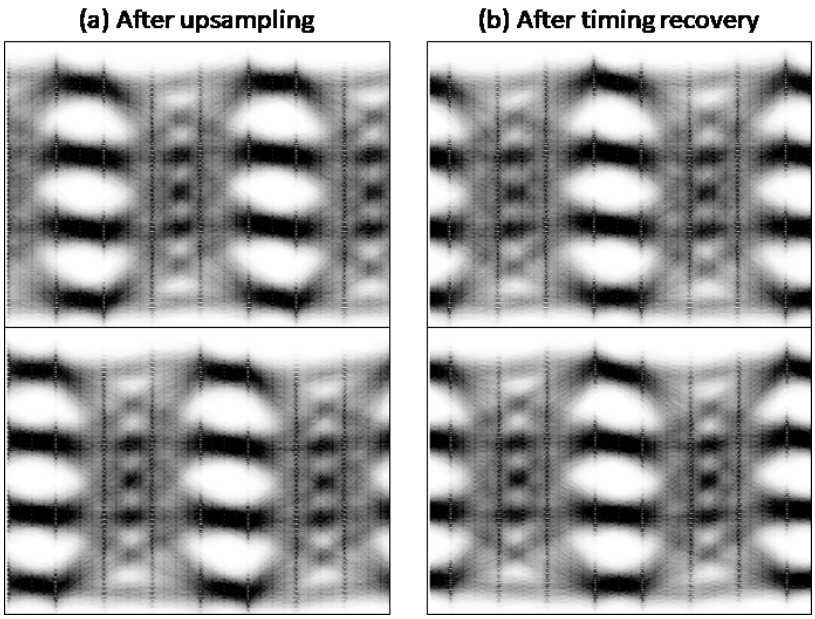

Figure 4.2: Gray-scale PAM-4 eye-diagram images constructed from the output of the real-time scope (a) after upsampling the received signal to 40 samples per symbol followed by (b) rudimentary timing recovery. Each eye-diagram consists of one SSPRQ pattern. Removing subsampling uncertainties aligns the eye-diagrams and improves the performance of the ML algorithm

provided the best performance [161]. Owing to the dimensions of the input, L2 regularizers were employed when training the CNN to restrict model complexity and prevent overfitting. Additionally, training and validation errors were carefully monitored to ensure model performance improves with subsequent epochs and the model does not overfit to the training data.

Figure 4.3 shows the TDECQ assessment accuracy using our CNN algorithm. The mean discrepancy over all explored TDECQ ranges was 0.10 dB. Additionally, for TDECQ $<$3 dB, the maximum discrepancy was 0.26 dB. Higher maximum discrepancy (0.48 dB) were obtained for TDECQ $>$3 dB. As previously mentioned, conventional TDECQ assessment algorithms demonstrate a variation of up to 0.25 dB owing to its statistical nature and therefore TDECQ measured using CNNs perform similar to conventional methods. Multiple CNNs were trained using various combinations of training, testing and validation data and every CNN was found to have comparable performance. This process demonstrates

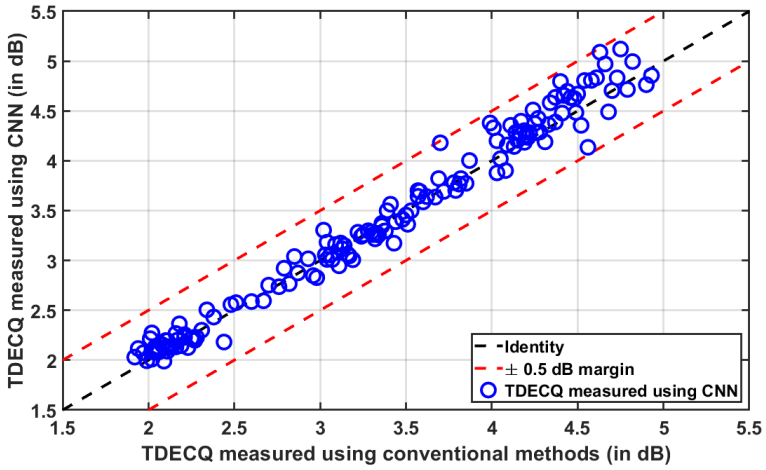

Figure 4.3: TDECQ assessment accuracies using grayscale eye-diagram image based CNN. Black dashed line is the identity and red dashed lines are the $\pm$0.5 dB margins. Assessments accuracies were within 0.5 dB for all explored TDECQ

the robustness of assessing TDECQ using grayscale eye-diagram images and CNNs.

The CNN took $\sim$100 seconds to train. Once fully trained, the CNN was able to compute TDECQ from PAM-4 eye-diagram images in $\sim$3 ms. Thus, compared to conventional industrial methodologies, CNN was able to compute TDECQ $\sim$4500 times faster per waveform/transmitter.

4.3 Real-time Signal based TDECQ Assessment

4.3.1 LSTM

While image based TDECQ assessment using CNNs proved sufficiently fast and accurate, it required the creation of eye-diagram images when computing TDECQ from real-time oscilloscopes. Therefore, we investigated strategies that use unprocessed real-time signals from real-time scopes in order to reduce processing overheads and improve efficiencies. One of the explored strategies was using LSTMs. Since long patterns (SSPRQ) are used to measure TDECQ, LSTMs should model long-term temporal information to accurately assess TDECQ.

The input to our LSTM is the raw waveform as obtained from a real-time scope without

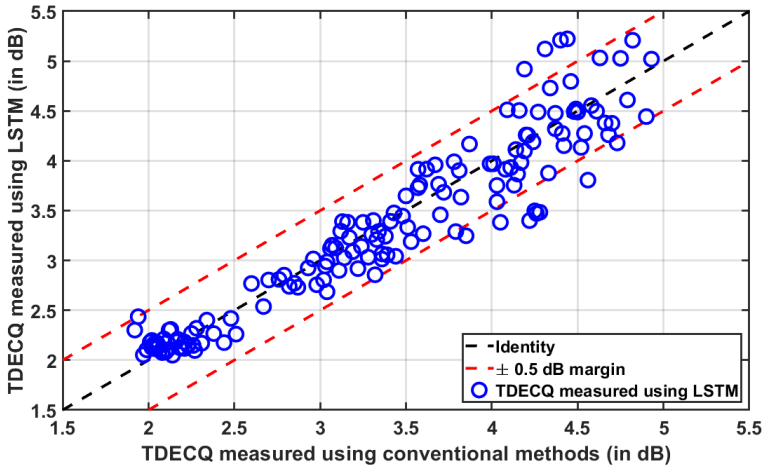

Figure 4.4: TDECQ assessment accuracies using LSTM and complete SSPRQ pattern. Performance was not as accurate as eye-diagram based CNN

any preprocessing. It consists of one SSPRQ pattern. Since the real-time scope used in the experimental setup had a sampling rate of 100 GSa/s and we employed 25 GBaud signaling rates, the length of the input was 262,140 samples. The LSTM architecture consisted of one LSTM layer with 200 hidden units which was followed by one fully connected regression layer that mapped the output of the LSTM layer to the associated TDECQ. The LSTM was optimized using the Adam optimizer [162] and trained using data obtained from our experimental setup. Once again, training and validation errors were carefully monitored to prevent overfitting.

Testing accuracies of this LSTM architecture had a mean discrepancy of 0.21 dB and a maximum discrepancy of 0.82 dB, Fig. 4.4. Various optimization algorithms and regularizers were explored to improve TDECQ assessment accuracies. However, all efforts provided similar results, and all had lower performance compared to the eye-diagram image processing approach. Additionally, the architectures took 15 hours to train. The lower performing LSTM is due to the length of the input feature and the memory of the employed GPU, which limits the number of hidden units that can be used in the LSTM layer resulting in underfitting.

In order to mitigate these performance limitations, we explored the performance of

LSTMs that use smaller input features. Specifically, we explored the accuracy of LSTM when only a portion of the SSPRQ pattern is used. This approach is based on the knowledge that specific sequences within the SSPRQ pattern are the most stressful and may therefore better reveal transmitter limitations. We refer to this architecture as truncated LSTM or tLSTM(x), where 'x' is the length of the SSPRQ segment used. Various SSPRQ segments and segment lengths were investigated, and their assessment accuracies and computation speeds were methodically studied.

The LSTM architecture consisted of one LSTM layer with 300 hidden units followed by one fully connected regression layer. Performance of tLSTMs trained using certain segments are shown in Fig. 4.5. As the segment lengths increased, TDECQ assessment accuracies increased while TDECQ computation speeds decreased. Performance of tLSTM over all explored segment lengths was marginally worse than that of eye-diagram based CNN, and computation times were tremendously slower. Regardless, tLSTMs performed much better than LSTMs employing the entire pattern in terms of assessment accuracies and computation speeds.

Performance of tLSTM strongly depended on the chosen segment, Fig. 4.6. Many parts of the SSPRQ pattern could not obtain mean discrepancies of $<$0.5 dB. In order to implement tLSTM based TDECQ assessment techniques, a careful investigation of what SSPRQ segment to use is required to obtain minimum performance discrepancies.

Training times for tLSTM varied between 5-20 minutes based on the length of the SSPRQ segment, and testing times varied between 20-300 ms per waveform/transmitter. As compared to conventional methods, TDECQ assessments were 50x-700x faster.

4.3.2 1D-CNN

Owing to the limitations of using one full SSPRQ pattern in LSTMs and the need to find the optimum SSPRQ segment for tLSTM, we also investigated the use of one-dimensional CNNs (1D-CNNs) on real-time signals. Accurate assessments of TDECQ using smaller

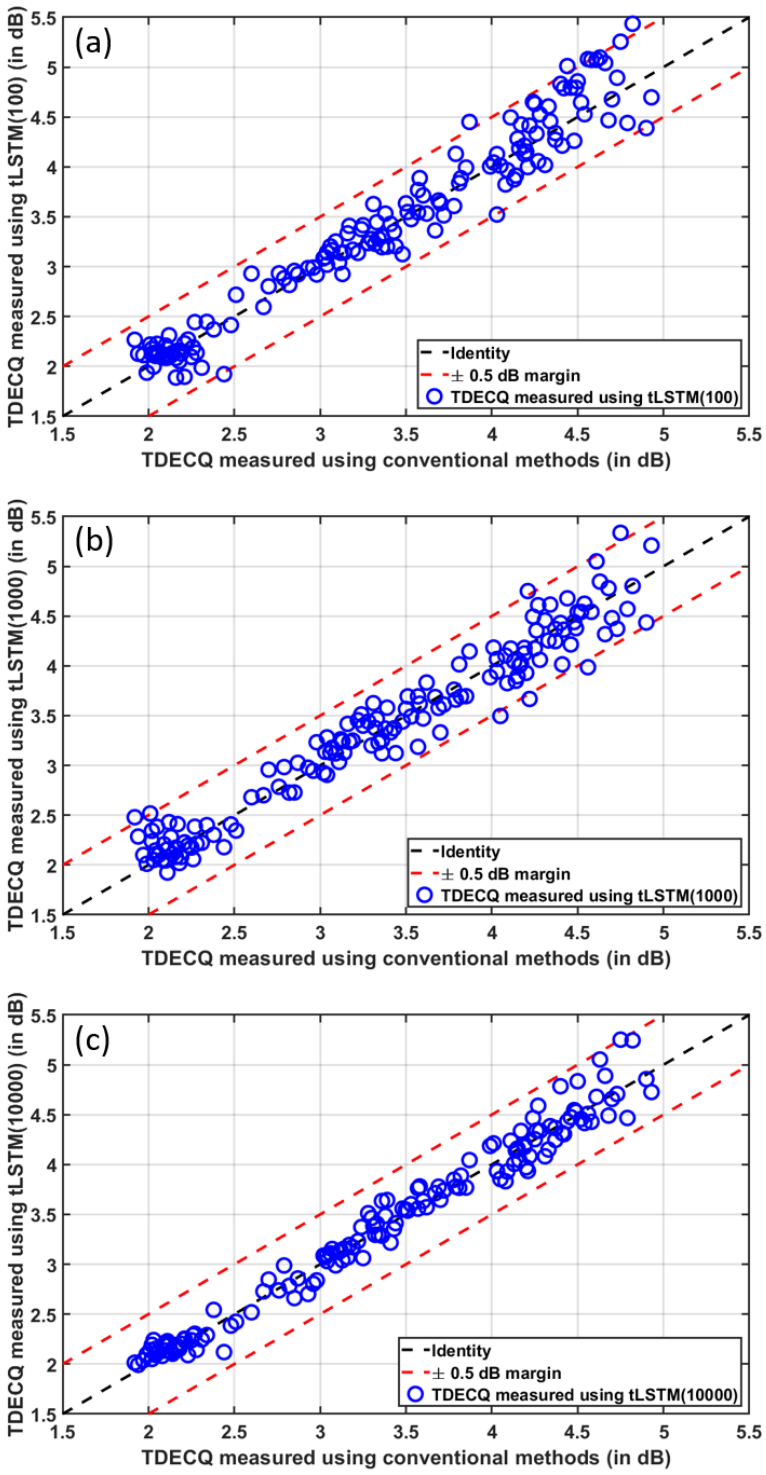

Figure 4.5: TDECQ assessment accuracies using only a portion of the SSPRQ pattern; (a) tLSTM(100), (b) tLSTM(1000), and (c) tLSTM(10000). Here, tLSTM(x) refers to an LSTM whose input is a portion of the captured SSPRQ pattern of length 'x'. As the segment length increased, assessment accuracies increased but computation speeds decreased. All tLSTM architectures performed marginally worse than eye-diagram based CNN but performed much better than LSTMs that used the entire SSPRQ pattern

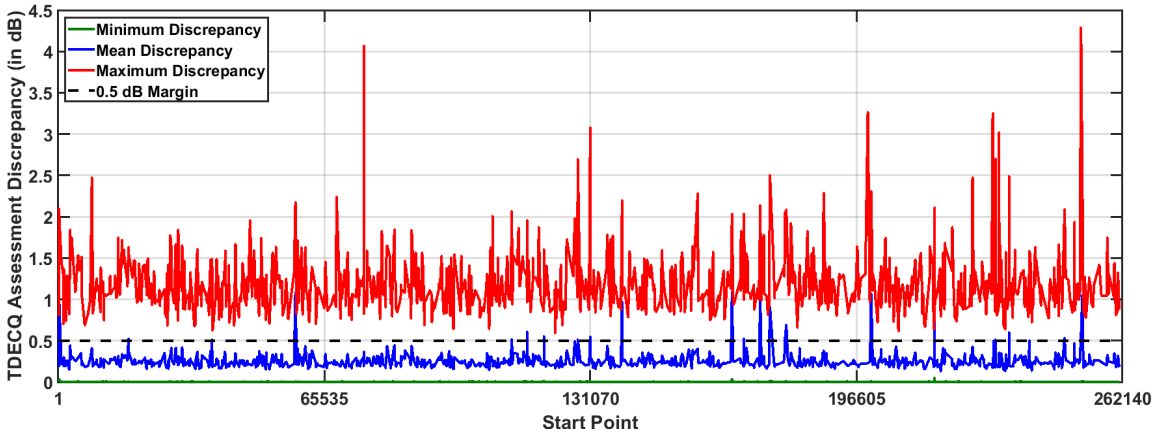

Figure 4.6: TDECQ assessment accuracies using a portion of the captured SSPRQ pattern for various starting points within the captured waveforms. The input length for the LSTM employed here is 1000. The performance strongly depends on what part of the SSPRQ pattern is used. A careful investigation of SSPRQ segments is required to employ tLSTMs and achieve high accuracies

segments of the SSPRQ pattern and LSTMs confirms that information about the transmitter's TDECQ is largely available in select places within the pattern. Since CNNs specialize in extracting features from large data in grid like topologies, they can be used to assess TDECQ from the entire SSPRQ pattern.

The input to our 1D-CNN is one SSPRQ pattern as obtained from the real-time scope without any preprocessing. As previously mentioned, it consists of 262,140 samples. The 1D-CNN consists of three FELs. In the first FEL, the convolutional layer consists of 16 filters of length 248 and the maxpooling layer has a window length of 248 with a stride of 31. The convolutional layer in the second FEL consists of 8 filters of length 64. This is followed by a maxpooling layer with a window length of 64 and stride 32. The final convolutional layer has 8 filters of length 16 and the associated maxpooling layer has a window length of 16 with a stride of 8. Similar to the eye-diagram based CNN, the nonlinear activation function used in these FELs is ReLU and all convolutional layers were initialized using the Glorot method. The output of the FELs is passed to a regression layer that maps its extracted features to the associated TDECQ. The 1D-CNN was optimized using RMSprop and appropriate L2 regularizers were employed to limit model complexity.

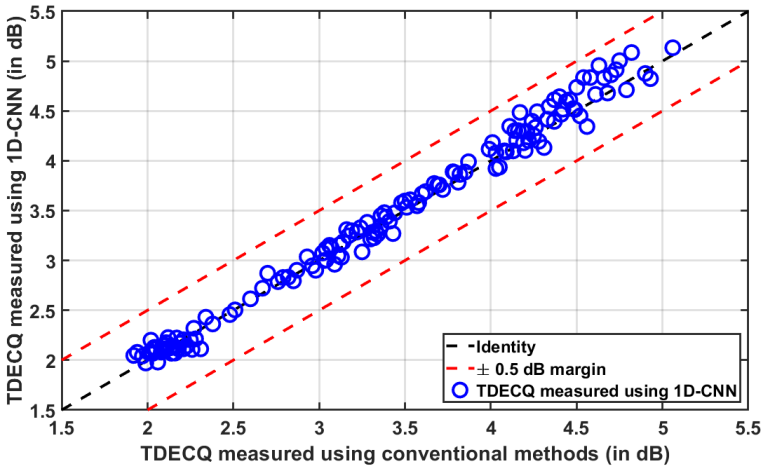

Figure 4.7: TDECQ assessment accuracies using 1D-CNN. 1D-CNN provided the best assessment accuracies over all explored ML techniques

Figure 4.7 shows the TDECQ assessment accuracy using 1D-CNN. The mean discrepancy over all explored TDECQ ranges were 0.09 dB. Additionally, the maximum discrepancy for TDECQ $<$3 dB was 0.20 dB and TDECQ $>$3 dB was 0.33 dB. Given the uncertainties in the training data due to the statistical nature of conventional TDECQ assessment algorithms, it is unlikely to observe any further improvements in assessment accuracies using ML without reducing algorithmic uncertainties first. 1D-CNN provided the best TDECQ assessment accuracies over all explored ML methods. Training times for 1D-CNN were $\sim$35 minutes and testing times were $\sim$13 ms per waveform, i.e. 1D-CNN performs $\sim$1200 times faster than conventional methods.

Table 4.1 summarizes all explored ML techniques with their training and testing times, as well as minimum, mean and maximum observed discrepancies for TDECQ $<$3dB and $>$3 dB.

4.3.3 Discussion on Computational Complexity

We investigated the computational complexity associated with both conventional methods and ML based methods in terms of the number of multiplications involved in these processes. We will ignore the number of additions and comparison here as multiplications are

Table 4.1: TDECQ assessment accuracies for various ML techniques

ML Technique	Training Time	Testing Time	Discrepancy for TDECQ <3 dB			Discrepancy for TDECQ >3 dB		
			Minimum	Mean	Maximum	Minimum	Mean	Maximum
CNN	100 seconds	3 milliseconds	0.00 dB	0.08 dB	0.26 dB	0.00 dB	0.12 dB	0.48 dB
LSTM	15 hours	5 seconds	0.00 dB	0.11 dB	0.50 dB	0.01 dB	0.27 dB	0.82 dB
tLSTM(100)	5 minutes	22 milliseconds	0.00 dB	0.12 dB	0.52 dB	0.00 dB	0.19 dB	0.62 dB
tLSTM(1000)	12 minutes	42 milliseconds	0.01 dB	0.14 dB	0.56 dB	0.00 dB	0.17 dB	0.58 dB
tLSTM(10000)	2 hours	263 milliseconds	0.00 dB	0.09 dB	0.32 dB	0.00 dB	0.12 dB	0.50 dB
1D-CNN	35 minutes	13 milliseconds	0.00 dB	0.06 dB	0.20 dB	0.00 dB	0.10 dB	0.33 dB

known to be more computationally expensive [163]. For ML based methods, we will restrict the analysis to CNNs as they proved to be superior to LSTMs in terms of performance and computation speeds. The computational complexity associated with timing recovery and Bessel filtering need not be used in the comparison. Timing recovery is implemented in the conventional method as well as in image based 2D-CNN, while waveform based 1D-CNN does not implement timing recovery (no preprocessing/raw waveforms). Fixed bandwidth Bessel filters can be implemented in the analog domain in the conventional method, while ML based methods do not require the application of Bessel filters on their inputs.

Eye-diagram image based CNN consists of two FELs. Based on the kernels used in Sec. 4.2, there are 20,480,000 (160x80x10x10x16) multiplications in the first convolutional layer, 4,665,600 (54x27x5x5x8x16) multiplications in the second convolutional layer, and 20,736 (18x9x16x8) multiplications in the fully connected layer. Therefore, the total number of multiplications involved is $\sim$25x10^6. Using a similar approach, we computed $\sim$1.1x10^9 multiplications in signal based 1D-CNN.

Conventional methods involve multiple applications of a 5-tap FFE owing to its iterative nature. Applying the FFE on one SSPRQ pattern would consist of 8,191,875 (65,535x25x5) multiplication if we assume an oversampling factor of 25. To calculate the total number of multiplications, we would need to estimate the number of iterations involved in the optimization algorithm. If we assume that it requires at least 10 iterations to find the right noise variance ($_G$), 25 iterations to find the best FFE filter weights for each iteration of noise variance, and a population size (number of FFE search initializations) of 5 to ensure global minima, the FFE is applied 1250 times. In such a scenario, the total number of multiplications are $\sim$10x10^9.

As compared to conventional methods, eye-diagram image based CNN has $\sim$400x less multiplications and signal based 1D-CNN has $\sim$10x less multiplications. Therefore, in terms of the number of multiplications, ML based methods are computationally cheaper

when assessing the TDECQ penalty. However, computation times for these methods are not just based on the number of multiplications but also on the process itself. Conventional methods are iterative and therefore time-consuming since they need to wait for the previous iteration to complete. Meanwhile, ML based methods involve fixed number of multiplications that can be executed simultaneously especially using GPUs. Therefore, ML based methods will be much faster.

CHAPTER 5
IMPAIRMENT DETECTION AND IDENTIFICATION IN OPTICAL NETWORKS

As optical networks get complex through the implementation of advanced techniques and technologies to meet the ever rising global data rate requirements, the optical network itself becomes prone to disruptions either due to signaling conditions or equipment failures. Therefore, failure management in optical networks is critical as service interruption can affect millions of users [164]. Additionally, robust failure management is necessary for optical network operators to quickly recover from failures and meet service level agreements (SLAs). However, despite its importance, today's failure management systems require human intervention and rely on rudimentary BER monitoring techniques to detect failures. Automating failure management systems is pivotal to the growth of optical networks in the future. Machine learning provides a promising direction to achieve automated optical network failure management (ONFM) systems.

From the perspective of network management, two types of failures exist in an optical network. They are hard failures and soft failures. Hard failures are those that are caused by unexpected events such as fiber cuts, electrical shutdown, broken equipment, weather effects etc. These failures are hard to predict since they are instantaneous. Soft failures are those that are caused by gradual degradation of equipment or changes in the environment. Their prompt detection, identification and localization can ensure cost-effective recovery before they translate into network disruption. Soft failures include - excessive ROADM filtering, laser drifts, growing fiber nonlinearity etc.

Recently, ML techniques have been investigated to detect soft failures in optical networks [165–170]. Methods in [165, 166, 170] employ pre-FEC BER measured over long durations (>20 minutes) for soft failure prediction, yet such durations may not be optimal

for predicting soft failures. Equipment indicators are used as input features in [169] for failure management. However, training ML for specific failures can fail to predict soft failures in general. A dual stage scheme that detects impairments using the pre-FEC BER and received optical power [167], and along with the optical spectra employs a semi-supervised SVM scheme to identify the impairment was also investigated. However, this technique can only identify impairments that directly affect the optical spectra. While [168] employs techniques to predict general soft failures, they do so by employing NNs with multiple hidden nodes. NNs are not always desirable since they consume notable energy, are associated with non-trivial parameter optimization, and require large data sets to train and induce undesired latency.

In this chapter, we develop simple and robust ML techniques that can be used to predict/detect and identify link failures in optical networks by exploiting metrics that are readily available in the DCR.

5.1 Experimental Testbed

We use a 3-channel 32 GBaud DP-QPSK link to validate our failure identification techniques, Fig. 5.1. It consists of an ECL operating at 1550.918 nm. The laser is modulated with DP-QPSK symbols using an MZM modulator. The QPSK signal is created using an M8196A Keysight AWG. The output of the AWG is amplified using an Inphi 4514 driver before passing it to the modulator to obtain sufficient modulation depth. The output of the modulator is passed to a Coherent Solution automatic bias controller (IQ-ABC) to stabilize the bias point in the modulator. This modulated optical signal forms the main channel.

Using similar methodologies employed in creating the main channel, we create two side channels spaced 37.5 GHz apart from the main channel on either sides. All the channels are combined using a 3-dB coupler and passed to an EDFA for pre-amplification. The 3-channel optical signal is passed to a recirculating loop to emulate fiber propagation. The launch power (LP) into the fiber is fixed at 0 dBm. Each loop consists of three 90 km

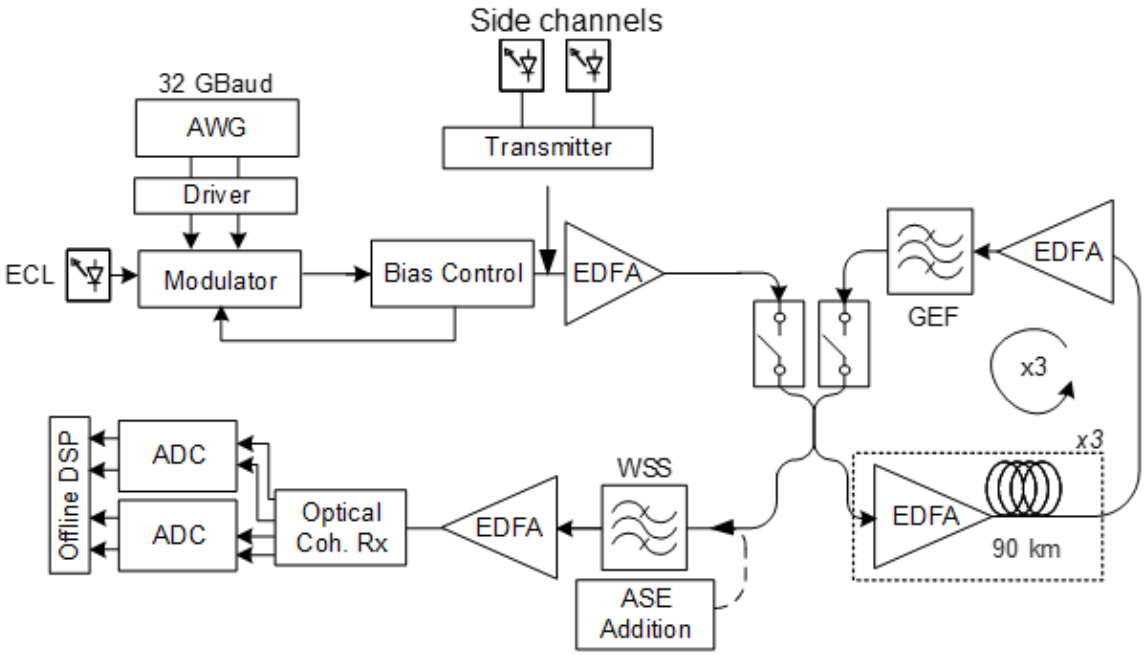

Figure 5.1: Experimental setup employing 3 channels at 32 GBaud DP-QPSK

spans of SSMF with EDFAs to compensate for propagation losses. The loop recirculates the signal three times providing an effective transport distance of 810 km. ASE noise is added to the output of the loop to vary the OSNR of the signal as required. The OSNR is initially set to 14 dB corresponding to a BER of 10^{-3}.

The noise loaded signal is filtered using a WSS to carve out the main channel. The WSS bandwidth is 37.5 GHz and is centered around 1550.918 nm. Finally, the signal is received by a coherent receiver and its output is passed to a pair of Keysight DSA93004L ADC for digitization. The digitized signal is processed using conventional receiver DSP to obtain the signal's BER.

5.2 Failing ROADM Identification

Failing ROADMs introduce undesired filtering effects in an optical link. As previously mentioned, these effects include excessive filtering, and passband offsets from the source laser carrier frequency. If left unmanaged, they can eventually lead to link failures. Two-class SVMs can be used to identify such degradations in an optical link.

In order to emulate the effects of failing ROADMs in an optical network, we vary the bandwidth of the WSS in our experimental testbed from 10 GHz to 37.5 GHz and vary the transmitter laser's operating frequency with respect to the center frequency of the WSS between -5 GHz and 5 GHz. Here, we classify a ROADM bandwidth of less than 32 GHz or a frequency offset greater than $\pm$1.5 GHz as excess filtering and a cause for concern.

The input feature vector to the SVM is the power spectral density (PSD) of the received electrical signal. A 64-point FFT is used to derive the PSD. Since PSDs are used for classification, this method can be implemented along with the receiver DSP where FFTs are frequently taken for CD compensation. The PSD of all the signals captured over various WSS bandwidths and frequency offset is used as the data set over which the SVM is trained and tested. The data is randomly divided into 10 equal sets. Nine of these sets are used to train the SVM, and the last set is used to test the SVM. A 10-fold cross-validation is then performed by changing the training and testing data sets.

Different types of kernels are implemented in the SVM classifier, Fig. 5.2. These include linear, quadratic, cubic and RBF. The box constraint, which is a measure of the slack in the optimization process, is also varied between 10^{-3} and 10^{6} to see the performance of the classifier under different constraints. For appropriately chosen box constraints, three kernels were able to provide classification accuracies of $>$99%. Such high accuracies suggest that good performance can be achieved with a reduced input feature size and commensurate reduction in the complexity of the classifier. PCA was used to reduce the number of features in the input vector. Upon analyzing the principal component variances, Fig. 5.3, one highly significant component and three moderately significant components were identified in the input PSD.

Figure 5.4(a) shows the performance of the SVM classifier using one principal component (identified separately as being strongly related to the filtered signal's spectral width). As can be seen, the error rate was always $>$18% demonstrating that one component (or simply tracking the passband signal's bandwidth) is insufficient to achieve good classifi-

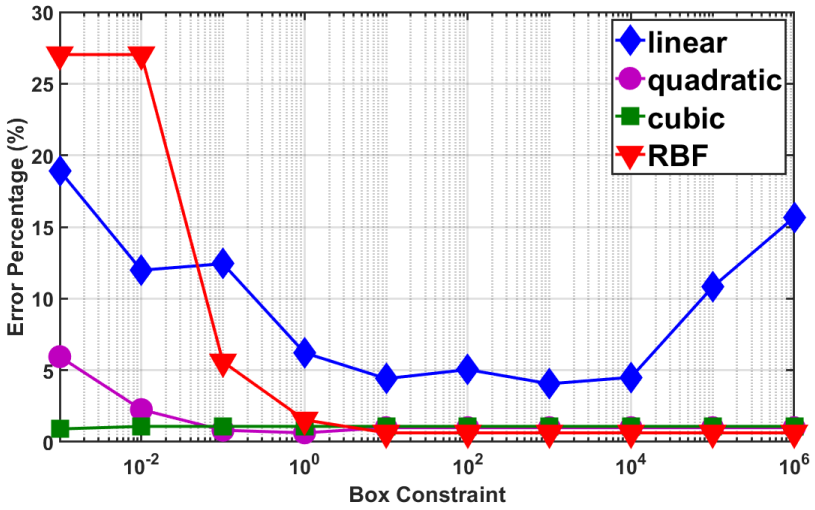

Figure 5.2: Prediction error rate for various types of kernels and box constraints

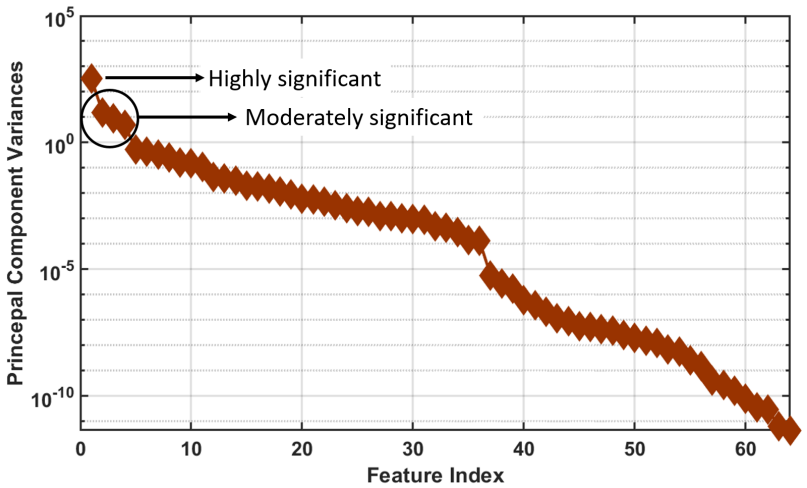

Figure 5.3: Principal component variances for the input feature vector. One highly significant component and three moderately significant components were identified in the principal component variances of the signal's PSD

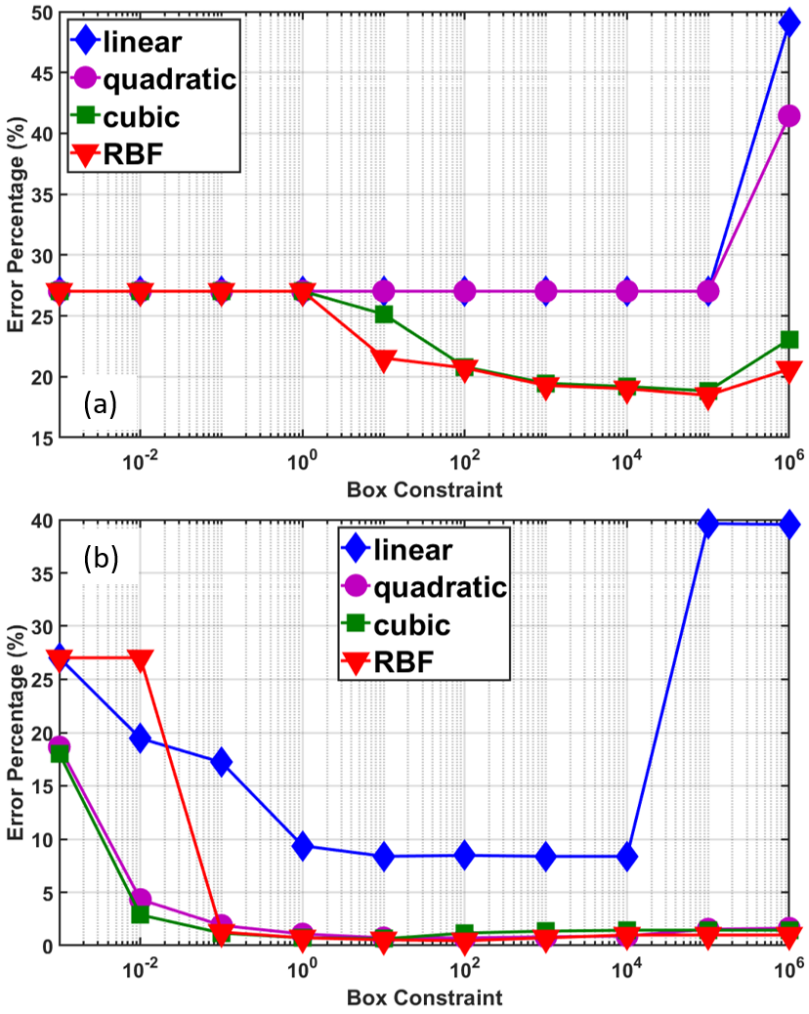

Figure 5.4: Prediction error rate with (a) one principal component and (b) four principal components for various kernels and box constraints

cation accuracy. However, with four principal components the classification accuracy was >99% for multiple kernels over a wide range of box constraints, Figure 5.4(b). Thus, four components are sufficient to identify signals subject to undesired ROADM filtering.

Once trained, it is straightforward to track PSDs with undesired filtering and hence to predict imminent failures. The technique can also be easily implemented in the receiver DSP and link can be monitored at user defined intervals.

5.3 One-class SVM based Anomaly Detection

One of the major challenges in implementing ML techniques in optical communication systems arises from the inability to collect enough data with soft failures. Optical networks are sufficiently robust by design and link failures are extremely rare. Therefore, supervised learning techniques, such as the SVM technique described previously, would require artificially created abnormalities to train the system which may not always be possible. Unsupervised anomaly detection techniques can be used to overcome this limitation since it only requires one type of data to train. In case of optical systems, this would be data taken during normal operations. Limited amount of naturally available data affected by soft failures can then be used to test the trained model. We investigate the use of one-class SVMs in identifying/predicting abnormalities in optical networks.

The input feature for the technique is the absolute value of the N-centermost adaptive filter coefficients (AFC) obtained from the DCR. In a standard optical transceiver demodulation scheme, this adaptive filter is employed at the end of the receiver DSP to compensate for any residual link impairments. We vary N to study the performance of this technique. The SVM is trained using multiple AFCs obtained under normal operation from the experimental testbed, Fig. 5.1. The technique is tested with data obtained by manually introducing the following abnormalities into the system

- Inter-channel interference: introduced by reducing the channel spacing between the main channel and the adjacent channel. It was varied between 25 GHz and 33 GHz.
- Malfunctioning laser: the main channel laser was substituted with a high linewidth ($<$1 MHz) unstable laser to emulate this abnormality.
- OSNR degradation: added ASE noise was increased to degrade the OSNR and vary it between 10 and 12 dB.
- ROADM impairments: introduced by reducing the bandwidth of the WSS, or detun-

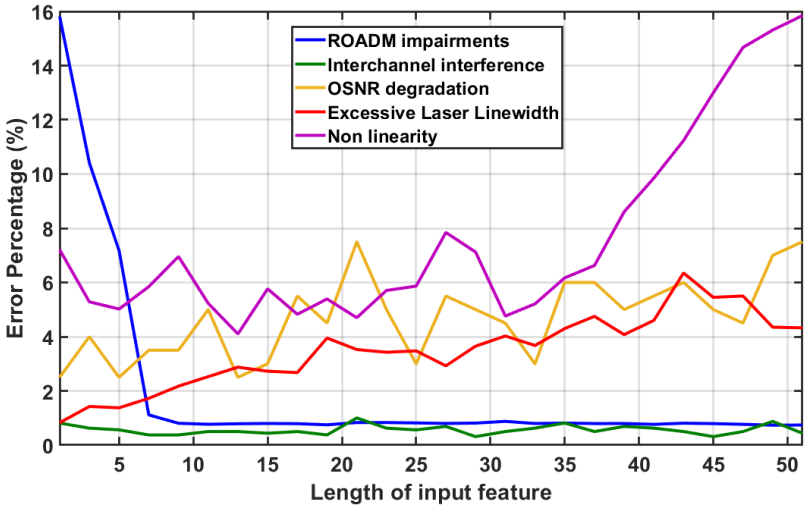

Figure 5.5: Performance of one-class SVM in the presence of various impairments. Few features are not sufficient to obtain good performance rates and large feature lengths are prone to overfitting

ing the WSS center frequency with respect to the main channel's center frequency. The bandwidth was varied between 14 GHz and 36 GHz and the detuning frequency was varied between 1.5 GHz and 5 GHz.

- Fiber nonlinearity: introduced by increasing the input LP into the recirculating loop. It is varied between 6 and 9 dBm.

Figure 5.5 shows the performance of one-class SVM in the presence of various abnormalities as a function of N. In case of ROADM abnormalities, low feature lengths are not sufficient to obtain good performance. Most of these errors arise from data affected by ROADMs operating at bandwidths close to the symbol rate (32 GBaud), Fig. 5.6. As expected, it is much harder to identify an anomaly if it is operating very close to normal conditions. In some cases, such as those arising from malfunctioning lasers, OSNR degradation and fiber nonlinearity, higher feature lengths induce higher error rates due to overfitting. Overall, for optimally chosen feature length (= 13), the error rates were $<5\%$.

When employing any unsupervised technique, one is interested in investigating the false positive and false negative rates. In our case, most of the classification errors were due to false positives, Table 5.1. This suggests that under normal operation, filter weights are well

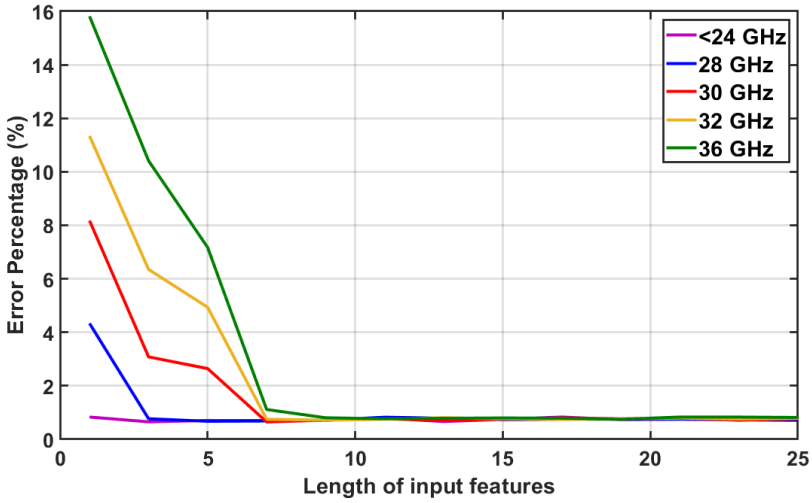

Figure 5.6: Performance of one-class SVM for various WSS bandwidths. Detection accuracies increase for lower filter lengths as the operating bandwidth goes further away from the operating symbol rate (32 GBaud)

Table 5.1: False positive and false negative rates for one-class SVM employing 13 center most filter weights

Abnormality	False positive rate	False negative rate
ROADM	0.7 %	0.4%
Interchannel Interference	0.6 %	0.05 %
OSNR degradation	2.5 %	1 %
Laser malfunction	1.7 %	0.1 %
Fiber nonlinearity	3.9 %	0.1 %

behaved and a good choice for input features.

Whenever sufficient abnormal data is available, this technique can be supplemented with impairment identification schemes to further automate OFNM systems. We investigated the use of two-class SVM for impairment identification and observed that for optimally chosen feature lengths, identification accuracies as high as 97% can be achieved, Fig. 5.7. Similar to the detection scheme, the identification scheme was also prone to underfitting and overfitting for low and high input feature lengths respectively.

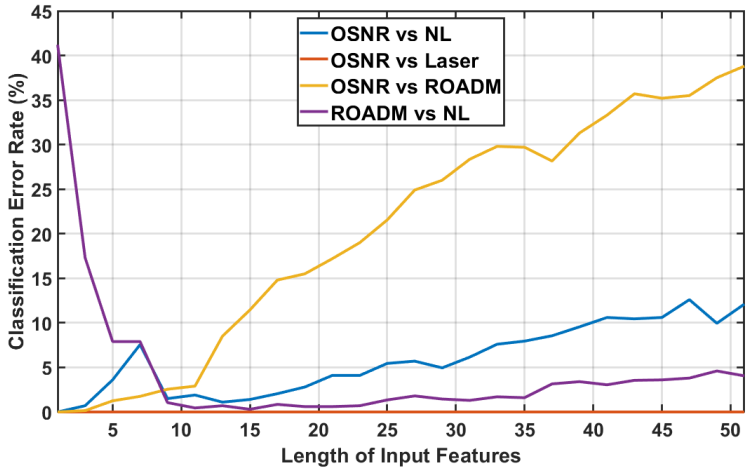

Figure 5.7: Identification performance of two-class SVM for various impairments, identified two at a time. For optimally chosen feature lengths, the classification errors can be as low as $<3\%$

5.4 Autoencoder based Failure Detection and Identification

While one-class SVM was able to detect/predict link failures, the accuracy was poor for certain impairments and the performance strongly depended on the number of AFCs used. Additionally, the framework did not provision for a robust impairment identification scheme. In order to circumvent these limitations, we investigate the use of autoencoders for simultaneous impairment detection/prediction and identification in optical networks.

The methodology consists of two steps - impairment prediction/detection based on autoencoders and impairment identification based on a feed forward NN, Fig. 5.8. The input to the autoencoder are the absolute values of all AFCs from the DCR. Unlike the previous method, there is no need to choose the number of AFCs in this methodology. The autoencoder is trained on multiple AFCs obtained from our experimental setup, Fig. 5.1. The input size is 182 and the code size is fixed to 10. Other code sizes were explored, but 10 provided the optimum trade-off between code size and performance.

Note that perfect reconstruction can never be achieved from an autoencoder scheme in an optical link as the AFCs vary slightly between acquisitions due to noise and there is loss

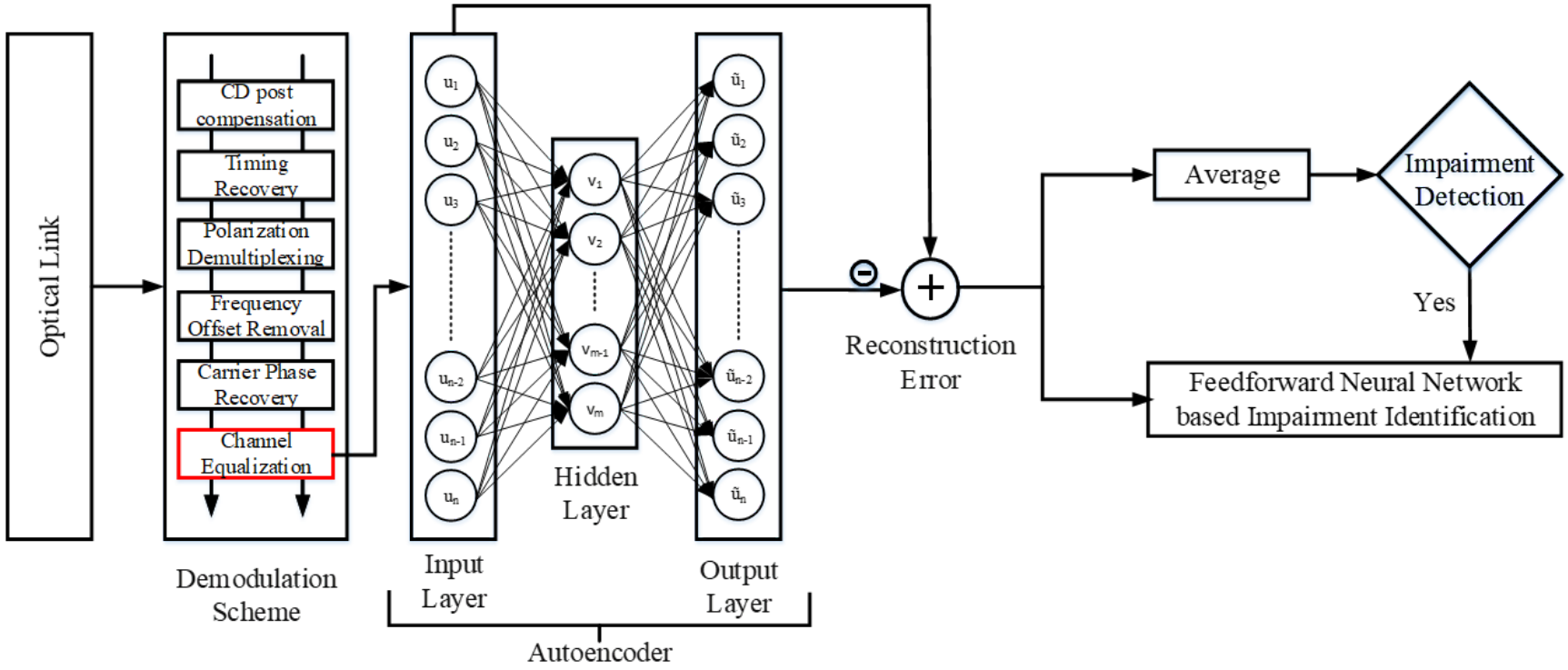

Figure 5.8: Two step impairment detection and identification scheme based on autoencoders. The input to the autoencoder are the AFCs from the DCR. The mean reconstruction error (MRE) from the autoencoder is used to detect impairments. If detected, the reconstruction errors are sent to a feed-forward NN to identify the cause of the impairment

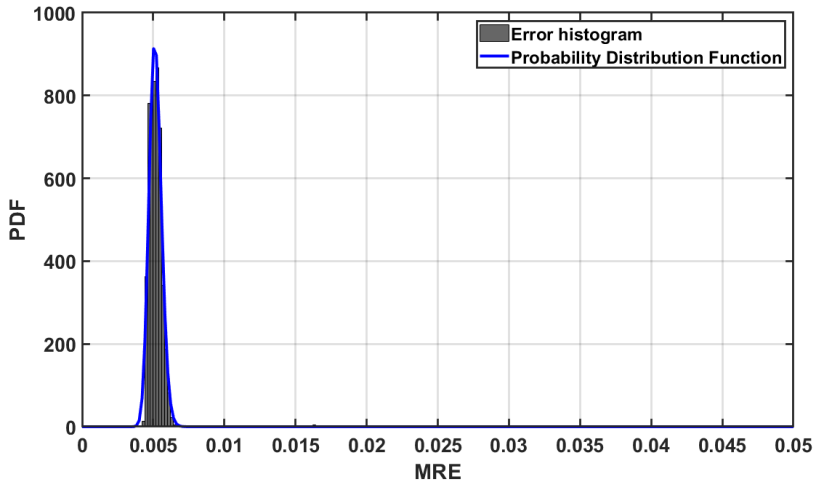

Figure 5.9: Distribution of the MRE under normal operation. The log-normal distribution used to fit the MRE under normal operation is represented in blue

of information based on the size of the code. Therefore, even under normal operation, the reconstruction error will conform to a probability distribution with appropriate attributes. Once fully trained, we compute the mean reconstruction error (MRE) for the AFCs under normal operation and fit it to a probability distribution function (PDF), Fig. 5.9. A log-normal distribution was chosen to fit the reconstruction error distribution.

In the event of an impairment, the adaptive filters will react to the impairment to reduce its effect on the signal resulting in a different set of AFCs. Since these AFCs are not representative of the AFCs under normal operation, the reconstruction error from the autoencoders will be large and the MRE would lie in the tail of the PDF, Fig. 5.10. By appropriately defining this region, we can detect any impairment affecting an optical link. Here, we set this region to occupy 10% of the total tail probability.

In order to measure the detection accuracy of the autoencoder technique, we test it on data obtained by manually introducing the following changes into the system

- Inter-channel interference: introduced by reducing the channel spacing between the main channel and the adjacent channel. It was varied between 15 GHz and 35 GHz.
- OSNR degradation: added ASE noise was increased to degrade the OSNR and vary it between 7 and 14 dB.

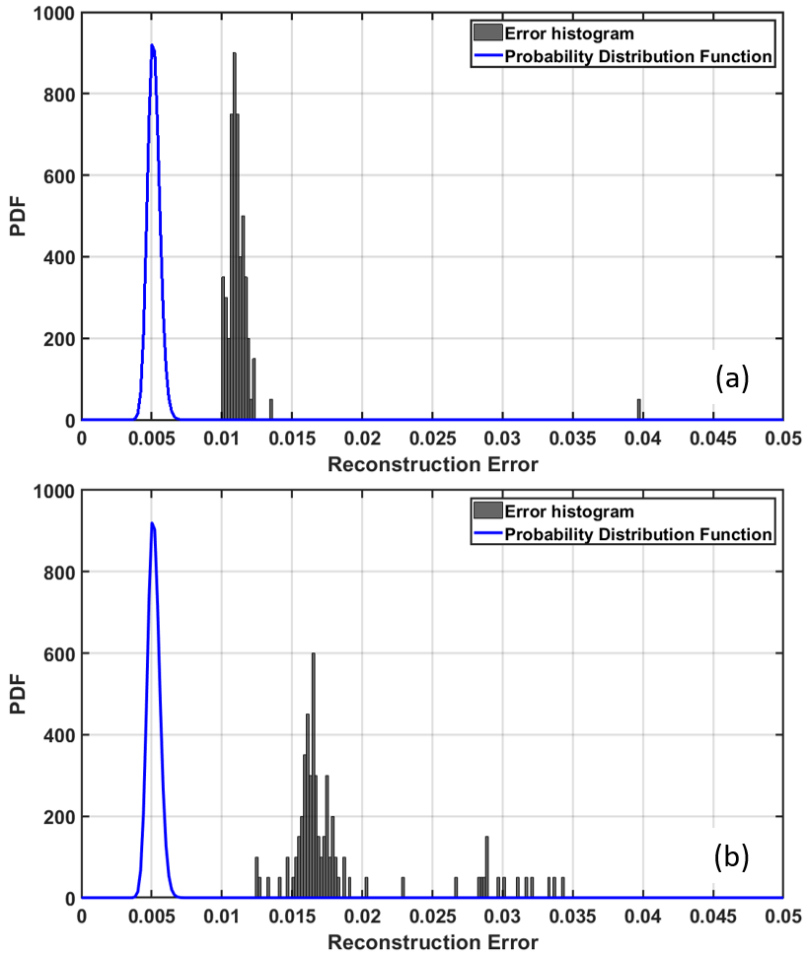

Figure 5.10: Distribution of the MRE under (a) link LP = 9 dBm and (b) WSS bandwidth = 24 GHz

- ROADM impairments: introduced by reducing the bandwidth of the WSS. The bandwidth was varied between 20 GHz and 36 GHz.
- Fiber nonlinearity: introduced by increasing the input LP into the recirculating loop. It is varied between 3 and 10 dBm.

We considered the following thresholds as impairments: Interchannel spacing $<$30 GHz, LP $>$6 dBm, ROADM filter bandwidth $<$30 GHz and OSNR $<$11 dB. The thresholds were chosen based on the experimental setup and the associated signaling rate. Thresholds need to be appropriately modified for other links.

Figure 5.11 shows the performance of the impairment detection scheme for various impairments. The red curves show the evolution of pre-FEC BERs as a function of various impairment parameters and the blue stems show the schemes detection accuracy. For the thresholds described above, the scheme is able to detect impairments with near 100% accuracy well before the pre-FEC BER hits the SD-FEC limit at 2.2×10^{-2}. While the technique is demonstrated for 4 impairments here, one can argue that the AFCs should be susceptible to any link abnormalities. Therefore, this technique can be extended to predict/detect any other impairment such as MPI or PDL.

When an impairment is detected, the reconstruction error is sent to a simple NN to identify the cause of the impairment, Fig. 5.12. The NN consists of 1 hidden layer with 10 hidden neurons. The output is one of the four impairments described above, namely, inter-channel interference, OSNR degradation, ROADM filter induced penalties or fiber nonlinearities. Note that this stage is only possible if soft failure data representing these impairments are present. Therefore, we are limited to the four impairments we could emulate in the experimental setup.

Table 5.2 shows the confusion matrix for the impairment identification scheme. The network is able to identify impairments arising from ROADM filters, OSNR degradation and interchannel interference with 100% accuracy; however, there is a small error ($<$1%) when detecting impairments arising from fiber nonlinearity. These impairments tend to

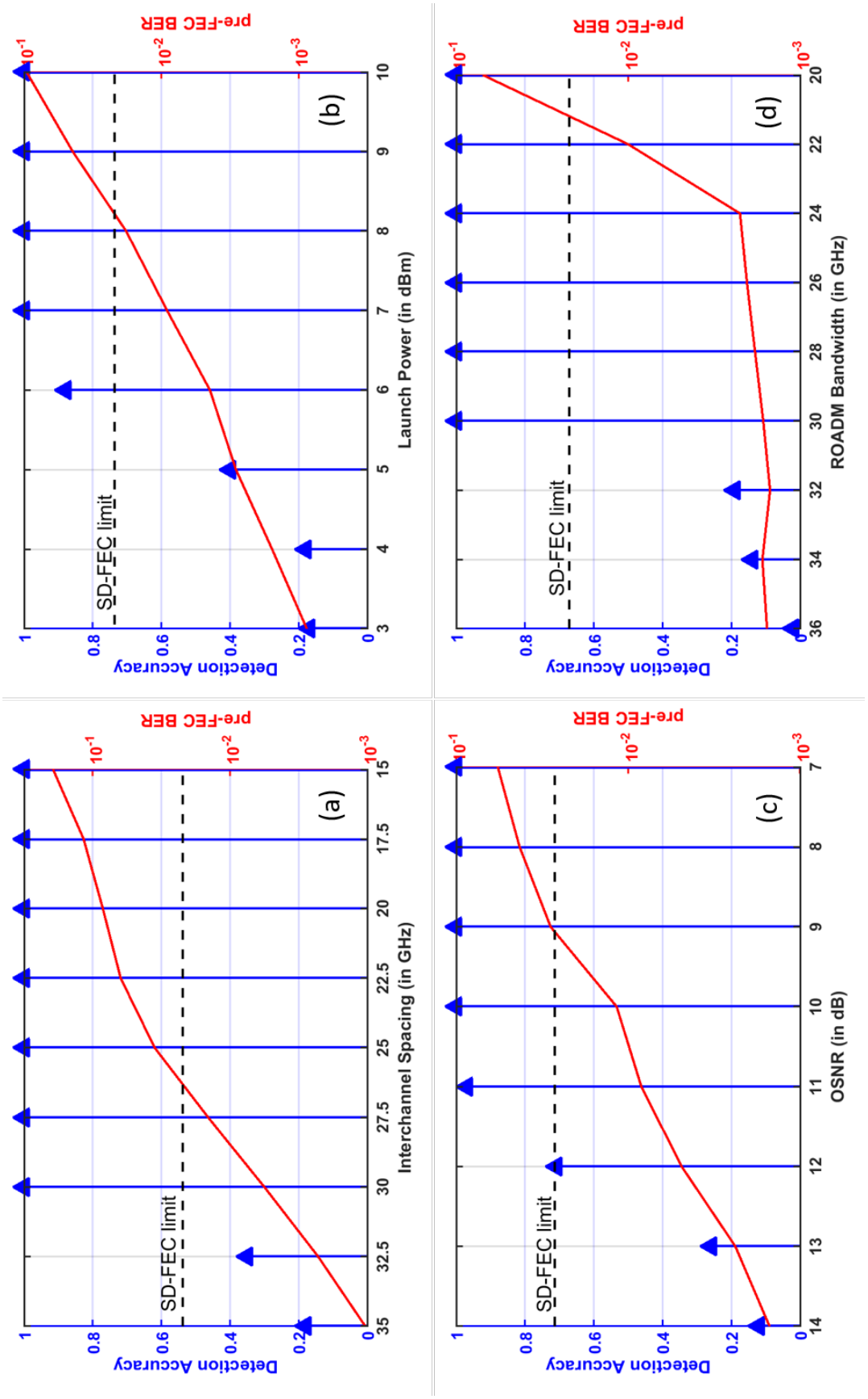

Figure 5.11: Performance of the impairment detection scheme along with the pre-FEC BER in the presence of impairments caused by (a) interchannel interference, (b) fiber Nonlinearity, (c) ROADM filters and (d) OSNR degradation respectively

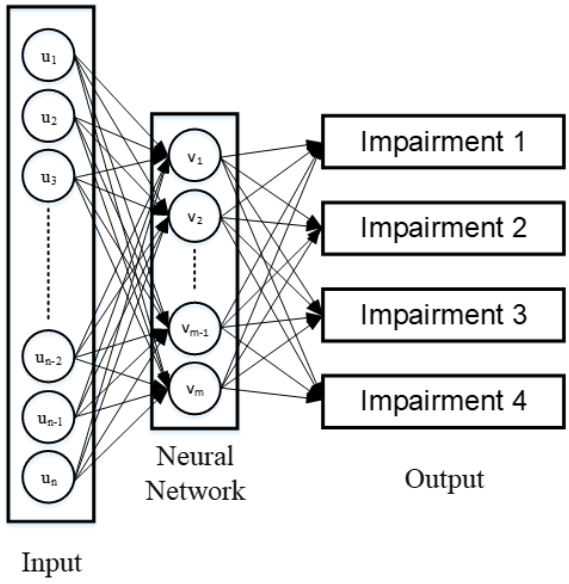

Figure 5.12: Feed forward NN scheme to identify the detected impairment. It consist of one hidden layer with 10 neurons. The NN input is the reconstruction error from the autoencoders and the output is the impairment label

Table 5.2: Confusion matrix of the feed forward NN used to identify impairments. Class 1 - Fiber nonlinearity, 2 - ROADM filter anomalies, 3 - OSNR degradation and 4 - Interchannel interference

Output	1	20.3 %	0 %	0 %	0 %	100 %
	2	0 %	22.7 %	0 %	0 %	100 %
	3	0.2 %	0 %	22.7 %	0 %	99.3 %
	4	0 %	0 %	0 %	34.1 %	100 %
		99.3 %	100 %	100 %	100 %	99.8%
		1	2	3	4	
		Target				

Table 5.3: Performance of the NN based identification scheme in the presence of multiple impairments

# actual	# Identified	Identification Accuracy
1	1	99.8 %
2	1	98.3 %
2	2	73.6 %

be misclassified as OSNR degradation possibly because these two impairments manifest similarly for QPSK signals [171].

Using the soft outputs from the neural network, we were also able to identify link impairments when multiple impairments were present in the link, Table 5.3. In the presence of two impairments, the scheme is able to identify at least one of the impairments with $>98\%$ accuracy and both impairments simultaneously with $>70\%$ accuracy. While the performance of identifying multiple impairments simultaneously is poor, the method is able to identify at least one impairment with high accuracy. Therefore, if the impairments are resolved sequentially, both impairments can be identified effectively.

CHAPTER 6
CONCLUSIONS

In order to meet the growing data rate requirements, optical communication systems are expected to get larger and faster in the coming years. However, many challenges lie ahead for these systems to meet such expectations. The dissertation began by identifying the limitations that ECs would introduce in future optical links which are expected to employ high symbol rates and higher modulation formats. We identified the primary phenomena that introduce frequency dependent ENoB in wideband ECs and developed novel models that can simulate these effects in an optical simulation environment. These phenomena include quantization, timing jitter, bandwidth limitations and noise. The models were theoretically validated and were experimentally found to capture frequency dependent ENoB such as those exhibited by commercial ECs accurately. Special considerations were made when developing the models to ensure that the models are computationally efficient. These include the modified methodology used to add timing jitter and to include DNL and INL. We then used these models to estimate the OSNR penalties from ECs for 400G, 600G and 800G systems that are expected to be deployed in the coming future. It was found that ECs introduce significant penalties that need to be accounted for when planning system deployments. Finally, we demonstrated how ML techniques can be used to circumvent tedious and time-consuming simulations when estimating OSNR penalties from ECs for commonly deployed link configurations.

Modern optical communication systems multiplex and demultiplex multiple ECs to achieve high symbol rates. Such architectures can introduce significant clock spurs that can degrade system performance. Additionally, modern ECs employ amplifiers that can introduce nonlinearities in the signal and deteriorate signal quality. Future research efforts can investigate how to include the effects of clock spurs and nonlinearities in a computationally

efficient manner into these models. Moreover, in this research, it was found that optical communication systems require higher conversion resolutions at the ADC when compared to the DAC, demonstrating the relationship between ADCs and the receiver DSP's efficiency on compensating impairments. These effects need to be further investigated and quantified in order to fully understand the effects of wideband ECs in optical communication systems.

In chapter 4, we introduced TDECQ and its role in qualifying optical transmitters. While TDECQ is a robust and repeatable methodology, it is computationally expensive and time consuming. We demonstrated how ML techniques can be used to accelerate TDECQ assessments while maintaining accuracies comparable to conventional methods. Specifically, we demonstrated eye-diagram image based CNN techniques , and real-time signal based LSTM and 1D-CNN techniques. All demonstrated ML methodologies were at least 500 times faster than conventional methods with CNNs demonstrating computation speed improvements of a factor of $\sim$4500. Maximum assessment discrepancies were $<$0.6 dB for investigated cases.

While exploring LSTM based TDECQ assessments, it was observed that the performance of LSTM greatly varied based on what segment of the SSPRQ pattern was utilized. This demonstrates that certain parts of the SSPRQ pattern hold more information about the transmitter's TDECQ than certain other parts. An extensive investigation is required to understand how different parts of the SSPRQ pattern stress the optical transmitter and conclude if it is possible to shorten the testing pattern to improve computation speeds. It is likely that such an investigation could result in the finding of a significantly shorter test pattern which along with ML can reduce acquisition times and assess TDECQ near-instantaneously. Additionally, future work can also investigate the use of ML techniques to identify the cause of unsatisfactory TDECQ in optical transmitters, so as to accelerate repair procedures and troubleshooting efficiencies.

With the imminent growth of optical networks, it is important to improve current OFNM

systems to reduce link downtime and meet SLAs. In chapter 5, we demonstrated ML techniques that can be used to implement automated OFNM systems which can predict/detect impairments as well as identify them. Our detection techniques were based on unsupervised learning algorithms since faulty data of all types may not always be available to implement supervised learning techniques in OFNM systems. The techniques were able to detect impairments with high accuracies using readily-available DSP features demonstrating the robustness and practicality of our method. Additionally, we demonstrated how the investigated detection schemes could be easily extended to implement impairment identification schemes when sufficient faulty data is available. The impairment identification scheme presented in this dissertation was able to detect multiple impairments with $>98\%$ accuracy if carefully handled.

Future work on OFNM systems can investigate how these presented techniques can be extended to implement impairment localization schemes which can tremendously improve system repair times. Furthermore, the use of ML techniques to optimize network capacities, maximize network margins and estimate link performance metrics can also be explored.

Appendices

APPENDIX A

THEORETICAL DERIVATION OF FREQUENCY DEPENDENT ENOB

Procedures for measuring the ENoB of a DAC is described in [75]. It requires transmitting sinusoids at individual frequencies, calculating the corresponding SINAD and then computing the ENoB using Eqn. 2.43. Similarly, the procedures for an ADC is described in [147] and requires receiving sinusoids at individual frequencies.

Equation 2.43 is derived as follows. Let us assume that each quantization level is uniformly spaced and has one unit amplitude. Then, any sinusoid at frequency f occupying full scale is given by,

$$x(t) = \frac{2^N}{2} \sin(2\pi f t) \tag{A.1}$$

where N is the hardware bit architecture. The RMS of $x(t)$ is given by $\frac{2^N}{2\sqrt{2}}$. If we assume that the conversion error due to quantization is white and uniformly distributed, its variance is given by

$$\sigma_q^2 = \frac{1}{12} \tag{A.2}$$

This is a very broad assumption and requires the converted signal to be essentially random, which is not true for sinusoids at individual frequencies. The SINAD of such a signal is then given by,

$$SINAD = \frac{P_{signal}}{P_{noise}} = \frac{2^{2N}/8}{1/12} \tag{A.3}$$

Taking the logarithm (base 2) on either side give us,

$$N = 0.5 \times \log_2(SINAD) - 0.5 \times \log_2(1.5) \tag{A.4}$$

If any other impairment is present, it is included in the SINAD and N is substituted with the effective number of bits or ENoB [75, 147].

In order to derive frequency dependent ENoB for ECs, we will first compute the modified SINAD by computing the statistics of various impairments. Using the assumption that timing jitter introduced by EC clocks is much lesser than its sampling period, the relation between timing jitter, the derivative of the analog signal being converted, and an equivalent amplitude jitter is given by

$$\Delta X = \frac{dx(t)}{dt}\Delta T \tag{A.5}$$

If we use the previous assumption that the added noise is white and independent of the signal, the equivalent amplitude jitter's variance is given by

$$\sigma_{aj}^2 = \sigma_{tj}^2 \left(RMS\left[\frac{dx(t)}{dt}\right]\right)^2 \tag{A.6}$$

$$= \sigma_{tj}^2 2^{2N-1}\pi^2 f^2 \tag{A.7}$$

where σ_{tj}^2 is the variance of the timing jitter.

In order to include the effects of DNL and INL, we assume that the error due to non-uniform resolution level is uniformly distributed. In such a case, the total quantization error forms a triangular pdf whose variance is given by

$$\sigma_q^2 = \frac{1}{6} \tag{A.8}$$

Let us assume that the variance of thermal noise is given by σ_n^2. Then the total noise and

distortion is given by $\sigma^2_{total} = \sigma^2_n + \sigma^2_q + \sigma^2_{aj}$.

For a DAC, bandwidth limitation reduce the power of the input signal and color the noise spectra. Therefore,

$$P_{signal} = \frac{2^{2N}}{8}|H(f)|^2 \tag{A.9}$$

$$\sigma^2_{total,filtered} = \sigma^2_{total}\frac{1}{f_B}\int_0^{f_B}|H(\nu)|^2 d\nu \tag{A.10}$$

where f is the frequency of the sinusoid, $H(f)$ is the normalized filter response, $|.|$ is the absolute value, and f_B is the bandwidth over which the noise is measured. f_B is usually set to half the sampling rate of the EC. Note that for an ADC, there will be no coloration of noise as the distortions arising from an ADC is introduced to the signal after the signal is low-pass filtered. ENoB improvements due to coloration of noise is known as processing gain [145].

Computing the frequency dependent ENoB by substituting the SINAD in Eqn. 2.43, we have

$$ENoB(f) = 0.5 \times \log_2(SINAD) - 0.5 \times \log_2(1.5) \tag{A.11}$$

$$= 0.5 \times \log_2\left(\frac{P_{signal}}{\sigma^2_{total,filtered}}\right) - 0.5 \times \log_2(1.5) \tag{A.12}$$

$$= 0.5 \times \log_2\left(\frac{2^{2N}|H(f)|^2}{8}\right) - 0.5 \times \log_2\left(\sigma^2_{total}\frac{1}{f_B}\int_0^{f_B}|H(\nu)|^2 d\nu\right)$$
$$- 0.5 \times \log_2(\frac{12}{8}) \tag{A.13}$$

$$= 0.5 \times \log_2\left(2^{2N}|H(f)|^2\right) - 0.5 \times \log_2(\sigma^2_{total})$$
$$- 0.5 \times \log_2\left(\frac{1}{f_B}\int_0^{f_B}|H(\nu)|^2 d\nu\right) - 0.5 \times \log_2(12) \tag{A.14}$$

$$= N + \log_2(|H(f)|) - 0.5 \times \log_2(12\sigma^2_n + 12\sigma^2_q + 12\sigma^2_{aj})$$
$$- 0.5 \times \log_2\left(\frac{1}{f_B}\int_0^{f_B}|H(\nu)|^2 d\nu\right) \tag{A.15}$$

Substituting the different noise variances,

$$\begin{aligned} ENoB(f) &= N + \log_2(|H(f)|) - 0.5 \times \log_2\left(\frac{1}{f_B}\int_0^{f_B}|H(\nu)|^2 d\nu\right) \\ &\quad - 0.5 \times \log_2(12\sigma_n^2 + 2 + 6\sigma_{tj}^2 2^{2N}\pi^2 f^2) \qquad \text{(A.16)} \\ &= N + \log_2(|H(f)|) - 0.5 \times \log_2\left(\frac{1}{f_B}\int_0^{f_B}|H(\nu)|^2 d\nu\right) \\ &\quad - 0.5 \times \log_2(1 + 6\sigma_{tj}^2 2^{2N}\pi^2 f^2) \\ &\quad - 0.5 \times \log_2\left(\frac{12\sigma_n^2 + 2 + 6\sigma_{tj}^2 2^{2N}\pi^2 f^2}{1 + 6\sigma_{tj}^2 2^{2N}\pi^2 f^2}\right) \qquad \text{(A.17)} \\ &= N + \log_2(|H(f)|) - 0.5 \times \log_2\left(\frac{1}{f_B}\int_0^{f_B}|H(\nu)|^2 d\nu\right) \\ &\quad - 0.5 \times \log_2(1 + 6\sigma_{tj}^2 2^{2N}\pi^2 f^2) \\ &\quad - 0.5 \times \log_2\left(1 + \frac{12\sigma_n^2 + 1}{1 + 6\sigma_{tj}^2 2^{2N}\pi^2 f^2}\right) \qquad \text{(A.18)} \end{aligned}$$

The last term on the RHS sharply decreases to 0 as a function of f. Thus, it can be assumed as a low frequency degradation and merged with N to give $ENoB_{DC}$. Additionally, we substitute N in $0.5 \times \log_2(1 + 6\sigma_{tj}^2 2^{2N}\pi^2 f^2)$ to $ENoB_{DC}$ to reduce the number of independent variables. Applying these two modification, we have the frequency dependent ENoB of a DAC as

$$\begin{aligned} ENoB(f) &= ENoB_{DC} + \log_2(|H(f)|) - 0.5 \times \log_2\left(1 + 6(2^{ENoB_{DC}}\pi f)^2\sigma_{tj}\right) \\ &\quad - \frac{1}{2} \times \log_2\left(\frac{1}{f_B}\int_0^{f_B}|H(\nu)|^2 d\nu\right) \qquad \text{(A.19)} \end{aligned}$$

Since ADCs do not low-pass filter its own noise and distortions, there will be no processing gain in an ADC and its frequency dependent ENoB is given by

$$ENoB(f) = ENoB_{DC} + \log_2(|H(f)|) - 0.5 \times \log_2\left(1 + 6(2^{ENoB_{DC}}\pi f\sigma_{tj})^2\right) \qquad \text{(A.20)}$$

APPENDIX B
POLYBINARY CODING FOR LOW COMPLEXITY HIGH SPEED ERROR-FREE VCSEL-MMF LINKS

VCSELs with multimode fibers and direct detect receivers dominate deployments of short reach optical links owing to their power efficiency, low cost, and small form factor. Traditionally, such links have been operated at error-free BERs (10^{-12}) using PAM-2 modulation format without equalization or FEC. Recently, equalization (both analog and digital) and higher modulation formats have become common place [72, 150, 172]. However, these techniques are computationally expensive, and increase latency and power requirements. Such trade-off are detrimental to short reach applications such as high performance computing (HPC) and data centers (DC). Thus, there is a need to identify techniques that increase link bitrates while retaining the low complexity of direct modulation and detection.

B.1 Polybinary Coding

Correlated coding is a popular technique used to increase bitrates in bandlimited channels [173]. The technique introduces correlations between generated symbols to decrease the signal's bandwidth. If the initial symbols are from PAM-2 modulation format, symbols generated using correlative coding are known as polybinary symbols. They are given by

$$a_n = \sum_{i=0}^{k-1} x_{n+i} \tag{B.1}$$

where x_n are the PAM-2 symbols. The bandwidth of a_n is reduced by a factor of k and the number of amplitude levels are increased by $(k-1)$.

Even though polybinary signaling introduces multiple levels and may seem like a higher modulation format, there can be significant advantages to using polybinary signaling in-

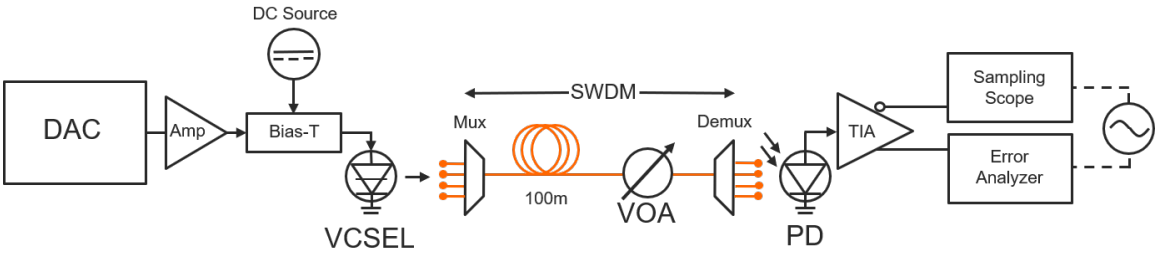

Figure B.1: VCSEL-MMF experimental setup for duobinary signaling [72]

stead of traditional multilevel signaling such as PAM-4 and PAM-8. Firstly, polybinary signals have smaller implementation complexity. The transmitter can be implemented using delays-and-adds. A traditional multilevel signal generator would require a serial to parallel converter at the transmitter and a parallel to serial converter at the receiver. Secondly, polybinary signals have the same horizontal eye opening as PAM-2 eyes operating at the same bitrate since only adjacent vertical transitions are allowed. Thus, polybinary coding is more robust to receiver timing jitter. Finally, for the same bandwidth and the same number of levels, polybinary signal increases the bitrate by a larger factor when compared to traditional multilevel signals. This is because a traditional multilevel signal with k levels increases the bitrate by $\log_2(k)$ and a polybinary signal increases the bitrate by $(k-1)$. The converse would be that for the same increase in bitrate, polybinary signals have fewer number of eyes and thus a smaller eye closure penalty.

B.2 Experimental Setup

We use an SWDM capable VCSEL-MMF testbed for our demonstration, Fig. B.1 [72]. The polybinary signal was implemented digitally using appropriate delays and additions. The optical signal was transported through 105m of wideband OM5 fiber [174] and the error rate was directly measured with an SHF 11100A bit error rate tester (BERT). Received optical power required to support BER = 10^{-12} were also measured. Two VCSELs [175, 176] with different bandwidths were examined to analyze the performance of polybinary signaling under different bandwidth constraints. The lower bandwidth VCSEL is VCSEL

Table B.1: Maximum bitrate (Gbps) (BER $<10^{-12}$) achieved for different formats through 105m of wideband fiber

	VCSEL 1	VCSEL 2
PAM-2	44	58
Duobinary	66	80
Polybinary-3	52	81
PAM-4	72	86

1 and the higher bandwidth VCSEL is VCSEL 2. For the purposes of fair comparison, the input RF swing (peak-to-peak voltage) was fixed for each modulation format. Since we are using a traditional PAM-2 BERT, the BER was calculated using the BER of each individual eye. For any polybinary signal at high SNR, the BER is given by

$$BER = \sum_i BER_i \tag{B.2}$$

where BER_i refers to the BER of the ith eye.

B.3 Results and Discussion

The maximum data rate achieved for each modulation format is listed in Table B.1. Using VCSEL 1, we were able to achieve similar data rates for PAM-4 and duobinary. The received power requirements were also similar. Polybinary-3, however, was only able to achieve 52 Gbps. This is far less than what is anticipated since polybinary-3 occupies 3 times less bandwidth than PAM-2. Polybinary-3 has a correlation depth of 3 and hence has 4 amplitude levels. VCSEL 2, however, was able to achieve similar data rates for duobinary, polybinary-3 and PAM-4 with comparable received optical power.

Figure B.2 shows the average received power required to achieve a certain bitrate for error-free signaling (BER $<10^{-12}$) using different modulation formats. As expected, the required received power increases monotonically for PAM-2 and PAM-4. Surprisingly, duobinary does not exhibit a monotonic trend. There appears to be one local maxima in its

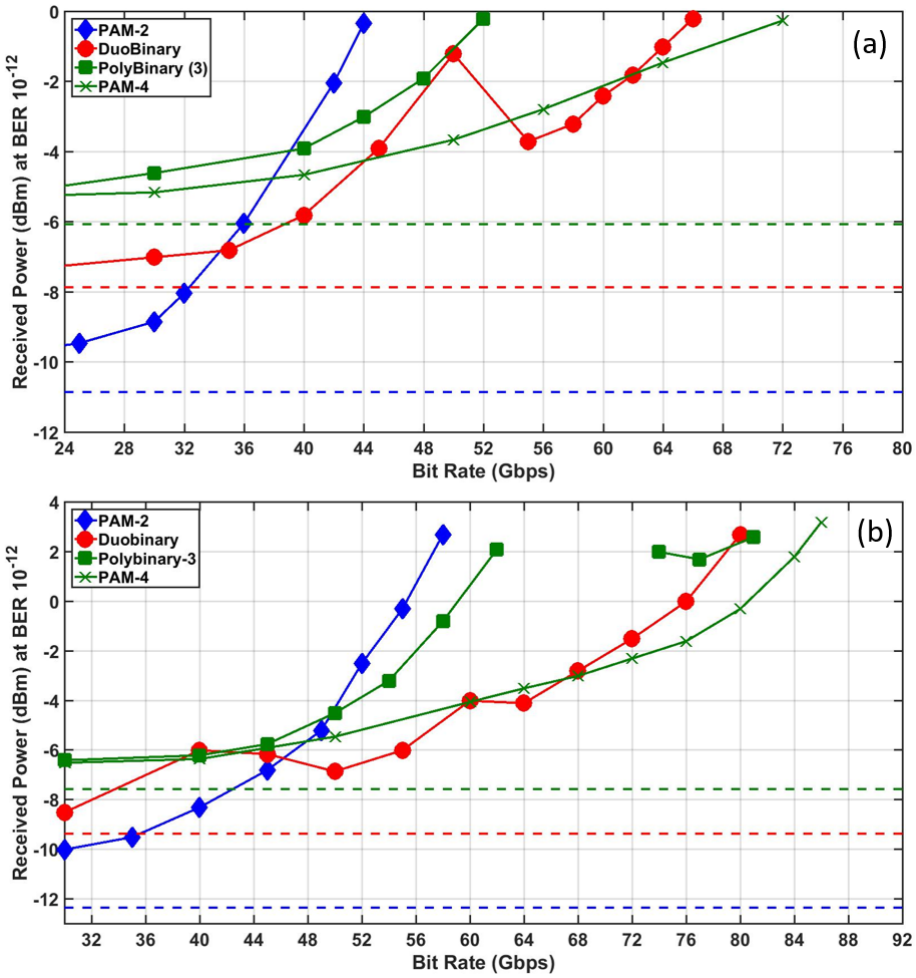

Figure B.2: Average received power required to achieve a certain bitrate at BER $<10^{-12}$. Dashed lines correspond to the thermal limit with the associated eye closure penalty. Blue corresponds to two level signals (PAM-2), red to three level signals (Duobinary) and green to four level signals (Polybinary-3 and PAM-4). (a) VCSEL 1 and (b) VCSEL 2

power requirements. Using VCSEL 2, we observed that polybinary-3 was able to achieve 30-62 Gbps and then 74-81 Gbps. The gap suggests that the power required for polybinary-3 between 62 Gbps and 74 Gbps exceeded the capabilities of the VCSEL.

We further investigate this non-monotonic trend of polybinary signaling by examination of the received extinction ratio, Fig. B.3. The average optical power and the input RF swing were kept constant. The extinction ratio of PAM-4 decreases as the bitrate increases owing to the bandwidth of the link. However, duobinary has a local maxima and polybinary-3 has two local maxima. Comparing Fig. B.2 and Fig. B.3, we see that the local maxima of

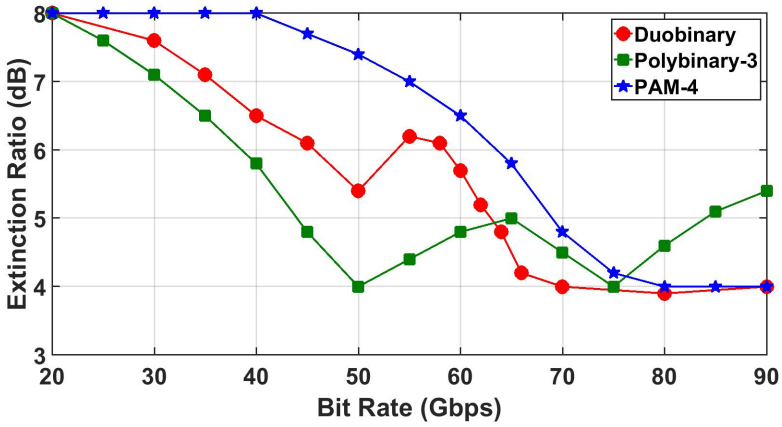

Figure B.3: Extinction ratio of the received optical signal for different bitrate and formats for a fixed input RF swing and fixed received optical power with VCSEL 1

duobinary extinction ratios corresponds to the local minima in the required power. Vice-versa is also true. Interestingly, there exists two local maximas for polybinary-3. We could not exploit these maximas since the first maxima did not have sufficient extinction ratio and the second maxima was very close to the sampling rate of the AWG (92 GSa/s). However, the existence of the second maxima with a higher extinction ratio suggests that higher bitrates could be achieved with polybinary-3 if AWGs with higher sampling rates are used.

Through an analysis of the Fourier spectra of the signals from the two VCSELs, we observed a strong correlation between the bandwidth of the link and the performance of certain bitrates. This suggests that low pass filtering the signal after the delay-and-add filter improves the performance of polybinary signaling by ensuring excess spectral content is removed. Indeed the requirement that proper trimming of spectral content is required to maximize the performance of polybinary signals is well documented [177]. We implemented a low pass filter digitally using our AWG for duobinary signals. The 3-dB bandwidth of the filter was set at half the bitrate. Figure B.4 shows the performance of the duobinary signal with the additional low pass filter. Low pass filtering the duobinary signal renders the behavior monotonic with an improved performance. However, the improvements in performance is limited to bitrates $<$64 Gbps. The performances are the same at higher bitrates since the added filter has little effect at those bitrates. The intrinsic channel

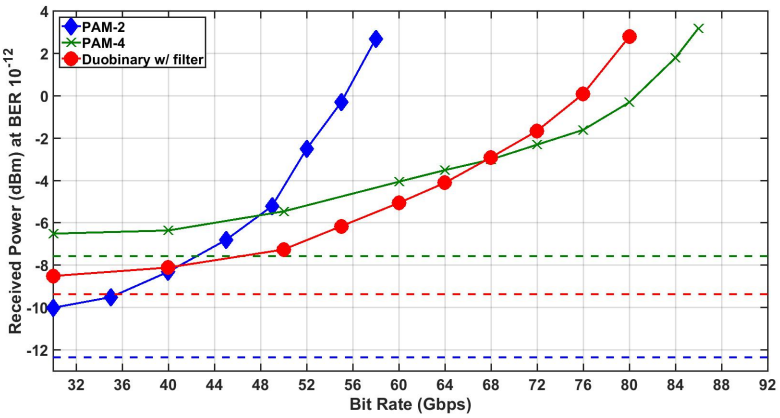

Figure B.4: Average received power required to achieve a certain bitrate at 10^{-12} BER with transmitter low-pass filtering.

bandwidth alone provides sufficient filtering.

REFERENCES

[1] *Cisco Annual Internet Report (20182023) White Paper*.

[2] Peter J. Winzer, David T. Neilson, and Andrew R. Chraplyvy. "Fiber-optic transmission and networking: the previous 20 and the next 20 years [Invited]". In: *Opt. Express* 26.18 (Sept. 2018), pp. 24190–24239.

[3] Mohammad Al-Amri, Mohamed El-Gomati, and M. Zubairy. *Optics in Our Time*. Dec. 2016.

[4] Govind P. Agarwal. *Fiber-Optic Communication Systems*. Wiley, 2010.

[5] S. Kumar and M. Jamal Deen. *Fiber Optic Communications: Fundamentals and Applications*. Wiley, 2014.

[6] Ian Goodfellow, Yoshua Bengio, and Aaron Courville. *Deep Learning*. `http://www.deeplearningbook.org`. MIT Press, 2016.

[7] Ignace Urbain Jean Chappe. *HISTOIRE DE LA TLGRAPHIE*. 1840.

[8] Alexander Jones. *Historical sketch of the electric telegraph: including its rise and progress in the United States*. 1852.

[9] Theodore Maiman. "Stimulated Optical Radiation in Ruby". In: *Nature* 187 (1 Aug. 1960), pp. 493–494.

[10] K. C. Kao and G. A. Hockham. "Dielectric-fibre surface waveguides for optical frequencies". In: *Proceedings of the Institution of Electrical Engineers* 113.7 (July 1966), pp. 1151–1158.

[11] F. P. Kapron, D. B. Keck, and R. D. Maurer. "RADIATION LOSSES IN GLASS OPTICAL WAVEGUIDES". In: *Applied Physics Letters* 17.10 (1970), pp. 423–425.

[12] T. Miya et al. "Ultimate low-loss single-mode fibre at 1.55 um". In: *Electronics Letters* 15.4 (Feb. 1979), pp. 106–108.

[13] Max Born et al. *Principles of Optics: Electromagnetic Theory of Propagation, Interference and Diffraction of Light*. 7th ed. Cambridge University Press, 1999.

[14] Z. Alferov. “Double heterostructure lasers: early days and future perspectives”. In: *IEEE Journal of Selected Topics in Quantum Electronics* 6.6 (2000), pp. 832–840.

[15] I. Hayashi et al. “JUNCTION LASERS WHICH OPERATE CONTINUOUSLY AT ROOM TEMPERATURE”. In: *Applied Physics Letters* 17.3 (1970), pp. 109–111.

[16] Jeff Hecht. *City of Light. The Story of Fiber Optics*. Oxford University Press, USA, 1999.

[17] M. I. Schwartz et al. “Atlanta fiber system experiment: The chicago lightwave communications project”. In: *The Bell System Technical Journal* 57.6 (1978), pp. 1881–1888.

[18] R. Berry, D. Brace, and I. Ravenscroft. “Optical Fiber System Trials at 8 Mbits/s and 140 Mbits/s”. In: *IEEE Transactions on Communications* 26.7 (1978), pp. 1020–1027.

[19] A. Moncalvo and F. Tosco. “European Field Trials and Early Applications in Telephony”. In: *IEEE Journal on Selected Areas in Communications* 1.3 (1983), pp. 398–403.

[20] Tingye Li. “Advances in Optical Fiber Communications: An Historical Perspective”. In: *IEEE Journal on Selected Areas in Communications* 1.3 (1983), pp. 356–372.

[21] Govind Agarwal. *Nonlinear Fiber Optics*. Academic Press, 2019.

[22] A. R. Chraplyvy, R. W. Tkach, and K. L. Walker. *Optical fiber for wavelength division multiplexing*. U. S. Patent 5,327,516. 1994.

[23] R. Essiambre, P. Winzer, and D. Grosz. “Impact of DCF properties on system design”. In: *J Optic Comm* 3 (2006), pp. 221–291.

[24] A. M. Vengsarkar et al. “Fundamental-mode dispersion-compensating fibers: design considerations and experiments”. In: *Conference on Optical Fiber Communication*. Optical Society of America, 1994, ThK2.

[25] Ashish M. Vengsarkar, Anne E. Miller, and W. A. Reed. “Highly efficient single-mode fiber for broadband dispersion compensation”. In: *Conference on Optical Fiber Communication/International Conference on Integrated Optics and Optical Fiber Communication*. Optical Society of America, 1993, PD13.

[26] Joseph Ford et al. “Wavelength add-drop switching using tilting micromirrors”. In: *Lightwave Technology, Journal of* 17 (June 1999), pp. 904–911.

[27] W. T. Anderson et al. “The MONET project-a final report”. In: *Journal of Lightwave Technology* 18.12 (2000), pp. 1988–2009.

[28] P. J. Winzer and R. J. Essiambre. “Advanced Optical Modulation Formats”. In: *Proceedings of the IEEE* 94.5 (2006), pp. 952–985.

[29] R. A. Linke and A. H. Gnauck. “High-capacity coherent lightwave systems”. In: *Journal of Lightwave Technology* 6.11 (1988), pp. 1750–1769.

[30] A Farbert et al. “Performance of a 10.7 Gb/s Receiver With Digital Equaliser Using Maximum Likelihood Sequence Estimation”. In: Jan. 2011, Th.4.1.5.

[31] Nikola Alić et al. “Signal statistics and maximum likelihood sequence estimation in intensity modulated fiber optic links containing a single optical preamplifier”. In: *Opt. Express* 13.12 (2005), pp. 4568–4579.

[32] D. McGhan et al. “5120-km RZ-DPSK transmission over G.652 fiber at 10 Gb/s without optical dispersion compensation”. In: *IEEE Photonics Technology Letters* 18.2 (2006), pp. 400–402.

[33] Seb Savory et al. “Digital Equalisation of 40Gbit/s per Wavelength Transmission over 2480km of Standard Fibre without Optical Dispersion Compensation”. In: Oct. 2006, pp. 1 –2.

[34] T. Okoshi and K. Kikuchi. *Coherent Optical Fiber Communications*. Springer, 1988.

[35] Y. Tamura et al. “The First 0.14-dB/km Loss Optical Fiber and its Impact on Submarine Transmission”. In: *Journal of Lightwave Technology* 36.1 (2018), pp. 44–49.

[36] P. Poggiolini et al. “The GN-Model of Fiber Non-Linear Propagation and its Applications”. In: *Journal of Lightwave Technology* 32.4 (2014), pp. 694–721.

[37] Andrea Carena et al. “EGN model of non-linear fiber propagation”. In: *Opt. Express* 22.13 (2014), pp. 16335–16362.

[38] W. D. Grover. “Forward error correction in dispersion-limited lightwave systems”. In: *Journal of Lightwave Technology* 6.5 (1988), pp. 643–654.

[39] ITU-T G.975. *Forward error correction for submarine systems*. `www.itu.int/rec/T-REC-G.975-200010-I/en`. 2000.

[40] C. E. Shannon. “A mathematical theory of communication”. In: *The Bell System Technical Journal* 27.3 (1948), pp. 379–423.

[41] G. Bosco. *Optical Communication Theory and Techniques. Soft Decoding in Optical Systems: Turbo Product Codes vs. LDPC Codes*. Springer, 2005.

[42] F. R. Kschischang. "Codes defined on graphs". In: *IEEE Communications Magazine* 41.8 (2003), pp. 118–125.

[43] D. J. Costello and G. D. Forney. "Channel coding: The road to channel capacity". In: *Proceedings of the IEEE* 95.6 (2007), pp. 1150–1177.

[44] F. Buchali et al. "Rate Adaptation and Reach Increase by Probabilistically Shaped 64-QAM: An Experimental Demonstration". In: *Journal of Lightwave Technology* 34.7 (2016), pp. 1599–1609.

[45] K. Schuh et al. "15.4 Tb/s transmission over 2400 km using polarization multiplexed 32-Gbaud 16-QAM modulation and coherent detection comprising digital signal processing". In: *2011 37th European Conference and Exhibition on Optical Communication*. 2011, pp. 1–3.

[46] P. J. Winzer et al. "56-Gbaud PDM-QPSK: coherent detection and 2,500-km transmission". In: *2009 35th European Conference on Optical Communication*. Vol. 2009-Supplement. 2009, pp. 1–2.

[47] G. Raybon et al. "Single-carrier all-ETDM 1.08-Terabit/s line rate PDM-64-QAM transmitter using a high-speed 3-bit multiplexing DAC". In: *2015 IEEE Photonics Conference (IPC)*. 2015, pp. 1–2.

[48] A. Ghazisaeidi et al. "Advanced C+L-Band Transoceanic Transmission Systems Based on Probabilistically Shaped PDM-64QAM". In: *Journal of Lightwave Technology* 35.7 (2017), pp. 1291–1299.

[49] B. Collings. "New devices enabling software-defined optical networks". In: *IEEE Communications Magazine* 51.3 (2013), pp. 66–71.

[50] D. T. Neilson et al. "Wavelength selective switching for optical bandwidth management". In: *Bell Labs Technical Journal* 11.2 (2006), pp. 105–128.

[51] G. Baxter et al. "Highly programmable wavelength selective switch based on liquid crystal on silicon switching elements". In: *2006 Optical Fiber Communication Conference and the National Fiber Optic Engineers Conference*. 2006, pp. 1–3.

[52] Annalisa Morea et al. "Throughput Comparison Between 50-GHz and 37.5-GHz Grid Transparent Networks [Invited]". In: *J. Opt. Commun. Netw.* 7.2 (2015), A293–A300.

[53] Faisal Nadeem Khan et al. “An Optical Communication’s Perspective on Machine Learning and Its Applications”. In: *J. Lightwave Technol.* 37.2 (2019), pp. 493–516.

[54] F. Musumeci et al. “A Tutorial on Machine Learning for Failure Management in Optical Networks”. In: *Journal of Lightwave Technology* 37.16 (2019), pp. 4125–4139.

[55] D. Gloge. “Weakly Guiding Fibers”. In: *Appl. Opt.* 10.10 (1971), pp. 2252–2258.

[56] A. W. Snyder and J. Love. *Optical Waveguide Theory*. Springer US, 1983.

[57] D. Marcuse. “Gaussian approximation of the fundamental modes of graded-index fibers”. In: *J. Opt. Soc. Am.* 68.1 (1978), pp. 103–109.

[58] C. D. Poole, J. H. Winters, and J. A. Nagel. “Dynamical equation for polarization dispersion”. In: *Opt. Lett.* 16.6 (1991), pp. 372–374.

[59] A. C. Hart, R. G. Huff, and K. L. Walker. *Method of making a fiber having low polarization mode dispersion due to a permanent spin*. U. S. Patent 5,298,047. 1994.

[60] Sergey Ten. “Ultra Low-loss Optical Fiber Technology”. In: *Optical Fiber Communication Conference*. Optical Society of America, 2016, Th4E.5.

[61] Yoshiaki Tamura et al. “Lowest-Ever 0.1419-dB/km Loss Optical Fiber”. In: *Optical Fiber Communication Conference Postdeadline Papers*. Optical Society of America, 2017, Th5D.1.

[62] C. RAMAN and K. KRISHNAN. “A New Type of Secondary Radiation”. In: *Nature* 121.1 (1928), pp. 501–502.

[63] Robert Boyd. *Nonlinear Optics*. Academic Press, 2008.

[64] K. Mochizuki, N. Edagawa, and Y. Iwamoto. “Amplified spontaneous Raman scattering in fiber Raman amplifiers”. In: *Journal of Lightwave Technology* 4.9 (1986), pp. 1328–1333.

[65] N. A. Olsson and J. P. van der Ziel. “FIBER BRILLOUIN AMPLIFIER WITH ELECTRONICALLY CONTROLLED BANDWIDTH”. In: *Optical Fiber Communication*. Optical Society of America, 1986, PD6.

[66] Katsumi Iwatsuki et al. “5 Gb/s Optical Soliton Transmission Experiment Using Raman Amplification for Fiber-Loss Compensation”. In: *Photonics Technology Letters, IEEE* 2 (Aug. 1990), pp. 507 –509.

[67] John A. Buck. *Fundamentals of Optical Fiber*. Wiley, 2004.

[68] R. Ramaswami, K. N. Sivarajan, and G. H. Sasaki. *Optical Networks: A Practical Perspective*. Morgan Kaufmann, 2010.

[69] A. Steinkamp and E. Voges. "Higher Order Polarization-Mode Dispersion in the Presence of Polarization-Dependent Loss in Optical Fiber Systems". In: *IEEE Photonics Technology Letters* 19.2 (2007), pp. 124–126.

[70] Alan Willner, Xiaoxia Wu, and Jeng-Yuan Yang. "Optical performance monitoring: Perspectives and challenges". In: *Optical Performance Monitoring*. Ed. by Calvin C.K. Chan. Oxford: Academic Press, 2010, pp. 1 –19.

[71] Douglas Charlton et al. "Field measurements of SOP transients in OPGW, with time and location correlation to lightning strikes". In: *Opt. Express* 25.9 (2017), pp. 9689–9696.

[72] Justin Lavrencik et al. "Scaling VCSEL-MMF Links to 1 Tb/s Using Short Wavelength Division Multiplexing". In: *J. Lightwave Technol.* 36.18 (2018), pp. 4138–4145.

[73] Govind Agarwal. *Long-Wavelength Semiconductor Lasers*. Springer, 1986.

[74] C. Laperle and M. OSullivan. "Advances in High-Speed DACs, ADCs, and DSP for Optical Coherent Transceivers". In: *Journal of Lightwave Technology* 32.4 (2014), pp. 629–643.

[75] "IEEE Standard for Terminology and Test Methods of Digital-to-Analog Converter Devices". In: *IEEE Std 1658-2011* (2012), pp. 1–126.

[76] Y. Yoffe and D. Sadot. "DSP-Enhanced Analog-to-Digital Conversion for High-Speed Data Centers' Optical Connectivities". In: *IEEE Photonics Journal* 7.4 (2015), pp. 1–13.

[77] Yaron Yoffe et al. "Low-Resolution Digital Pre-Compensation Enabled by Digital Resolution Enhancer". In: *J. Lightwave Technol.* 37.6 (2019), pp. 1543–1551.

[78] A. Yariv, P.E.E.A. Yariv, and P. Yeh. *Photonics: Optical Electronics in Modern Communications*. Oxford series in electrical and computer engineering. Oxford University Press, 2007. ISBN: 9780195179460.

[79] G. R. Walker, R. C. Steele, and N. G. Walker. "Optical amplifier noise figure in a coherent optical transmission system". In: *Journal of Lightwave Technology* 8.9 (1990), pp. 1409–1413.

[80] R. Essiambre et al. “Capacity Limits of Optical Fiber Networks”. In: *Journal of Lightwave Technology* 28.4 (2010), pp. 662–701.

[81] “IEEE Draft Standard for Ethernet Amendment: Physical Layers and Management Parameters for 50 Gb/s, 200 Gb/s, and 400 Gb/s Operation over Single-Mode Fiber”. In: *IEEE P802.3cn/D3.0, July 2019* (2019), pp. 1–87.

[82] D. T. Neilson et al. “Wavelength selective switching for optical bandwidth management”. In: *Bell Labs Technical Journal* 11.2 (2006), pp. 105–128.

[83] M. Filer and S. Tibuleac. “Generalized weighted crosstalk for DWDM systems with cascaded wavelength-selective switches”. In: *OFC/NFOEC*. 2012, pp. 1–3.

[84] Y. Hsueh et al. “Passband Narrowing and Crosstalk Impairments in ROADM-Enabled 100G DWDM Networks”. In: *Journal of Lightwave Technology* 30.24 (2012), pp. 3980–3986.

[85] A.E.B Saleh and M.C Teich. *Fundamentals of Photonics*. 1991.

[86] Gengchen Liu et al. “Demonstration of a carrier frequency offset estimator for 16-/32-QAM coherent receivers: a hardware perspective”. In: *Opt. Express* 26.4 (2018), pp. 4853–4862.

[87] Md. Saifuddin Faruk and Seb J. Savory. “Digital Signal Processing for Coherent Transceivers Employing Multilevel Formats”. In: *J. Lightwave Technol.* 35.5 (2017), pp. 1125–1141.

[88] J.G. Proakis. *Digital Communications*. McGraw-Hill series in electrical and computer engineering : communications and signal processing. McGraw-Hill, 2001. ISBN: 9780071181839.

[89] Fred Buchali et al. “Rate Adaptation and Reach Increase by Probabilistically Shaped 64-QAM: An Experimental Demonstration”. In: *Journal of Lightwave Technology* (Dec. 2015).

[90] P. Schulte and G. Bcherer. “Constant Composition Distribution Matching”. In: *IEEE Transactions on Information Theory* 62.1 (2016), pp. 430–434.

[91] J. Cho et al. “Trans-Atlantic Field Trial Using High Spectral Efficiency Probabilistically Shaped 64-QAM and Single-Carrier Real-Time 250-Gb/s 16-QAM”. In: *Journal of Lightwave Technology* 36.1 (2018), pp. 103–113.

[92] Tao Liu and Ivan B. Djordjevic. “Optimal signal constellation design for ultra-high-speed optical transport in the presence of nonlinear phase noise”. In: *Opt. Express* 22.26 (2014), pp. 32188–32198.

[93] Lotfollah Beygi, Erik Agrell, and Magnus Karlsson. “Optimization of 16-point Ring Constellations in the Presence of Nonlinear Phase Noise”. In: *Optical Fiber Communication Conference/National Fiber Optic Engineers Conference 2011*. Optical Society of America, 2011, OThO4.

[94] Z. Qu and I. B. Djordjevic. “On the Probabilistic Shaping and Geometric Shaping in Optical Communication Systems”. In: *IEEE Access* 7 (2019), pp. 21454–21464.

[95] M. G. Taylor. “Coherent detection method using DSP for demodulation of signal and subsequent equalization of propagation impairments”. In: *IEEE Photonics Technology Letters* 16.2 (2004), pp. 674–676.

[96] R. Kudo et al. “Coherent Optical Single Carrier Transmission Using Overlap Frequency Domain Equalization for Long-Haul Optical Systems”. In: *Journal of Lightwave Technology* 27.16 (2009), pp. 3721–3728.

[97] M. Oerder and H. Meyr. “Digital filter and square timing recovery”. In: *IEEE Transactions on Communications* 36.5 (1988), pp. 605–612.

[98] Chang Yuxin et al. “Mode demultiplexing based on multimodulus blind equalization algorithm”. In: *Optics Communications* 324 (2014), pp. 311 –317.

[99] Dominique Godard. “Self-Recovering Equalization and Carrier Tracking in Two-Dimensional Data Communication Systems”. In: 1980.

[100] C. Xie and S. Chandrasekhar. “Two-stage constant modulus algorithm equalizer for singularity free operation and optical performance monitoring in optical coherent receiver”. In: *2010 Conference on Optical Fiber Communication (OFC/NFOEC), collocated National Fiber Optic Engineers Conference*. 2010, pp. 1–3.

[101] L. Liu et al. “Initial tap setup of constant modulus algorithm for polarization demultiplexing in optical coherent receivers”. In: *2009 Conference on Optical Fiber Communication - incudes post deadline papers*. 2009, pp. 1–3.

[102] S.S. Haykin. *Unsupervised Adaptive Filtering: Blind source separation*. Wiley-Interscience publication. Wiley, 2000.

[103] H. Zhang et al. “Polarization demultiplexing based on independent component analysis in optical coherent receivers”. In: Oct. 2008, pp. 1 –2.

[104] P. Johannisson et al. “Convergence Comparison of the CMA and ICA for Blind Polarization Demultiplexing”. In: *IEEE/OSA Journal of Optical Communications and Networking* 3.6 (2011), pp. 493–501.

[105] A. Leven et al. “Frequency Estimation in Intradyne Reception”. In: *IEEE Photonics Technology Letters* 19.6 (2007), pp. 366–368.

[106] A. Tarighat et al. “Digital adaptive phase noise reduction in coherent optical links”. In: *Journal of Lightwave Technology* 24.3 (2006), pp. 1269–1276.

[107] B. Widrow, J. McCool, and M. Ball. “The complex LMS algorithm”. In: *Proceedings of the IEEE* 63.4 (1975), pp. 719–720.

[108] E. Ip and J. M. Kahn. “Compensation of Dispersion and Nonlinear Impairments Using Digital Backpropagation”. In: *Journal of Lightwave Technology* 26.20 (2008), pp. 3416–3425.

[109] Fernando P. Guiomar et al. “Mitigation of intra-channel nonlinearities using a frequency domain Volterra series equalizer”. In: *Opt. Express* 20.2 (2012), pp. 1360–1369.

[110] Y. Cai et al. “Experimental demonstration of coherent MAP detection for nonlinearity mitigation in long-haul transmissions”. In: *2010 Conference on Optical Fiber Communication (OFC/NFOEC), collocated National Fiber Optic Engineers Conference*. 2010, pp. 1–3.

[111] Erik Agrell et al. “Roadmap on Optical Communications”. In: *Journal of Optics* 18 (May 2016).

[112] J. King, D. Leyba, and G. D. LeCheminant. “TDECQ (transmitter dispersion eye closure quaternary) replaces historic eye-mask and TDP test for 400 Gb/s PAM4 optical transmitters”. In: *2017 Optical Fiber Communications Conference and Exhibition (OFC)*. 2017, pp. 1–3.

[113] *SSPRQ test pattern*. `http://www.ieee802.org/3/bs/public/adhoc/smf/16_04_19/anslow_01_0416_smf.pdf`.

[114] “IEEE Standard for Ethernet - Amendment 10: Media Access Control Parameters, Physical Layers, and Management Parameters for 200 Gb/s and 400 Gb/s Operation”. In: *IEEE Std 802.3bs-2017 (Amendment to IEEE 802.3-2015 as amended by IEEE’s 802.3bw-2015, 802.3by-2016, 802.3bq-2016, 802.3bp-2016, 802.3br-2016, 802.3bn-2016, 802.3bz-2016, 802.3bu-2016, 802.3bv-2017, and IEEE 802.3-2015/Cor1-2017)* (2017), pp. 1–372.

[115] W.S. McCulloch and W Pitts. “A logical calculus of the ideas immanent in nervous activity”. In: *Bulletin of Mathematical Biophysics* 5 (Dec. 1943).

[116] B Widrow. “An Adaptive ’Adaline’ Neuron Using Chemical Memistors”. In: *Stanford Electronics Laboratories Technical Report* 2 (Oct. 1960).

[117] M. Minsky and S.A Papert. *Perceptrons*. Jan. 1969. ISBN: 9780262130431.

[118] D.E Rumerlhart, J. L. McClelland, and PDP Research Group. *Parallel Distributed Processing. Explorations in the Microstructure of Cognition: Foundations*. July 1986. ISBN: 9780262181204.

[119] D. Rumelhart, G. Hinton, and R. Williams. "Learning representations by back-propagating errors". In: *Nature* 323 (July 1986), pp. 533–536.

[120] Geoffrey E. Hinton, Simon Osindero, and Yee-Whye Teh. "A Fast Learning Algorithm for Deep Belief Nets". In: *Neural Comput.* 18.7 (July 2006), 15271554.

[121] Yoshua Bengio and Yann Lecun. "Scaling learning algorithms towards AI". In: *Large-scale kernel machines*. Ed. by L. Bottou et al. MIT Press, 2007.

[122] T.M Mitchell. *Machine Learning*. 1997. ISBN: 0-07-115467-1.

[123] R.S Sutton and A.G Barto. *Reinforcement Learning*. Nov. 2018.

[124] V.N. Vapnik and A.Y. Chervonenkis. "On the uniform convergence of relative frequencies of events to their probabilities". In: Jan. 2015, pp. 11–30.

[125] Bernhard E. Boser, Isabelle M. Guyon, and Vladimir N. Vapnik. "A Training Algorithm for Optimal Margin Classifiers". In: *Proceedings of the Fifth Annual Workshop on Computational Learning Theory*. COLT 92. Pittsburgh, Pennsylvania, USA: Association for Computing Machinery, 1992, 144152. ISBN: 089791497X.

[126] C.M. Bishop. *Pattern Recognition and Machine Learning*. Information science and statistics. Springer (India) Private Limited, 2013. ISBN: 9788132209065.

[127] Michael Bianco et al. "Machine learning in acoustics: a review". In: (May 2019).

[128] Yann Lecun. "Generalization and network design strategies". In: *Connectionism in perspective*. Ed. by R. Pfeifer et al. Elsevier, 1989.

[129] Alex Graves et al. *A Novel Connectionist System for Unconstrained Handwriting Recognition*. 2008.

[130] Y. Bengio, P. Simard, and P. Frasconi. "Learning long-term dependencies with gradient descent is difficult". In: *IEEE Transactions on Neural Networks* 5.2 (1994), pp. 157–166.

[131] Sepp Hochreiter and Jrgen Schmidhuber. "Long Short-Term Memory". In: *Neural Computation* 9.8 (1997), pp. 1735–1780.

[132] B. Schlkopf et al. “Estimating the Support of a High-Dimensional Distribution”. In: *Neural Computation* 13.7 (2001), pp. 1443–1471.

[133] Geoffrey E Hinton and James L. McClelland. “Learning Representations by Recirculation”. In: *Neural Information Processing Systems*. Ed. by D. Z. Anderson. American Institute of Physics, 1988, pp. 358–366.

[134] Karl Pearson F.R.S. “LIII. On lines and planes of closest fit to systems of points in space”. In: *The London, Edinburgh, and Dublin Philosophical Magazine and Journal of Science* 2.11 (1901), pp. 559–572.

[135] V. Curri, M. Cantono, and R. Gaudino. “Elastic All-Optical Networks: A New Paradigm Enabled by the Physical Layer. How to Optimize Network Performances?” In: *Journal of Lightwave Technology* 35.6 (2017), pp. 1211–1221.

[136] John C. Cartledge et al. “Digital signal processing for fiber nonlinearities”. In: *Opt. Express* 25.3 (2017), pp. 1916–1936.

[137] David S. Millar et al. “Design of a 1 Tb/s Superchannel Coherent Receiver”. In: *J. Lightwave Technol.* 34.6 (2016), pp. 1453–1463.

[138] Tomislav Drenski and Jens. C. Rasmussen. “ADC & DAC - Technology Trends and Steps to Overcome Current Limitations”. In: *Optical Fiber Communication Conference*. Optical Society of America, 2018, p. M2C.1.

[139] X. Chen et al. “Experimental quantification of implementation penalties from limited ADC resolution for Nyquist shaped higher-order QAM”. In: *2016 Optical Fiber Communications Conference and Exhibition (OFC)*. 2016, pp. 1–3.

[140] D. Rafique et al. “Digital Preemphasis in Optical Communication Systems: On the DAC Requirements for Terabit Transmission Applications”. In: *Journal of Lightwave Technology* 32.19 (2014), pp. 3247–3256.

[141] *Keysight M8195A datasheet*. `https://www.keysight.com/us/en/assets/7018-04509/data-sheets/5992-0014.pdf`.

[142] R.J. van de Plassche. *Integrated Analog-to-digital and Digital-to-analog Converters*. Kluwer international series in engineering and computer science. Kluwer Academic Publishers, 1994. ISBN: 9780792394365.

[143] I. Opris. *Challenges in A/D Design and Practical Understanding of A/D Specifications*. IEEE Chapter Meeting Presentation. Apr. 2003.

[144] “IEEE Standard for Terminology and Test Methods of Digital-to-Analog Converter Devices”. In: *IEEE Std 1658-2011* (2012), pp. 1–126.

[145] W. Kester. *Taking the Mystery out of the Infamous Formula, "SNR = 6.02N + 1.76dB," and Why You Should Care*. Analog Devices Tutorial, MT-001. 2009.

[146] Anatol Khilo et al. "Photonic ADC: overcoming the bottleneck of electronic jitter". In: *Opt. Express* 20.4 (2012), pp. 4454–4469.

[147] "IEEE Standard for Terminology and Test Methods for Analog-to-Digital Converters". In: *IEEE Std 1241-2010 (Revision of IEEE Std 1241-2000)* (2011), pp. 1–139.

[148] J. Wang, C. Xie, and Z. Pan. "Optimization of DSP to Generate Spectrally Efficient 16QAM Nyquist-WDM Signals". In: *IEEE Photonics Technology Letters* 25.8 (2013), pp. 772–775.

[149] F. Buchali et al. "Implementation of 64QAM at 42.66 GBaud using 1.5 samples per symbol DAC and demonstration of up to 300 km fiber transmission". In: *OFC 2014*. 2014, pp. 1–3.

[150] Justin Lavrencik et al. "168Gbps PAM-4 Multimode Fiber Transmission through 50m using 28GHz 850nm Multimode VCSELs". In: *Optical Fiber Communication Conference (OFC) 2020*. Optical Society of America, 2020, W1D.3.

[151] Haijiang Yu et al. "400Gbps Fully Integrated DR4 Silicon Photonics Transmitter for Data Center Applications". In: *Optical Fiber Communication Conference (OFC) 2020*. Optical Society of America, 2020, T3H.6.

[152] "Fibre optic communication system design guides - Part 8: Calculating dispersion penalty from measured time-resolved chirp data". In: *IEC TR 61282-8:2006* (2006), pp. 1–20.

[153] Tektronix. *Statistical Principles and Trends in Mask Testing*. `www.tek.com/document/whitepaper/designcon-2015-paper-statistical-principles-and-trends-mask-testing`. 2015.

[154] "IEEE Draft Standard for Ethernet Amendment 10: Media Access Control Parameters, Physical Layers and Management Parameters for 200 Gb/s and 400 Gb/s Operation". In: *IEEE P802.3bs(TM)/D3.23.3, July 2017* (2017), pp. 1–393.

[155] "IEEE Approved Draft Standard for Ethernet Amendment: Media Access Control Parameters for 50 Gb/s and Physical Layers and Management Parameters for 50 Gb/s, 100 Gb/s, and 200 Gb/s Operation". In: *IEEE P802.3cd/D3.5, September 2018 (Amendment of IEEE Std 802.3-2018 as amended by IEEE Std 802.3cb-201x and IEEE Std 802.3bt-201x)* (2018), pp. 1–408.

[156] G. D. Brown. "Bandwidth and rise time calculations for digital multimode fiber-optic data links". In: *Journal of Lightwave Technology* 10.5 (1992), pp. 672–678.

[157] T. A. Eriksson, H. Blow, and A. Leven. “Applying Neural Networks in Optical Communication Systems: Possible Pitfalls”. In: *IEEE Photonics Technology Letters* 29.23 (2017), pp. 2091–2094.

[158] Ying Zhao et al. “BER and TDECQ Correlation for Different Impairments in 400Gbps PAM4 system”. In: *Optical Fiber Communication Conference (OFC) 2020*. Optical Society of America, 2020, W3G.3.

[159] USA Keysight Technologies. *TDECQ Part II Manufacturing Test Recommendations*. `https://www.keysight.com/us/en/assets/7018-06506/white-papers/5992-3676.pdf`. 2019.

[160] Xavier Glorot and Yoshua Bengio. “Understanding the difficulty of training deep feedforward neural networks”. In: *Proceedings of the Thirteenth International Conference on Artificial Intelligence and Statistics*. Ed. by Yee Whye Teh and Mike Titterington. Vol. 9. Proceedings of Machine Learning Research. Chia Laguna Resort, Sardinia, Italy: PMLR, 2010, pp. 249–256.

[161] G. Hinton. *Neural Networks for machine learning*. `https://www.coursera.org/learn/neural-networks/home/welcome`.

[162] Diederik Kingma and Jimmy Ba. “Adam: A Method for Stochastic Optimization”. In: *International Conference on Learning Representations* (Dec. 2014).

[163] Martin Furer. “Faster Integer Multiplication”. In: *SIAM J. Comput.* 39.3 (2009), pp. 979–1005.

[164] J. Borland. *Analyzing the internet collapse*. MIT Technology Review. 2008.

[165] D. Rafique et al. “Cognitive Assurance Architecture for Optical Network Fault Management”. In: *Journal of Lightwave Technology* 36.7 (2018), pp. 1443–1450.

[166] A. P. Vela et al. “BER Degradation Detection and Failure Identification in Elastic Optical Networks”. In: *Journal of Lightwave Technology* 35.21 (2017), pp. 4595–4604.

[167] L. Shu et al. “Dual-Stage Soft Failure Detection and Identification for Low-Margin Elastic Optical Network by Exploiting Digital Spectrum Information”. In: *Journal of Lightwave Technology* (2019), pp. 1–1.

[168] X. Chen et al. “Self-Taught Anomaly Detection With Hybrid Unsupervised/Supervised Machine Learning in Optical Networks”. In: *Journal of Lightwave Technology* 37.7 (2019), pp. 1742–1749.

[169] Zhilong Wang et al. “Failure prediction using machine learning and time series in optical network”. In: *Opt. Express* 25.16 (2017), pp. 18553–18565.

[170] F. Musumeci et al. “A Tutorial on Machine Learning for Failure Management in Optical Networks”. In: *Journal of Lightwave Technology* 37.16 (2019), pp. 4125–4139.

[171] Ronen Dar et al. “Properties of nonlinear noise in long, dispersion-uncompensated fiber links”. In: *Opt. Express* 21.22 (2013), pp. 25685–25699.

[172] D. M. Kuchta et al. “A 71-Gb/s NRZ Modulated 850-nm VCSEL-Based Optical Link”. In: *IEEE Photonics Technology Letters* 27.6 (2015), pp. 577–580.

[173] A. Lender. “The duobinary technique for high-speed data transmission”. In: *IEEE Transactions on Communication and Electronics* 82.2 (1963), pp. 214–218.

[174] Y. Sun et al. “SWDM PAM4 Transmission From 850 to 1066 nm Over NG-WBMMF Using 100G PAM4 IC Chipset With Real-Time DSP”. In: *Journal of Lightwave Technology* 35.15 (2017), pp. 3149–3158.

[175] J. A. Tatum et al. “VCSEL-Based Interconnects for Current and Future Data Centers”. In: *Journal of Lightwave Technology* 33.4 (2015), pp. 727–732.

[176] P. Westbergh et al. “High-speed 850 nm VCSELs with 28 GHz modulation bandwidth operating error-free up to 44 Gbit/s”. In: *Electronics Letters* 48.18 (2012), pp. 1145–1147.

[177] S. Walklin and J. Conradi. “Multilevel signaling for increasing the reach of 10 Gb/s lightwave systems”. In: *Journal of Lightwave Technology* 17.11 (1999), pp. 2235–2248.

INTELLECTUAL PROPERTY

Patents

1. **Siddharth Varughese**, Jerrod Langston, Stephen E. Ralph, and Varghese A. Thomas, "Methods and Devices for Input Signal Conversion Simulation", U.S. Patent No. 10,666,277

2. **Siddharth Varughese**, Justin Lavrencik, Varghese A. Thomas, and Stephen E. Ralph, "Systems and Methods for Improved Data Transmission in Short-Reach Links", U.S. Patent Application No.: 16/127,177, patent pending

3. **Siddharth Varughese**, and Stephen E. Ralph, "Systems and Methods to Assess Optical Components using Real-time Signals and Machine Learning", U.S. Patent Application No.: 63/057,572, patent pending

4. Varghese A. Thomas, **Siddharth Varughese**, Saeed Zeinolabedinzadeh, Andrew J. Stark, and Stephen E. Ralph, "Quasicoherent Receivers for High Speed Optical Links", U.S. Patent Application No.: 62/937,130, patent pending

5. Daniel Lippiatt, Stephen E. Ralph, and **Siddharth Varughese**, "Linear and Nonlinear Noise Extraction by Exploiting Carrier Phase Recovery", U.S. Patent Application No.: 62/931,318, patent pending

6. **Siddharth Varughese**, and Stephen E. Ralph, "TDECQ Estimation Using Eye-Diagram Images", U.S. Patent Application No.: 62/930,681, patent pending

Journals

1. **Siddharth Varughese**, Jerrod Langston, Varghese A. Thomas, Sorin Tibuleac, and Stephen E. Ralph, "Frequency Dependent ENoB Requirements for M-QAM Optical Links: An Analysis Using an Improved Digital to Analog Converter Model," J. Lightwave Technol. 36, 4082-4089 (2018)

2. Justin Lavrencik, **Siddharth Varughese**, Varghese A. Thomas, and Stephen E. Ralph, "Scaling VCSEL-MMF Links to 1 Tb/s Using Short Wavelength Division Multiplexing," J. Lightwave Technol. 36, 4138-4145 (2018)

3. Jhon J. Granada Torres, **Siddharth Varughese**, Varghese A. Thomas, Andrea Chiuchiarelli, Stephen E. Ralph, Ana M. Crdenas Soto, Neil Guerrero Gonzlez, "Mitigation of time-varying distortions in Nyquist-WDM systems using machine learning", Optical Fiber Technology, 38, 2017, 130-135 (2017)

4. Justin Lavrencik, Varghese A. Thomas, **Siddharth Varughese**, and Stephen E. Ralph, "DSP-Enabled 100 Gb/s PAM-4 VCSEL MMF Links," J. Lightwave Technol. 35, 3189-3196 (2017)

5. **Siddharth Varughese**, Daniel Lippiatt, Sorin Tibuleac, and Stephen E. Ralph, "Frequency Dependent ENoB Requirements for 400G/600G/800G Optical Links," accepted in J. Lightwave Technol.

6. **Siddharth Varughese**, Alirio Melgar, Pavel Zivny, Shane Hazzard, and Stephen E. Ralph, "Accelerating Assessments of Optical Components using Machine Learning: TDECQ as Demonstrated Example," submitted to J. Lightwave Technol.

7. Hyung Joon Cho, **Siddharth Varughese**, Daniel Lippiatt, Richard DeSalvo, Sorin Tibuleac, and Stephen E. Ralph, "Optical performance monitoring using digital coherent receivers and convolutional neural networks," to be submitted to Opt. Express

Conference Proceedings

1. **Siddharth Varughese**, Daniel Lippiatt, Thomas Richter, Sorin Tibuleac, and Stephen E. Ralph, "Low Complexity Soft Failure Detection and Identification in Optical Links using Adaptive Filter Coefficients", Optical Fiber Communication Conference (OFC), San Diego, CA, USA, 2020

2. **Siddharth Varughese**, Daniel Garon, Alirio Melgar, Varghese A. Thomas, Pavel Zivny, Shane Hazzard, and Stephen E. Ralph, "Accelerating TDECQ Assessments using Convolutional Neural Networks", Optical Fiber Communication Conference (OFC), San Diego, CA, USA, 2020

3. Nikolay N. Ledentsov, Vitaly A. Shchukin, Vladimir P. Kalosha, Nikolay Ledentsov, Lukasz Chorchos, Jarosaw P. Turkiewicz, Urs Hecht, Patrick Kurth, Friedel Gerfers, Justin Lavrencik, Siddharth Varughese, and Stephen E. Ralph, "Optical Interconnects using Single-Mode and Multi-Mode VCSEL and Multi-Mode Fiber", Optical Fiber Communication Conference (OFC), San Diego, CA, USA, 2020

4. Hyung J. Cho, **Siddharth Varughese**, Daniel Lippiatt, and Stephen E. Ralph, "Convolutional Recurrent Machine Learning for OSNR and Launch Power Estimation: A Critical Assessment", Optical Fiber Communication Conference (OFC), San Diego, CA, USA, 2020

5. Justin Lavrencik, **Siddharth Varughese**, Nikolay Ledentsov Jr., Lukasz Chorchos, Nikolay Ledentsov, and Stephen E. Ralph, "168Gbps PAM-4 Multimode Fiber Transmission through 50m using 28GHz 850nm Multimode VCSELs", Optical Fiber Communication Conference (OFC), San Diego, CA, USA, 2020

6. Varghese A. Thomas, Alirio Melgar, **Siddharth Varughese**, Daniel Garon, Kan Tan, Shane Hazzard, Maria Agoston, Pavel Zivny, and Stephen E. Ralph, "TDECQ Sensitivity to Algorithmic Implementation and Noise Characterization", Optical Fiber Communication Conference (OFC), San Diego, CA, USA, 2020

7. Daniel Lippiatt, **Siddharth Varughese**, Thomas Richter, Sorin Tibuleac, and Stephen E. Ralph, "Joint Linear and Nonlinear Noise Estimation of Optical Links by Exploiting Carrier Phase Recovery", Optical Fiber Communication Conference (OFC), San Diego, CA, USA, 2020

8. Hyung J. Cho, Daniel Lippiatt, **Siddharth Varughese**, and Stephen E. Ralph, "Convolutional Neural Networks for Optical Performance Monitoring," IEEE Avionics and Vehicle Fiber-Optics and Photonics Conference (AVFOP), Arlington, VA, USA, 2019

9. Justin Lavrencik, **Siddharth Varughese**, Varghese A. Thomas, Johan S. Gustavsson, Erik Haglund, Anders Larsson, and Stephen E. Ralph, "102Gbps PAM-2 over 50m OM5 Fiber using 850nm Multimode VCSELs," IEEE Photonics Conference (IPC), San Antonio, TX, USA, 2019

10. **Siddharth Varughese**, Thomas Richter, Sorin Tibuleac, and Stephen E. Ralph, " Joint Optimization of DAC and ADC based on Frequency Dependent ENoB Analysis for High Speed Optical Systems", European Conference on Optical Communication (ECOC), Dublin, Ireland, 2019

11. Daniel Lippiatt, **Siddharth Varughese**, Thomas Richter, Sorin Tibuleac, and Stephen E. Ralph, "Machine-Learning-Based Optical Performance Monitoring using Carrier Phase Recovery", European Conference on Optical Communication (ECOC), Dublin, Ireland, 2019

12. Justin Lavrencik, Ewa Simpanen, Nasibeh Haghighi, **Siddharth Varughese**, Johan S. Gustavsson, Erik Haglund, W. V. Sorin, Sai Mathai, Mike Tan, James A. Lott, Anders Larsson, and Stephen E. Ralph, "Error-Free 850nm to 1060nm VCSEL Links: Feasibility of 400 Gbps and 800 Gbps 8-SWDM", European Conference on Optical Communication (ECOC), Dublin, Ireland, 2019

13. Varghese A. Thomas, **Siddharth Varughese**, and Stephen E. Ralph, "Quasicoherent Receivers for Access Networks Using Fullwave Rectification Based Envelope Detection," Conference on Lasers and Electro-Optics (CLEO), San Jose, CA, USA, 2019

14. Justin Lavrencik, Ewa Simpanen, **Siddharth Varughese**, Alirio Melgar, Varghese A. Thomas, Johan S. Gustavsson, Wayne V. Sorin, Sagi Mathai, Michael Tan, Anders Larsson, and Stephen E. Ralph, "Error-Free 100Gbps PAM-4 Transmission over 100m OM5 MMF using 1060nm VCSELs," Optical Fiber Communication Conference (OFC), San Diego, CA, USA, 2019

15. **Siddharth Varughese**, Daniel Lippiatt, Thomas Richter, Sorin Tibuleac, and Stephen E. Ralph, "Identification of Soft Failures in Optical Links Using Low Complexity Anomaly Detection," Optical Fiber Communication Conference (OFC), San Diego, CA, USA, 2019

16. **Siddharth Varughese**, Justin Lavrencik, and Stephen E. Ralph, "Probabilistic Shaping for VCSEL-MMF Links," IEEE Avionics and Vehicle Fiber-Optics and Photonics Conference (AVFOP), Portland, OR, USA, 2018

17. Varghese A. Thomas, Christian G. Bottenfield, Gareeyasee Saha, **Siddharth Varughese**, and Stephen E. Ralph, "Simulation of Integrated Transmitter with Enhanced Power for Analog RF Links," IEEE Photonics Conference (IPC), Reston, VA, 2018

18. Justin Lavrencik, **Siddharth Varughese**, Johan S. Gustavsson, Erik Haglund, Anders Larsson, and Stephen E. Ralph, "Power Efficient Modulation Formats for Error-Free VCSEL MMF Links," European Conference on Optical Communication (ECOC), Rome, Italy, 2018

19. Jerrod Langston, **Siddharth Varughese**, Richard DeSalvo, and Stephen E. Ralph, "Blind Cyclostationarity-Based Format Classification for Coherent Links," European Conference on Optical Communication (ECOC), Rome, Italy, 2018

20. Jerrod Langston, **Siddharth Varughese**, Richard DeSalvo, and Stephen E. Ralph, "Optical signal reconstruction using transmit-side DSP," IEEE Avionics and Vehicle Fiber-Optics and Photonics Conference (AVFOP), New Orleans, LA, USA, 2017

21. **Siddharth Varughese**, Jerrod Langston, Stephen E. Ralph, and Richard DeSalvo, "Blind polarization identification and demultiplexing using statistical learning," IEEE Photonics Conference (IPC), Orlando, FL, USA, 2017

22. **Siddharth Varughese**, Justin Lavrencik, Johan S. Gustavsson, Erik Haglund, Anders Larsson, and Stephen E. Ralph, "Polybinary Coding for Low Complexity High Speed Error-Free VCSEL-MMF Links," European Conference on Optical Communication (ECOC), Gothenburg, Sweden, 2017

23. Justin Lavrencik, **Siddharth Varughese**, Johan S. Gustavsson, Erik Haglund, Anders Larsson, and Stephen E. Ralph, "Error-Free 100Gbps PAM-4 Transmission over 100m Wideband Fiber using 850nm VCSELs," European Conference on Optical Communication (ECOC), Gothenburg, Sweden, 2017

24. **[Upgraded] Siddharth Varughese**, Jerrod Langston, Varghese A. Thomas, Sorin Tibuleac, and Stephen E. Ralph, "Implementing DACs in High Speed Optical Link Simulations," Advanced Photonics Congress (APC), New Orleans, LA, USA, 2017

25. Jhon J. Granada Torres, **Siddharth Varughese**, Stephen E. Ralph, A. M. Crdenas Soto, and Neil G. Gonzlez, "Clustering in Short Time Windows for Nonsymmetrical Demodulation in 16QAM Overlapped WDM Channels," Advanced Photonics Congress (APC), New Orleans, LA, USA, 2017

26. Alirio A. Melgar-Evangelista, Varghese A. Thomas, Justin Lavrencik, **Siddharth Varughese**, and Stephen E. Ralph, "Experimentally benchmarked fiber propagation model for 50Gbps PAM-4 MMF links employing multimode VCSELs," Optical Fiber Communications Conference (OFC), Los Angeles, CA, 2017

27. Justin Lavrencik, **Siddharth Varughese**, Varghese A. Thomas, Gary Landry, Yi Sun, Robert Shubochkin, Kashyapa Balemarthy, Jim Tatum, and Stephen E. Ralph, "4 100Gbps VCSEL PAM-4 Transmission over 105m of Wide Band Multimode Fiber," Optical Fiber Communications Conference (OFC), Los Angeles, CA, 2017

28. **Siddharth Varughese**, Justin Lavrencik, Varghese A. Thomas, and Stephen E. Ralph, "Raised cosine pulse shapes for next generation MMF links," IEEE Photonics Conference (IPC), Waikoloa, HI, USA, 2016

29. **Siddharth Varughese**, Varghese A. Thomas, Pierre Isautier, Jerrod Langston, Mohammad Alfiad, Sorin Tibuleac, and Stephen E. Ralph, "ENoB requirements for non-square 64-QAM," IEEE Photonics Conference (IPC), Waikoloa, HI, USA, 2016

30. Justin Lavrencik, **Siddharth Varughese**, Varghese A. Thomas, Gary Landry, Yi Sun, Robert Shubochkin, Kashyapa Balemarthy, Jim Tatum, and Stephen E. Ralph, "2 100Gbps PAM-4 wideband fiber 100m links using 850nm and 940nm VCSELs," IEEE Photonics Conference (IPC), Waikoloa, HI, USA, 2016

31. Justin Lavrencik, **Siddharth Varughese**, Varghese A. Thomas, Gary Landry, Yi Sun, Robert Shubochkin, Kashyapa Balemarthy, Jim Tatum, and Stephen E. Ralph, "100Gbps PAM-4 Transmission over 100m OM4 and Wideband Fiber using 850nm VCSELs," European Conference on Optical Communication (ECOC), Dusseldorf, Germany, 2016

VITA

Siddharth Varughese received his B. Tech degree with honors in electrical engineering from Indian Institute of Technology Madras, Chennai, India, in 2015. Afterwards, he joined the Georgia Institute of Technology, Atlanta, Georgia, USA to pursue his PhD. He is currently with the Terabit Optical Networking Center, a hybrid industry-academic research group at the intersection of fiber optics, high-speed digital communications,digital signal processing and machine learning.

His research interests include linear and nonlinear signal processing for single- and multimode optical links, developing simulation models for optical links, and using machine learning to automate optical network management and accelerate optical component manufacturing. He is a recipient of the Oscar P. Cleaver award 2016 for topping the ECE PhD qualification examination, Oscar P. Cleaver award 2020 for the most outstanding PhD dissertation proposal and ECE Graduate Research Assistant Excellence award 2020 for demonstrating particular excellence in performing his duties.

During his free time, he enjoys playing board games, traveling, and exploring new cultures, and reading about history and politics.